The Biogeochemical Interaction and Alteration of Hydrocarbons in Shallow Sediments of the Scotian Slope, Nova Scotia

By

Anirban Chowdhury

A Thesis Submitted to

Saint Mary's University, Halifax, Nova Scotia

in Partial Fulfillment of the Requirements for

the Degree of Master of Science in Applied Science.

August 2024, Halifax, Nova Scotia

Approved	: Dr. Todd Ventura
	Supervisor
Approved	: Dr. Anne Dalziel
	Internal Committee Member
Approved	: Dr. Shawna White
	Internal Committee Member
Approved	: Dr. Owen Sherwood
	External examiner
	Date: August 2024

Abstract

The Biogeochemical Interaction and Alteration of Hydrocarbons in Shallow Sediments of the Scotian Slope, Nova Scotia

By Anirban Chowdhury

This thesis presents findings from a study on headspace gas and methane clumped isotopic data obtained from various core samples along the Scotian Slope of Nova Scotia. The research aimed to quantify *i*) gas loss during sample storage, *ii*) evaluate the effectiveness of frozen sediment cores in identifying the sulfate methane transition zones, and *iii*) understand the origins and mechanisms of hydrocarbon gases at deep marine, cold seep sites. Results indicated an average of 75% gas loss for Isojars during the first nine months of storage, emphasizing the importance of proper preservation techniques. Optimal conditions for sample analysis were established, aiding in methane core profile construction for identifying shallow sediment, geochemical transition zones. Methane clumped isotopologue analysis revealed a deep biosphere approximately one kilometer below the seabed, sustained by microbial gas production, supporting seep sites near salt diapirs. This study highlights the significance of direct seep gas samples and provides insights into methane dynamics in marine environments and how deep biosphere methane gas production can impact ocean floor community ecology in diapir controlled cold seep localities.

August 2024

Acknowledgments

Completing this master's thesis has been an enriching journey, one that would not have been possible without the support and guidance of numerous individuals and institutions. It is with immense gratitude that I extend my heartfelt appreciation to all those who contributed to this endeavor. First and foremost, I express my deepest gratitude to my supervisor Dr. Todd Ventura, whose unwavering support, invaluable insights, and expert guidance have been instrumental throughout this research. Your mentorship has not only shaped this thesis but has also nurtured my growth as a scholar. I am truly grateful for your patience, encouragement, and dedication. I extend my sincere thanks to the members of my thesis committee, Dr. Anne Dalziel and Dr. Shawna White, for their invaluable feedback, constructive criticism, and scholarly expertise. Your insights have significantly enriched the quality of this work, and I am grateful for the time and effort you dedicated to reviewing and guiding this project.

I am indebted to the Saint Mary's University (FGSR and Dr. Adam Sarty) for providing a conducive environment for research and learning. The resources, facilities, and academic support offered by the university have been indispensable in the completion of this thesis. I am particularly grateful to the staff and faculty of the Geology (particularly Dr. Howard, Dr. Mitch and Dr. Simone) for their assistance and encouragement throughout my academic journey. I would like to express my appreciation to my colleagues and peers for their camaraderie, encouragement, and stimulating discussions. Your friendship and support have made this academic pursuit more enjoyable and rewarding. My heartfelt thanks go to my family Dipanwita, Arjya, Soumyashree and Yogesh for their unwavering love, encouragement, and understanding. Their constant support and belief in my abilities have been a source of strength and motivation throughout this journey. I am deeply grateful for their sacrifices and unwavering faith in my pursuits.

Finally, I dedicate this thesis to Dr. Colleen Barber and Dr. Katherine Robertson, whose inspiration and encouragement have been my guiding light. Your belief in me has been a constant source of motivation, and I am forever grateful for your unwavering support. In conclusion, I am profoundly grateful to all those who have supported and encouraged me on this journey. Your contributions have been invaluable, and I am humbled by your generosity and kindness. This thesis is as much yours as it is mine, and I am honored to share it with you. Thank you.

Anirban

Table of Contents

List of Figures

List of Tables

List of Abbreviations

ppm	Parts per million
‰	Per mille (parts per thousand)
cmbsf	Centimeter below the sea floor
mbsf	Meters below the sea floor
AOM	Anaerobic Oxidation of Methane
µmol/L	Micromole per liter
$\delta^{13}C$	Ratio of the stable isotopes carbon-13 (^{13}C) to carbon-12 (^{12}C)
$\delta^{2}H$	Ratio of the stable isotope deuterium (^{2}H) to hydrogen-1 (^{1}H)
DB	Divergent boundary
CB	Convergent boundary
µL	Microliter
mL	Millilitre
DIC	Dissolved inorganic carbon
BP	British Petroleum
NS	Nova Scotia
ms	Millisecond
M	Molar
KOH	Potassium hydroxide
µm	Micrometer
mm	Millimeter
LN_2	Liquid nitrogen
$mol \cdot L^{-1}$	Mole per liter
$\delta^{13}C\text{-}CH_4$	Stable carbon isotopic composition of methane
$\delta D\text{-}CH_4$	Stable hydrogen isotopic composition of methane
K	Kelvin
°C	Degrees Celsius

Chapter 1. Introduction

1.1. General introduction

In sedimentary basins, complex organic compounds are thermochemically broken-down during late diagenesis and catagenesis, leading to the formation of short-chain, volatile hydrocarbons (Dake and Ershaghi,1996; Selley, 1998). Some of these hydrocarbons, such as petroleum and natural gas, are recovered through drilling and represent commonly used sources of energy for various industries. Crude oil is found buried in the subsurface of the Earth within porous rock formations. Natural gas, on the other hand, is a lighter hydrocarbon gas, often found alongside oil deposits (Ryder and Zagorski, 2003; Allen and Allen, 2013). Natural gas is used for heating, electricity generation, and as a feedstock for various chemical processes. Oil and natural gas are unevenly scattered throughout the Earth's crust and more likely to occur in distinctive geological systems where organic-rich rocks have been buried (Mokhatab et al., 2006; Schoell, 1983; Faramawy et al., 2016). These resources typically form from the remains of ancient organic matter, such as plankton and algae, which accumulated on lake bottoms or the seafloor over millions of years (El Ayouty, 2017). Over time, layers of sediment gradually overlay the organic matter, resulting in progressively higher burial pressures and temperatures. This geological process, referred to as diagenesis and catagenesis, facilitates the transformation of organic matter into hydrocarbons through a series of microbial and thermochemical reactions (Walters, 2017). The type of hydrocarbons formed, and their abundance depend on various factors including the type of organic matter, burial depth, and temperature. Oil and natural gas are typically found in underground reservoirs within sedimentary rocks and take millions of years to form. Porous and permeable reservoir rocks, such as sandstone and limestone, provide spaces for hydrocarbons to accumulate and determines the storage volume (El Ayouty, 2017). However, these reservoirs need

to be sealed with relatively impermeable cap rock for hydrocarbon trapping. Common cap rocks include shale and salt formations. Structure such as anticlines and fault trap, as well as stratigraphic horizons capped by impermeable sealing lithology form petroleum traps also play a crucial role in the process of accumulating hydrocarbons (Dyman, 1997; Bai, and Cao, 2014). Understanding geological characteristics of a potential reservoir is crucial for the petroleum exploration industry. To study such characteristics, various methods such as seismic surveys, well logging, and geochemical analyses are used to identify subsurface structures and to evaluate the potential for hydrocarbon accumulation (Sheriff & Geldart, 1995). Once a promising location is identified, drilling is conducted to access the reservoir and later the hydrocarbons. Understanding the geology of the hydrocarbons is essential not only for resource exploration, but also for predicting reservoir behavior, optimizing production, and minimizing environmental impact.

Oil and gas seeps occurrence provide important clues for early discoveries of petroleum sources (MacDonald et al., 2002; Hélène et al., 2020; Ivanov et al., 2020). Many of the initial giant oil field discoveries were made as the direct result of drilling on or near seepage sites. By studying seeps and the geological reasons for their occurrence (subsurface geochemical study), valuable insight into petroleum systems and fluid flow regimes in an exploration area can be gained that can help reduce exploration risk (Hélène et al., 2020; Ivanov et al., 2020).

Surface geochemistry is used to search for direct or indirect near-surface expressions of hydrocarbon seepage from deeper subsurface hydrocarbon accumulations (Abrams et al., 2001) and is based on the premise that all seals over petroleum reservoirs leak to some extent and hydrocarbons are driven toward the surface by their natural buoyancy. This seepage is detected at or near the surface as elevated hydrocarbon concentrations, changes in sediment mineralogy, and/or a biological response to the presence of the hydrocarbons (Dembicki Jr and Samuels, 2007;

Pape et al., 2011; Batang et al., 2012). The hydrocarbon seepage sought after in surface geochemistry is usually divided into microseepage and macroseepage (Judd and Hovland, 2009). Microseepage is low-concentration seepage where only small amounts of hydrocarbons are leaking by vertical migration to the surface (Calhoun and Hawkins, 2002). Microseepage is not obvious to an observer at the surface and is normally detected via geochemical analysis of near-surface sediments. In contrast, macroseepage is high-concentration seepage where large amounts of hydrocarbons are leaking, resulting in visible or easily detectable oil and gas at the surface (Hovland et al., 2012). This type of seepage is usually closely associated with faults or fracture zones that extend down to the vicinity of the reservoir (Fig. 1.1).

The seepage of these fluids occurs globally on submerged continental margins and consists of CO_2, gaseous and liquid hydrocarbons, and brines (Judd and Hovland, 2007). These fluids originate from different depths within the sedimentary column and can undergo geochemical and microbial reactions (e.g., solid precipitations) during their migration (Klusman, 2004). Their expulsion at the seafloor can lead to the formation of diverse seafloor morphologies, including mud volcanoes (Milkov et al., 2004), pockmarks (Marcon et al., 2014), carbonate build-ups (Greinert et al., 2001), and brine lakes (Dupré et al., 2014) (Fig. 1.1). The water column also hosts chemical components that interact with those present in the ascending fluids. Methane or organic matter, when combined with sulfates, releases hydrogen sulfide. In marine sediment, sulfate reduction is linked with organic matter oxidation (Meister et al., 2013) or anaerobic oxidation of methane (Boetius et al., 2000; Gao et al., 2022; Mao et al., 2022), or both. Regardless of the coupled-oxidation process, the overall redox reaction releases bicarbonate ions, which promotes carbonate precipitation (Fig. 1.1).

Accurately identifying gas sources and their formation mechanisms presents significant challenges (Lu et al. 2008) due to three main issues: i) minimizing gas loss during sampling and storage, ii) preventing degradation of samples caused by microbial activity, and iii) obtaining minimally fractionated samples (Torres, 2002). To address these challenges and improve the understanding of subsurface geochemistry (Kvenvolden & Lorenson, 2000), there is a need for more effective methodologies that integrate laboratory experiments, theoretical models (Donval et al. 2008), and statistical analysis. This study compares the characteristics of hydrocarbons in headspace gases from core samples at different depths along hydrocarbon potential areas of the Scotia Slope, using analyses of gas composition and carbon isotopes of methane. The study also examines the least attenuated samples from active seep sites on the Scotia Slope and the formation mechanism of seep gas linking its relationship with salt tectonics of the area.

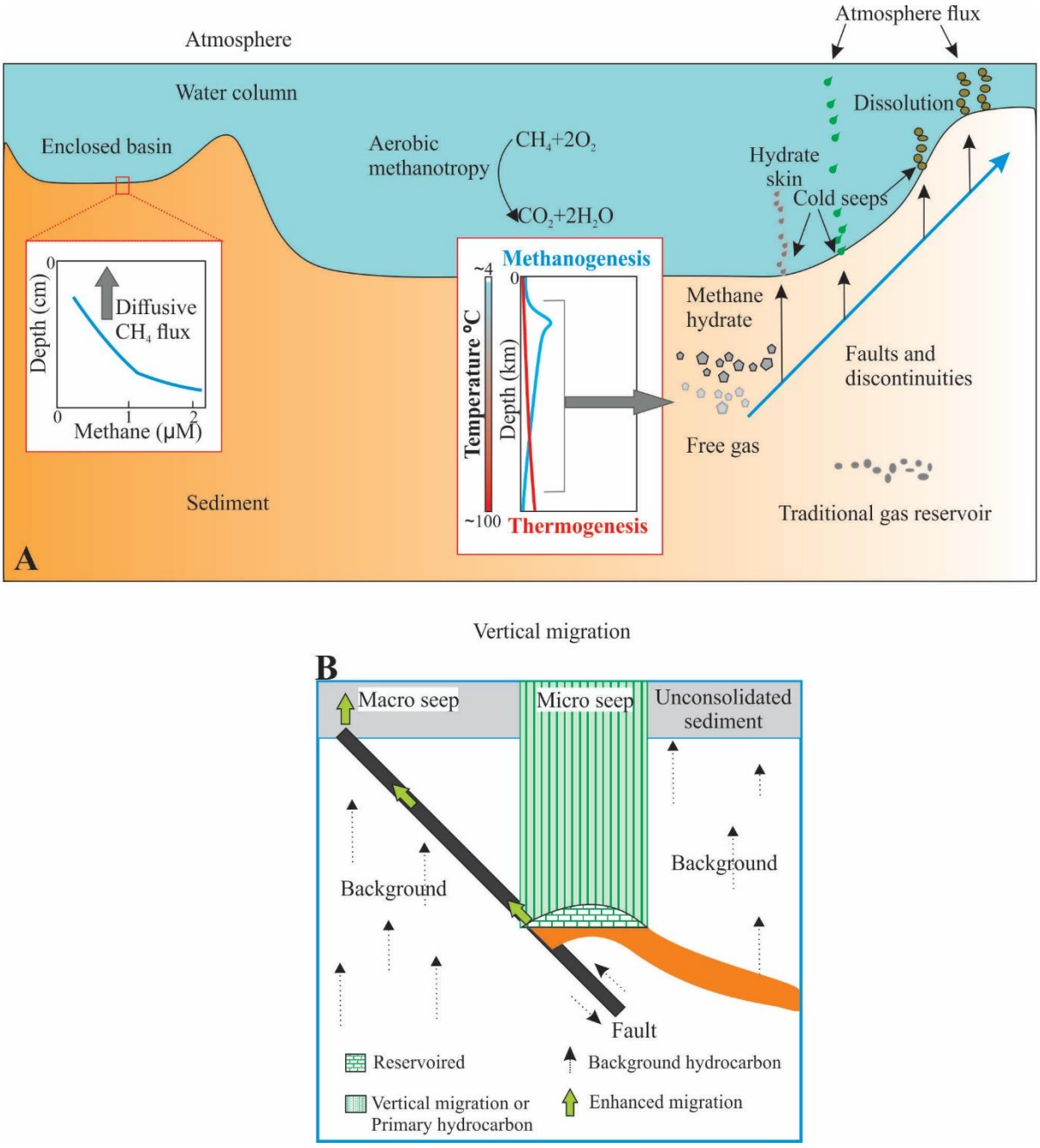

Figure 1.1. A) General offshore subsurface profile indicating important features, geobiological mechanism, and occurrences of seep sites (modified after Valentine, 2011). B) Geological conditions responsible for occurrences of micro- and macro-seeps (modified after Potter et al. 1996; Rasheed et al., 2015).

1.2. Natural gas composition and classification

1.2.1. Natural gas

Natural gas of geogenic origin (thermogenic gas) is a gaseous fossil fuel and when occurring in petroliferous geological formations, represents a volatile mixture of low molecular weight hydrocarbon and non-hydrocarbon compounds (Fig. 1.2). Natural gas normally includes nitrogen (N_2) and carbon dioxide (CO_2), and small quantities of hydrogen sulfide (H_2S) and trace quantities of noble gases like argon, hydrogen, and helium (Fig. 1.3) may also be present (Mokhatab et al., 2006, Speight, 2018, Mokhatab et al., 2018). Rarely, the presence of low molecular weight aromatic hydrocarbons such as benzene, toluene, and xylenes (Mokhatab et al., 2006) have also been detected. Though natural gas hydrocarbons are odourless and colorless, the presence of sulfur compounds like mercaptans and hydrogen sulfide imparts an associated odor. Generally, hydrocarbons constitute more than 90–95% of natural gases and is composed of methane, followed by ethane, propane, butanes (table 1.1), and heavier gas volatile hydrocarbons (Khilyuk et al., 2000). The proportions of a particular hydrocarbon gas (C_1–C_6) are inversely proportional to their molecular weight, with methane making up the maximum compositional abundance. The relative ratio of the proportion of hydrocarbons (C_1–C_6) vary for gases of different origins, so may act as a molecular tracker to identify the origin of the natural gas (Mokhatab et al., 2006; Speight, 2018).

Table 1.1. Natural gas (thermogenic) composition and molecular abundance (Speight, 2015).

Chemical constituents in natural gas	Molecules	Range (%)
Methane	CH_4 (C_1)	85–100
Ethane	C_2H_6 (C_5)	3–8
Propane	C_3H_8 (C_3)	1–5
Butane	C_4H_{10} (C_4)	1–2
Pentane	C_5H_{12} (C_5)	1–5
Hexane	C_6H_{14} (C_6)	2
Carbon dioxide	CO_2	1–2
Hydrogen sulfide	H_2S	1–2
Oxygen	O_2	0.1
Nitrogen	N_2	1–5
Helium	He_2	0.5

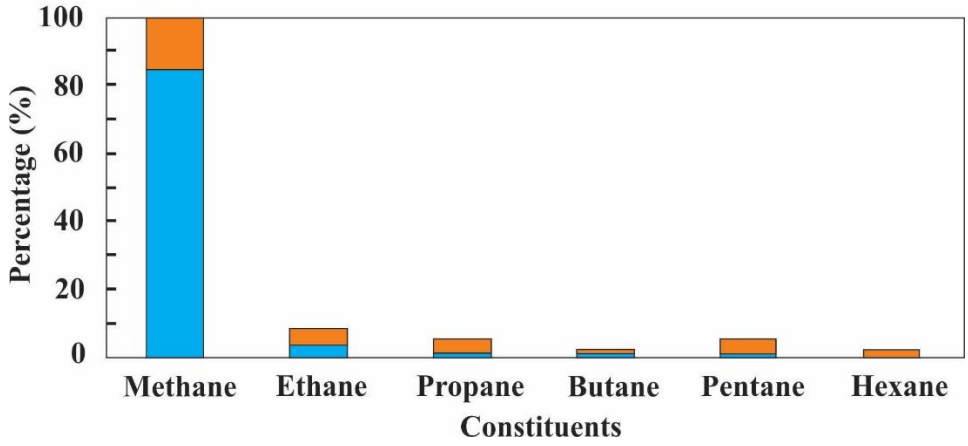

Figure 1.2. The compositional abundance of hydrocarbon gases in natural gas. C_1 typically constitute more than 80%. The orange bar shows the maximum abundance (modified after Speight, 2015).

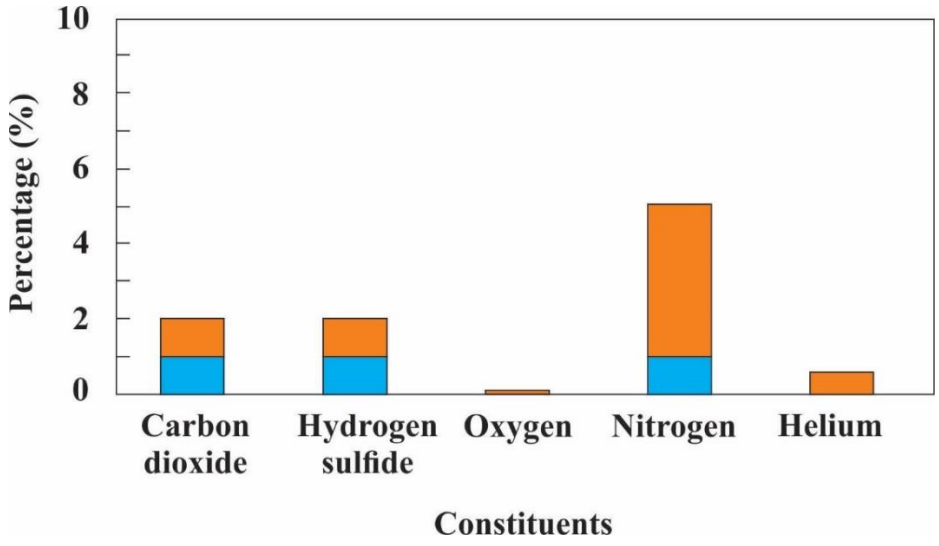

Figure 1.3. The compositional abundance of nonhydrocarbon gases in natural gas (modified after Speight, 2015).

1.2.2. Classification of natural gas

Natural gas can be classified by origin or by chemical composition, which evaluates the quality of the gas and its energy content (Schoell, 1983, Rojey et al., 1997; Kidnay et al., 2011; Speight, 2007; Tagliabue et al., 2009). The thermogenic natural gas (usually associate with petroleum) can be categorised as a conventional or unconventional gas (Fig. 1.4). Conventional gasses are found in deep reservoirs and are either associated with crude oil (associated gas), or not associated with crude oil (non-associated gas). These gases occur in free, condensate or dissolved states and are formed in conventional reservoirs having typical petrophysical property. Geologically petroleum reservoir has a well-defined tight cap rock and formation pressure coefficient. Unconventional gases are irreconcilable with conventional mechanisms, features and have a debatable accumulation mechanism like shale gas, coal bed methane, and gas hydrates (Zhi-jun et al., 2003; Jin et al., 2022). Natural gas can also be categorized based on the abundance of hydrocarbon composition (vol. %) as wet gas having C_{2+} greater than 10% and dry gas having C_{2+} less than 10%. Trace amount of hydrogen sulfide (H_2S) is also found in natural gas and easily detected by

its smell. The gas with hydrogen sulfide concentration greater 4 ppm is termed as sour gas and below 4 ppm to zero is termed as sweet gas (Aminzadeh and Dasgupta, 2013; Ali, 2017).

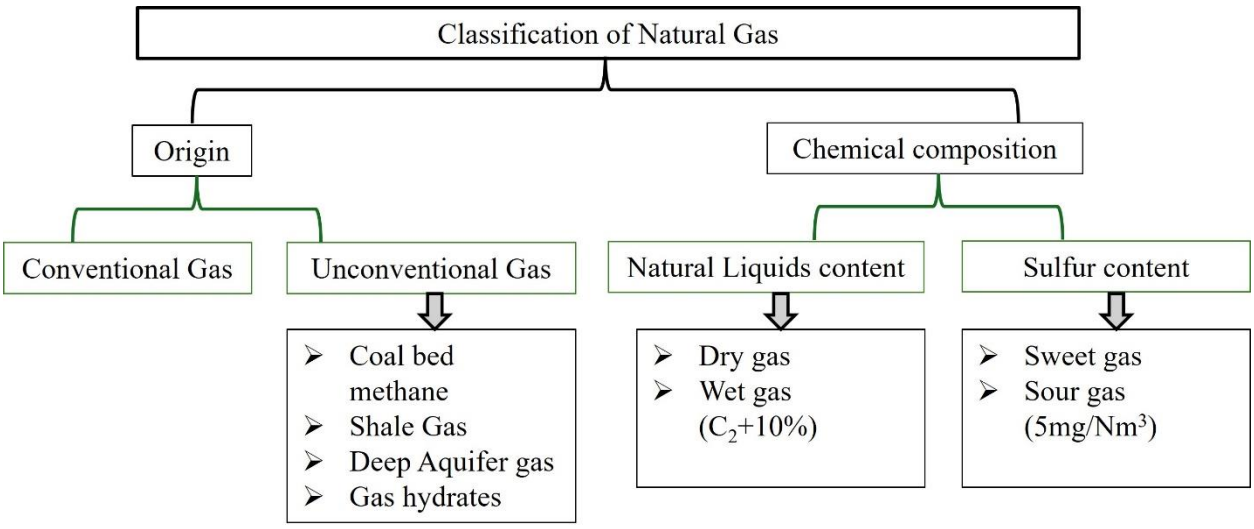

Figure 1.4. Showing the traditional classification of natural gas based on origin and chemical composition (modified after Speight, 2007).

1.2.3. Formation of petroleum and natural gas (thermogenic gas)

The process of petroleum formation initiates with the accumulation of organic materials in sedimentary basin. Increases in the overlying sediment burial depth are accompanied with elevated burial temperature (Aminzadeh and Dasgupta, 2013; Ali, 2017). At depths beyond 2 km, and at temperatures ranging from 60 to 120 °C, the organic matter is converted to oil and natural gas due to dehydration and then thermal cracking of organic molecules. This depth and temperature range is known as the "oil window" (Fig. 1.5). Beyond 120 °C most of the organic matter is thermochemically converted to gas (Faramawy et al., 2016; McCabe, 2012; Burrows et al., 2020). Thermogenic gas formed during catagenesis can reach burial temperatures of 250 °C. Microbial

(biogenic) gas primarily formed during diagenesis arises at much lower temperatures of 60–80°C (Hunt, 1996).

Most natural petroleum systems include source rocks, reservoir rocks, trapping mechanisms, migration routes, and sealing elements (see Fig. 1.5). The organic-rich rock layer leading to the formation of gas and oil is called the source rock (Racey, 2011; Ali, 2017). Liquid and gaseous hydrocarbons tend to slowly move from the source rock toward the surface. Reservoir rocks are relatively permeable and allow for migration of the fluids from the source rocks to facilitate recovery of the oil or gas. In some cases, the liquids and gases make it all the way to the surface, while in other cases, they are contained by overlying impermeable rocks (e.g., mudrock) (Magoon and Dow, 1991; Gluyas and Swarbrick, 2021). Migration pathways facilitate the movement of matured hydrocarbons from regions of higher potential (pressure) to those of lower potential, (pressure) typically progressing from greater depths to shallower depths. Various types of petroleum traps exit, including anticlinal, fault-related, and salt-related stratigraphic traps, that serve as collection points for deeper basin migrating hydrocarbons (Selley, 1998). For example, sealing rocks, possessing low permeability, encase hydrocarbon traps, thereby limiting the escape of entrapped fluids. One of the signature structural features of oil and natural gas reservoir is an antiform shape (Fig. 1.5) and considered crucial for hydrocarbon exploration. These features often trap oil and gas within their porous and permeable layers, making them significant targets for drilling operations. The migrated liquids and gases trapped within reservoirs segregate into layers based on their density, with gas rising to the top, oil below it, and water underneath the oil. The proportions of oil and gas depends primarily on the source rock temperature.

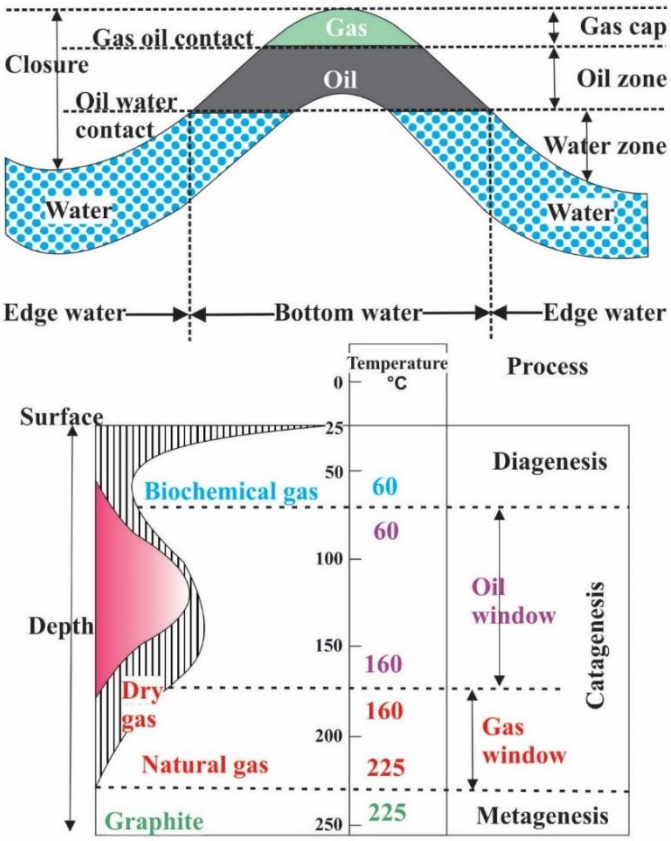

Figure 1.5. Top) typical natural gas and petroleum occurrence in a basin, highlighting the antiform shape (gas, oil and oil contact) of the reservoir and their relative positions. Bottom) gas oil window and formation temperature of biogenic and thermogenic gas (modified after Duggan-Haas et al., 2013).

1.3. Sources of methane

The two dominant processes in passive plate margin settings that generate methane in natural systems are biogenic and thermogenic processes (Wuebbles and Hayhoe, 2002). Biogenic methane gas (≥ 99 % methane) is produced as a direct consequence of microbial activity and is usually generated a few tens of meters below the seabed. Biogenic methane gases have a low formation temperature and constitute over 20% of the world gas reserve (Rice and Claypool, 1981). During the early subsidence of sediment, oxygen is consumed by aerobic respiration, which is followed by a shift to anaerobic modes of metabolism such as microbial sulfate reduction that leads to carbon

remineralization (Rice and Claypool, 1981; Milkov, 2011; Amiel et al., 2020). The rise in methane production happens primarily through reduction of CO_2 by hydrogen generated from the anaerobic oxidation of organic matter. In the subsurface (> 1 Km) the production rate of biogenic methane is controlled by temperature (less than 60 ℃), higher concentration of organic matter, anoxic condition, and lack of sulfate or other terminal electron acceptors and donors (Thiagarajan et al., 2020). Microbial methanogenesis is the main terminal process of subsurface anaerobic organic-matter biodegradation (Pace, 2009).

In contrast, thermogenic methane usually occurs at sub-bottom depths exceeding 1,000 m. These hydrocarbon gases are produced under conditions of high temperature (Douglas et al., 2017; Thiagarajan, 2020) and great pressure from kerogens (which are derived from organic matter) usually derived from an organic-rich source rock (Faramawy et al., 2016). A minor fragment of global methane is also generated by abiotic process having a non-organic source of origin. This methane is economically non-exploitable due to its rarity in occurrences and abundance (Dai et al., 2005; Jin et al., 2009). Abiotic methane is usually formed from high temperature chemical reaction occurs in restricted geologic environments (Dutkiewicz et al., 2004; Etiope and Sherwood Lollar, 2013).

1.3.1. Distinguishing biogenic and thermogenic methane gas

Conventionally, the origin of hydrocarbon gases is inferred through the molecular composition of gases (e.g. the ratio of methane (C_1) to higher-order hydrocarbons (C_{2+}) or C_1/C_{2+} (Schoell, 1983), carbon dioxide (CO_2), and nitrogen (N_2)), and by the (2) stable isotopic composition of gases (e.g. δ^2H-CH_4, δ^{13}C-CH_4, δ^{13}C-CO_2) (Fig. 1.6, Fig. 1.7) (Whiticar, 1994; Kohnert et al., 2017; Wesley et al., 2023). By combining measurements of hydrocarbon molecular composition (Bernard et al., 1977; Schoell, 1980) with measurements of stable carbon and hydrogen isotopes in methane

(Whiticar, 1994; Kohnert et al., 2017; Wesley et al., 2023), the gas's source mechanism can be studied. For example, biogenic gas (δ^{13}C-CH_4 <−55 per mil, denoted as ‰ with C_1/C_{2+}> 200) can be distinguished from thermogenic gas (δ^{13}C-CH_4 > −55 ‰ with C_1/C_{2+} < c. 100) on a plot of δ^{13}C-CH_4 v. C_1/C_{2+} (Bernard et al., 1976).

These classifications are based on the biogenic and thermogenic gas generic diagram, and they are revised every few years with advancement in technology (Fig. 1.6, Fig. 1.7; Bernard et al., 1976; Milkov and Etiope, 2018). These isotopic and molecular composition classification tools are limited when the collected gas samples are fractionated or have mixed gases. However, more recently the estimation of molecular formation temperature of methane using clumped isotopologue techniques have come online that further enable classification of hydrocarbon gas origin (Stolper et al., 2014a; Young et al., 2017). Since the clumped isotopologue measures the state of ordering and abundance of one or more rare isotope ($^{13}CH_3D$, $^{12}CH_2D_2$) can overcome the limitation imposed by traditional isotopic methods (Stolper et al., 2014a; Stolper et al., 2014c; Stolper et al., 2015).

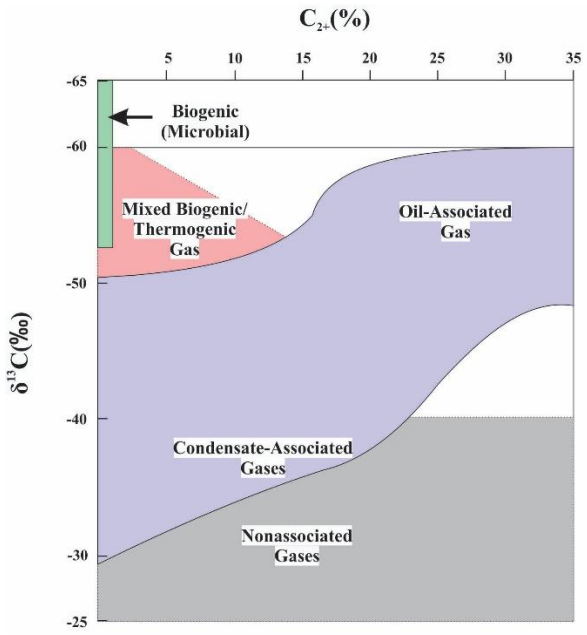

Figure 1.6. Differentiation of biogenic (microbial), thermogenic and mixed gas based on the dryness of the gas (C_{2+} (%)) and the carbon isotopic composition of methane (modified after Schoell, 1983).

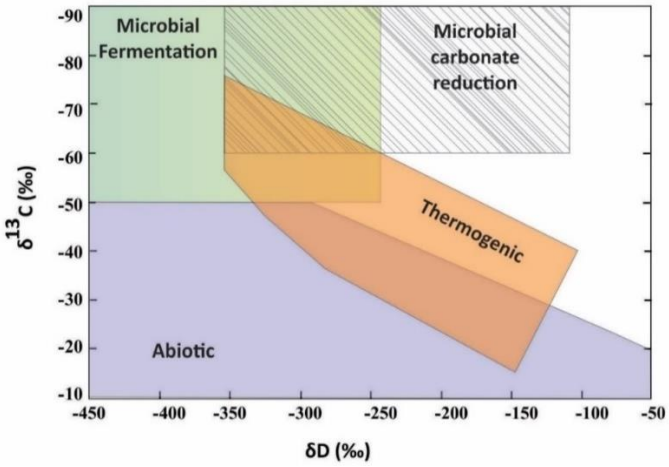

Figure 1.7. Generic classification diagram based on hydrogen isotopes (δD) vs carbon isotopes ($\delta^{13}C$) used in petroleum industry to classify gas origin and formation of natural gas. Modified after Dong et al. (2021), Douglas et al. (2017), Etiope (2015), Etiope and Sherwood Lollar (2013), Milkov and Etiope (2018), Schoell (1980), Sherwood et al. (2017).

1.4. Seep sites and their geological occurrences

Continental passive margins are known to host approximately 35% of the worlds oil and gas fields (Fig. 1.8). In recent years, notable strides in deepwater geological theories and exploration technologies have yielded a substantial surge in the discovery of oil and gas fields within these deepwater continental margin basins (Song et al., 2020). Hydrocarbon enrichment in these settings is facilitated by the availability of quality source rock, the presence of adequate reservoir rock, the development of a seal and trap that can contain migrating hydrocarbons. All of the elements of a petroleum system must be in place in their correct order of evolution for any significant hydrocarbon discovery to be found. Where seals leak, ocean cold seeps can be formed. Seafloor seepage of upward migrated fluids is a widespread phenomenon in these continental margins facilitated by the underlying hydrocarbon storage and production. The emission of light hydrocarbons as methane to the water column and possibly to the atmosphere make them an important target for scientific studies as do their effects on seafloor stability and deep-sea biology (Andresen and Huuse, 2011; Andresen et al., 2011; Løseth et al., 2011; Ho et al., 2012; Serié et al., 2012). Notable examples include the Guyana Basin and the Lower Congo Basin (Pettingill, 2001; Pettingill, 2001; Pang, 2004; Weimer et al., 2006; Weimer and Pettingill, 2007). The Scotian Basin, situated on the western fringe of the Mid-Atlantic Ocean, stands as a prototypical example of a passive continental margin basin (Karim et al., 2012; Campbell et al., 2015).

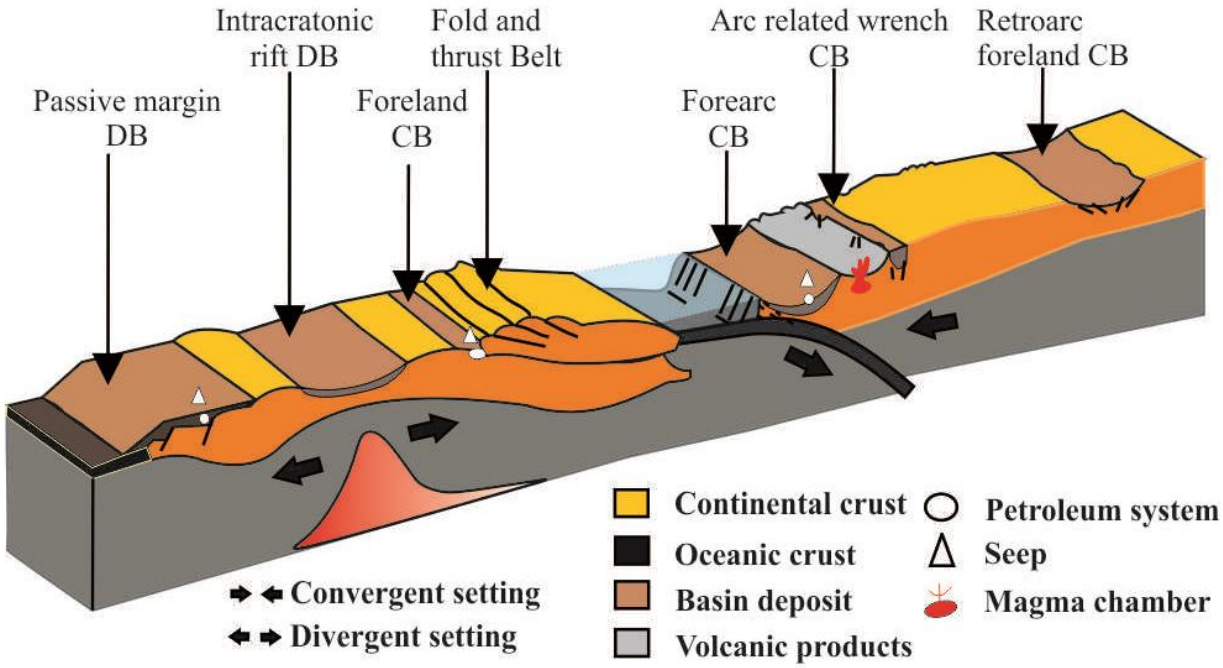

Figure 1.8. Top- Geological setting and major occurrence of seep sites. The colorless triangle and ellipse represent the seep site and petroleum system (modified after Ciotoli et al., 2020).

1.5. Cold seeps

The deep sea includes a wide array of environments, such as abyssal plains, mid-ocean ridges, and submarine canyons, each with distinct geological features and processes. Cold seeps are unique marine environments where hydrocarbons and other low temperature fluids seep out of the ocean floor. These environments often supporting diverse ecosystems. In contrast, other types of seeps, like hot springs or mud volcanoes, release fluids at different temperatures and with distinct chemical compositions, shaping various ecosystems (Batang et al., 2012). Globally, deep-sea cold seeps are more likely to form at convergent boundaries associated with salt tectonics (Fig. 1.9) (Spiess et al., 2008). These seeps represent a complex interplay of geological processes, fluid dynamics, and biological interactions. Cold seeps occur where methane and other hydrocarbons, often sourced from subsurface petroleum reservoirs, migrate upwards through sediment layers,

eventually reaching the seafloor (Gay et al., 2007; Wenau et al., 2015). Sediment diapirs, caused by the upward migration of gas and fluids, deform the seafloor and create localized topographic highs. Oval and conical pockmarks, and microbial mats are few distinct sea floor features caused by the upward migration of fluids in seeps (Andresen et al., 2011; Boswell et al., 2012). Cold seeps are known for their enrichment in gas hydrate deposit and distinct features like authigenic carbonate chimneys, and sediment diapirs. Authigenic carbonate chimneys, composed of minerals precipitated from hydrothermal fluids, can reach significant heights, and serve as habitats for chemosynthetic communities (Suess, 2014; Wenau et al., 2015).

1.6. Salt diapirs and cold seeps

Salt diapir accompanied by faulting and gas-charged conditions, is frequently associated with the migration and accumulation of hydrocarbons (Schroot and Schüttenhelm, 2003). Salt diapirs are characterize by low density, unique plasticity and high thermal conductivity. Their contrasting geological properties from their surroundings creates mechanical instability creating faults and domes in the associated areas (Jackson and Hudec, 2017). Due to higher thermal conductivity of salt, salt tectonics induces: *i*) a rise in local geotherm, *ii*) the development of radial faults (Zhuo et al., 2016) and *iii*) the formation of direct hydrocarbon indicators (an antiform shaped trap) facilitating the occurrences of macro and micro seeps (Fig. 1.9. The commonly associated salt tectonics, observed in regions such as the Scotian Basin, Gulf of Mexico and the Mediterranean Sea, result in complex structural features such as salt domes and diapirs, influencing sedimentary processes and hydrocarbon accumulation that feeds these seeps (Luheshi et al., 2012).

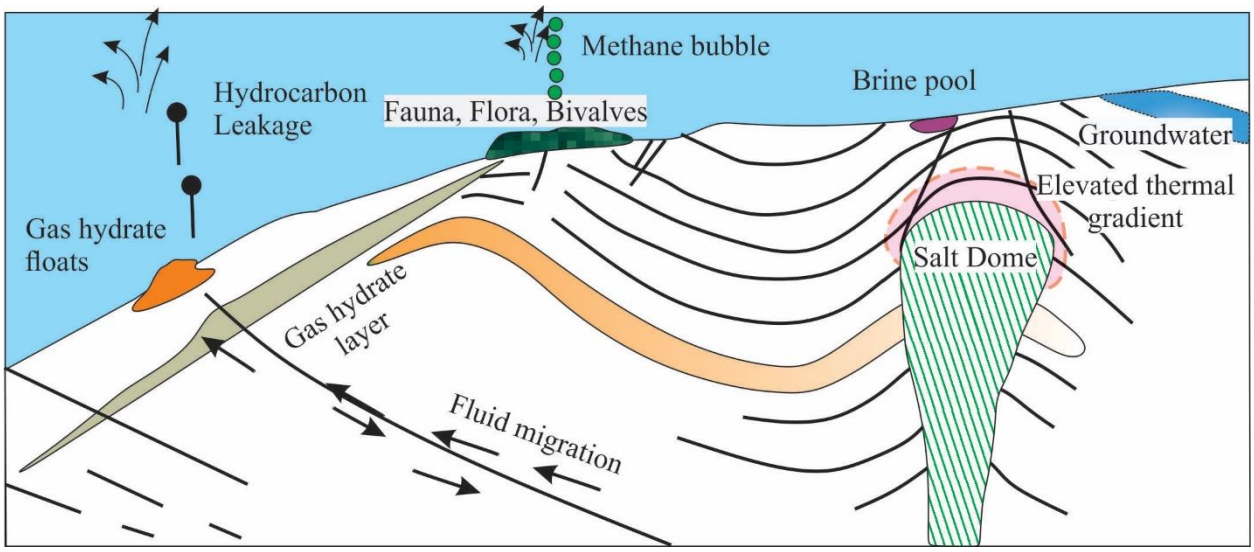

Figure 1.9. Passive margin geologic settings and forces of fluid expulsion generate different types of cold seeps; pockmarks on shelves and slopes caused by outflow from submerged aquifers, over pressured formations containing hydrocarbons and brines, and rapidly accumulating water-rich sediments in deltas or drift deposits. Carbonate chimneys, asphalt seeps, methane hydrate mounds, seep fauna, and methane plumes in the water column are ubiquitous manifestations as are infrequently observed methane hydrate rafts (modified from Suess, 2014).

1.7. Methane isotope geochemistry

Methane isotope geochemistry serves a wide array of applications beyond its role as a tool for distinguishing between biogenic and thermogenic methane sources (Fig. 1.6). The carbon and hydrogen stable isotope signatures of methane can reveal information about the origin of natural gas and enable us to differentiate between pathways of microbial methanogenesis (Whiticar et al., 1986). The two isotope systems are reported as $\delta^{13}C$ and δD (Fig. 1.7) values representing the normalized products defined as $(R_s/R_{std} - 1) \times 1000$; where $R = [D]/[H]$ and $[^{13}C]/[^{12}C]$ where "s" represents the sample and "std" indicates the analytical standards VSMOW (Vienna Standard Mean Ocean Water) and VPDB (Vienna Pee Dee Belemnite), respectively (e.g., Whiticar et al., 1986; Whiticar, 1999). Together the carbon and hydrogen stable isotope compositions are used to determine how methane formed, commonly by constructing Whiticar (Whiticar, 1999) and

Bernard plots, with the later also utilizing the variability of higher hydrocarbon number gases via a ratio of $C_1/ (C_2 + C_3)$ (Bernard et al., 1976). The methane isotope compositions fall into unique fields that distinguish their different formation conditions (Fig. 1.7), including the specific mechanisms by which isotopic fractionation occurs within an environment and the biogeochemical reactions resulting in methane formation (Douglas et al., 2017; Etiope, 2015; Etiope and Sherwood Lollar, 2013; Milkov and Etiope, 2018). The isotopic signatures of methane can still widely vary within a particular source-origin field of the $\delta^{13}C$ and δD plot that do not have distinct sharp boundaries on a Whiticar and Bernard plot (Fig. 1.6, Fig. 1.7). This is because the alteration of a natural gas mixture can result in kinetic isotope effects (KIEs) that attenuate the natural isotopic composition of methane at the initial substrate level of formation and/or by later reaction rates associated with the movement and interaction of the gas in a natural system (Whiticar, 1999). Additionally, the amassing of methane within a reservoir or its escape at a seep (Joye, 2020) is often the result of a gas being oxidized by aerobic and anaerobic processes, and mixed from multiple sources (Etiope and Sherwood Lollar, 2013). Traditional stable isotopic analyses can therefore fail to determine the provenance and formation conditions of methane (Stolper et al., 2014a; Young et al., 2017). The conventional carbon isotope compares the most abundant stable isotope ratios are also not capable of revealing the fraction of thermogenic methane present in natural methane reservoirs (Zhang et al., 2021) or providing information about the formation temperature, particularly for thermogenic methane, which is mostly ambiguous in natural environment.

The measurement of clumped isotopologues of methane $^{13}CH_4$, $^{12}CH_3D$, $^{13}CH_3D$, $^{12}CH_2D_2$ (e.g. Stolper et al., 2014a; Ono et al., 2014) can be used to identify the formation temperature of methane. Moreover, the ratio of clumped isotopic species appears to better reflect environmental

condition from mixed samples compared to measurements of $\delta^{13}C$ and δD. In cases where methane has been formed and trapped in thermodynamic equilibrium condition, clumped isotopes are able to provide the absolute direct measurement of the gas's formation temperature (Stolper et al., 2014a; Stolper et al., 2014c; Stolper et al., 2015; Xie et al., 2021). The ability of methane clumped isotopologues to also act as a tracer, revealing information about gas origin and the source of its carbon substrate, makes a powerful isotopic tool. Recent advances in the measurement of multiple substituted isotopologues of methane ($^{13}CH_3D$ and $^{12}CH_2D_2$) have opened the opportunity to study the formational condition of the gas (Ono et al., 2014; Stolper et al., 2014a). It is experimentally observed that the deviation of methane clumped isotopologue composition from the theoretically determined random distribution of isotopes in bulk is a function of temperature. This comparative measurement between the theoretical prediction and observed deviation can be used to construct a methane isotopologue geothermometer (Ono et al., 2014; Stolper et al., 2014a; Webb & Miller 2014; Liu and Liu 2016; Young et al., 2016; Young et al., 2017; Eiler et al., 2013; Zhang et al., 2021). High-resolution gas-source isotope-ratio mass spectrometers or laser absorption spectrometers are widely used to determine the relative abundances of unsubstituted ($^{12}CH_4$), singly substituted ($^{12}CH_3D$, $^{13}CH_4$) and multiply substituted isotopologues ($^{13}CH_3D$, $^{12}CH_2D_2$) of methane (Young et al., 2016; Young et al., 2017; Eiler et al., 2013).

While stable carbon isotopic data provides invaluable information about the seep gas and helps to identify its origin, sources, and formation mechanism, radiocarbon data (^{14}C) offers unique information about the age of the gases. Radiocarbon dating helps to resolve the ambiguity for the overlapping field boundaries within stable isotopic data (Kessler et al., 2005; Sparrow et al., 2018) and can distinguish methane sources from fossil and modern-day microbial origin. Fossil methane lacks detectable ^{14}C and can be older than 57,300 years, equivalent to ten half-lives of ^{14}C

(radiocarbon dead), and manifests as 0% modern carbon (pMC). Moreover, $\delta^{14}C$ can aid in distinguishing direct seeps gas and gas hydrates by comparing relative contributions of migrated vs. locally generated methane (Pohlman et al., 2009). However, $\delta^{14}C$ applications are limited as they need pure samples and the ^{14}C values are largely influenced by local (geological, microbiological, and atmospheric) and anthropogenic factors (Clark et al., 2000; Heeschen et al., 2005).

1.8. Scotian Margin petroleum systems

The offshore of Nova Scotia is well known for its hydrocarbon potential and unique geological setting (Enachescu and Hogg., 2005; OERA; Pe-Piper et al., 2008; Smith et al., 2014). The hydrocarbon potential of the Scotian Basin has been evaluated by many workers (Mukhopadhyay, 2003; Enachescu and Hogg., 2005; Pe-Piper et al., 2008; Sachse et al., 2012; Smith et al., 2014) and different hydrocarbon potential sites have been discovered and developed as significant sources of gas and oil in the last decade. Pre-exploration investigation and record bids of over one billion dollars were made by Shell Canada Ltd. in 2011 and BP Exploration Operating Ltd. in 2012 for four blocks (Oil, 2018). Independent government and private organizations like Department of Natural Resources and Renewables (DNRR-2010), Geological Survey of Canada (Campbell & MacDonald, 2016), the Canada-Nova Scotia Offshore Petroleum Board (CNSOPB), and universities of the Maritimes have conducted routine surveys in the Scotian Basin to evaluate hydrocarbon potential. One recent product of this work is the Play Fairway Analysis (Play Fair Analysis, 2011; MoH et al., 2011), which proposed the existence of an underlying lower Jurassic source rock based on data from the neighboring basin and indirect observation of oil and condensates (Et-Touhami et al., 2012; Sachse et al., 2012; Oliveira et al., 2006; Duarte et al., 2010; Silva et al., 2011). LeBlanc et al. (2007) used 2D velocity models with two-way simultaneous

travel-time inversion to predict the occurrence of gas hydrate of up to 2-6% and free gas concentrations less than 1–2%, in the sediment pore space up to an average depth of 200 meters below the sea floor (mbsf). These and other reports indicate that identifying prospective source rocks in the basin is challenging, with a mix of known and suspected intervals (Mukhopadhyay, 2003, 1995; NSDoEM, 2011; BEICIP-FRANLAB, 2011). The Scotia Basin consist of a complex play of salt tectonics due to the movement of the underlying salt diapir (Decalf and Heyn, 2022). Salt is ductile, and the rising salt diapir triggers basins and variable topography along the seabed. These *in situ* salt tectonics generate a network of faults and enable hydrocarbon flow through the system. As the fluids migrate through the faults and interact with the salt bodies, their fluid chemistry is altered generating distinct geochemical signatures and creating micro and macro seepage (Joye, 2020; Brun and Fort, 2018; Kramer and Shedd, 2017).

The Scotian Slope lies in the offshore region of Scotian Basin and is characterised by hydrocarbon seepage. Seismic images of the Scotian Slope reveal the existence of underlain salt diapirs and dome shaped structures ideal for hydrocarbon accumulation. Furthermore, the Scotian Slope is a part of passive continental margin increases the possibility of being potential hydrocarbon-rich zone (Play Fair Analysis, 2011; MoH et al., 2011). Detecting and sampling seeps and its surrounding sediments (drilling and coring) on the seabed can strongly indicate the presence of an explorable petroleum system and provides crucial insights into the hydrocarbon source, migration pathways, and maturity. However, sampling hydrocarbon seeps is challenging due to high cost, technological constrain (special vessels), their transient nature and the complexities of the environment (Campbell, 2019). This study aims to assess the hydrocarbon potential of the region by analyzing samples obtained during cruises conducted between 2015 and 2021 as part of the

Genome Application Partnership Program (Campbell, 2019; Ventura et al., 2023; Owino, 2023) to assess the hydrocarbon potential of the area and formation mechanism of the seep gases.

1.9. Structure of thesis

This thesis is divided into four chapters and presents findings from two distinct research projects. Each chapter begins with an introduction outlining the research hypothesis and objectives. Chapter 1 serves as an introduction, providing contextual information on subsurface geochemistry, gas geochemistry, isotopic analysis of hydrocarbon gases, the study area, sample classifications, and delineating the thesis primary objectives. In Chapter 2, includes an experimental investigation aimed at optimizing gas storage methodologies and contrasting the gas retention capabilities of confined versus unconfined sediment samples. Chapter 3, published as a research article, presents the results of a methane clumped isotopologue study conducted on three different types of gas samples collected from active seep sites along the Scotian slope. As Chapters 2 and 3 are prepared as separate manuscripts for journal submission, there is some redundancy, particularly in the introductions and methodologies. Finally, Chapter 4 summarizes the key findings of both studies and outlines future research direction.

References

Abrams, M. A., Segall, M. P., & Burtell, S. G. (2001, April). Best practices for detecting, identifying and characterizing near-surface migration of hydrocarbons within marine sediments. In Offshore Technology Conference (pp. OTC-13039). OTC.

Ali, H. N. (2017). Fundamentals of petroleum geology. Springer Handbook of Petroleum Technology, 321-357.

Allen, P. A., & Allen, J. R. (2013). Basin analysis: Principles and application to petroleum play assessment. John Wiley & Sons.

Amiel, N., Shaar, R., & Sivan, O. (2020). The effect of early diagenesis in methanic sediments on sedimentary magnetic properties: Case study from the SE Mediterranean continental shelf. Frontiers in Earth Science, 8, 283.

Aminzadeh, F., & Dasgupta, S. N. (2013). Fundamentals of petroleum geology. In Developments in Petroleum Science (Vol. 60, pp. 15-36). Elsevier.

Andresen, K. J., & Huuse, M. (2011). 'Bulls-eye' pockmarks and polygonal faulting in the Lower Congo Basin: relative timing and implications for fluid expulsion during shallow burial. Marine Geology, 279(1-4), 111-127.

Andresen, K. J., Huuse, M., Schødt, N. H., Clausen, L. F., & Seidler, L. (2011). Hydrocarbon plumbing systems of salt minibasins offshore Angola revealed by three-dimensional seismic analysis. AAPG bulletin, 95(6), 1039-1065.

Andresen, K. J., Huuse, M., Schødt, N. H., Clausen, L. F., & Seidler, L. (2011). Hydrocarbon plumbing systems of salt minibasins offshore Angola revealed by three-dimensional seismic analysis. AAPG bulletin, 95(6), 1039-1065.

Bai, G. P., & Cao, B. F. (2014). Characteristics and distribution patterns of deep petroleum accumulations in the world. Oil Gas Geol, 35(1), pp. 19-25.

Batang, Z. B., Papathanassiou, E., Al-Suwailem, A., Smith, C., Salomidi, M., Petihakis, G., ... & Fayad, N. (2012). First discovery of a cold seep on the continental margin of the central Red Sea. Journal of Marine Systems, 94, 247-253.

BEICIP-FRANLAB (2011) Play Fairway Analysis (PFA) offshore Nova Scotia Canada. Published report. http://www.novascotiaoffshore.com/analysis.

Bernard, B. B., Brooks, J. M., & Sackett, W. M. (1976). Natural gas seepage in the Gulf of Mexico. Earth and Planetary Science Letters, 31(1), 48-54.

Boetius, A., Ravenschlag, K., Schubert, C.J., Rickert, D., Widdel, F., Gieseke, A., Amann, R., Jørgensen, B.B., Witte, U. and Pfannkuche, O. (2000). A marine microbial consortium apparently mediating anaerobic oxidation of methane. Nature, 407(6804), 623-626.

Boswell, R., Collett, T. S., Frye, M., Shedd, W., McConnell, D. R., & Shelander, D. (2012). Subsurface gas hydrates in the northern Gulf of Mexico. Marine and Petroleum Geology, 34(1), 4-30.

Brun, J. P., & Fort, X. (2018). Growth of continental shelves at salt margins. Frontiers in Earth Canada-Nova Scotia Offshore Petroleum Board's (CNSOPB) 2013 Call for Bids NS13-1 (www.cnsopb.ns.ca)

Burrows, L.C., Haeri, F., Cvetic, P., Sanguinito, S., Shi, F., Tapriyal, D., Goodman, A. and Enick, R.M., 2020. A literature review of CO2, natural gas, and water-based fluids for enhanced oil recovery in unconventional reservoirs. Energy & Fuels, 34(5), pp.5331-5380.

Calhoun, G. G., & Hawkins, J. L. (2002). Effects of Earth Tides on Vertical Migration. AAPG HEDBERG CONFERENCE.

Campbell, D. C. (2019). CCGS Hudson Expedition 2016-011, phase 2. Cold seep investigations on the Scotian Slope, offshore Nova Scotia, June 15–July 6, 2016. Geological Survey of Canada, Open File, 8525, 88.

Campbell, D. C., Shimeld, J., Deptuck, M. E., & Mosher, D. C. (2015). Seismic stratigraphic framework and depositional history of a large Upper Cretaceous and Cenozoic depocenter off southwest Nova Scotia, Canada. Marine and Petroleum Geology, 65, 22-42.

Campbell, D.C. and MacDonald, A.W.A. (2016). CCGS Hudson Expedition 2015-018-Geological investigation of potential seabed seeps along the Scotian Slope, June 25-July 9, 2015. Geological Survey of Canada Open File 8116. https://doi.org/10.4095/299390

Ciotoli, G., Procesi, M., Etiope, G. et al. Influence of tectonics on global scale distribution of geological methane emissions. Nat Commun 11, 2305 (2020). https://doi.org/10.1038/s41467-020-16229-1

Clark, J. F., Washburn, L., Hornafius, J. S., & Luyendyk, B. P. (2000). Dissolved hydrocarbon flux from natural marine seeps to the southern California Bight. Journal of Geophysical Research: Oceans, 105(C5), 11509-11522.

CNSOPB-Canada-Nova Scotia Offshore Petroleum Board. (2008). Annual Report 2007-2008. Halifax, NS. https://publications.gc.ca/site/eng/9.836365/publication.html

Dai, J., Yang, S., Chen, H., & Shen, X. (2005). Geochemistry and occurrence of inorganic gas accumulations in Chinese sedimentary basins. Organic Geochemistry, 36(12), 1664-1688.

Dake, L. P., & Ershaghi, I. (1996). The Practice of Reservoir Engineering. Journal of Petroleum Science and Engineering, 3(14), 263.

Decalf, C. C., & Heyn, T. (2022). Salt geometry in the Central Basin of the Nova Scotia passive margin, offshore Canada based on new seismic data. Marine and Petroleum Geology, 106065.

Dembicki Jr, H., & Samuels, B. M. (2007). Identification, characterization, and ground truthing of deepwater thermogenic hydrocarbon macroseepage utilizing high-resolution AUV geophysical data. In Offshore Technology Conference (pp. OTC-18556). OTC.

DNRR- Department of Natural Resources and Renewables Nova Scotia (DNRR). 2010 (April). 12-year retrospective of natural gas production in Nova Scotia. Province of Nova Scotia, Halifax, NS. File no. 1049179.

Donval, J. P., Charlou, J. L., & Lucas, L. (2008). Analysis of light hydrocarbons in marine sediments by headspace technique: Optimization using design of experiments. Chemometrics and intelligent laboratory systems, 94(2), 89-94.

Douglas, P. M., Stolper, D. A., Eiler, J. M., Sessions, A. L., Lawson, M., Shuai, Y., ... & Kitchen, N. (2017). Methane clumped isotopes: Progress and potential for a new isotopic tracer. Organic Geochemistry, 113, 262-282.

Douglas, P. M., Stolper, D. A., Eiler, J. M., Sessions, A. L., Lawson, M., Shuai, Y., & Niemann, M., (2017). Methane clumped isotopes: progress and potential for a new isotopic tracer. Organic geochemistry, 113, 262-282.

Duarte, L.V., Silva, R.L. Oliveira, L.C.V., Comas-Rengifo, M.J., Silva, F. (2010). Organic-Rich facies in the Sinemurian and Pliensbachian of the Lusitanian Basin, Portugal: Total organic carbon distribution and relation to transgressive-regressive facies cycles. Geol. Acta. 8, 325-340.

Duggan-Haas, D. A., Ross, R. M., & Allmon, W. D. (2013). The science beneath the surface: a very short guide to the Marcellus Shale. Paleontological Research Institution.

Dupré, S., Mascle, J., Foucher, J. P., Harmegnies, F., Woodside, J., & Pierre, C. (2014). Warm brine lakes in craters of active mud volcanoes, Menes caldera off NW Egypt: evidence for deep-rooted thermogenic processes. Geo-Marine Letters, 34, 153-168.

Dutkiewicz, A., Volk, H., Ridley, J., & George, S. C. (2004). Geochemistry of oil in fluid inclusions in a middle Proterozoic igneous intrusion: implications for the source of hydrocarbons in crystalline rocks. Organic geochemistry, 35(8), 937-957.

Dyman, T. S., Spencer, C. W., & Baird, J. K. (1997). Geologic and production characteristics of deep natural gas resources based on data from significant fields and reservoirs, Chapter C. Geologic controls of deep natural gas resources in the United States. US Geological Survey Bulletin, 19-38.

Eiler, J. M., Clog, M., Magyar, P., Piasecki, A., Sessions, A., Stolper, D., ... & Schwieters, J. (2013). A high-resolution gas-source isotope ratio mass spectrometer. International Journal of Mass Spectrometry, 335, 45-56.

El Ayouty, M. K. (2017). Petroleum geology. In The geology of Egypt (pp. 567-600). Routledge.

Enachescu, M. E., & Hogg, J. R. (2005). Exploring for Atlantic Canada's next giant petroleum discovery. CSEG Recorder, 30(5), 19-30.

Etiope, G. (2015). Natural gas seepage. The Earth's hydrocarbon degassing.

Etiope, G., & Sherwood Lollar, B. (2013). Abiotic methane on Earth. Reviews of Geophysics, 51(2), 276-299.

Et-Touhami, M., Olsen, P.E., Kent, D.V. (2012). Potential source rocks of Late Triassic-Early Jurassic Synrift deposits in Morocco. Salon International des Energies (SIDE), International Energy Exhibition & Conference Oil, Gas, Mining, RnE, Palais des Congrès –Marrakech, Maroc.

Faramawy, S., Zaki, T., & Sakr, A. E. (2016). Natural gas origin, composition, and processing: A review. Journal of Natural Gas Science and Engineering, 34, 34-54.

Gao, Y., Wang, Y., Lee, H. S., & Jin, P. (2022). Significance of anaerobic oxidation of methane (AOM) in mitigating methane emission from major natural and anthropogenic sources: a review of AOM rates in recent publications. Environmental Science: Advances, 1(4), 401-425.

Gay, A., Lopez, M., Berndt, C., & Seranne, M. (2007). Geological controls on focused fluid flow associated with seafloor seeps in the Lower Congo Basin. Marine Geology, 244(1-4), 68-92.

Gluyas, J. G., & Swarbrick, R. E. (2021). Petroleum geoscience. John Wiley & Sons.

Greinert, J., Bohrmann, G., & Suess, E. (2001). Gas hydrate-associated carbonates and methane-venting at Hydrate Ridge: classification, distribution and origin of authigenic lithologies. Geophysical Monograph-American Geophysical Union, 124, 99-114.

Heeschen, K. U., Collier, R. W., de Angelis, M. A., Suess, E., Rehder, G., Linke, P., & Klinkhammer, G. P. (2005). Methane sources, distributions, and fluxes from cold vent sites at Hydrate Ridge, Cascadia Margin. Global Biogeochemical Cycles, 19(2).

Hélène, O., Karine, O., Stéphanie, D., Carla, S., Anne-Sophie, A., Clément, G., & Livio, R. (2020). Geological and biological diversity of seeps in the Sea of Marmara. Deep Sea Research Part I: Oceanographic Research Papers, 161, 103287.

Hovland, M., Jensen, S., & Fichler, C. (2012). Methane and minor oil macro-seep systems—their complexity and environmental significance. Marine Geology, 332, 163-173.

Hunt JM (1996) Petroleum geochemistry and geology. W.H. Freeman and Co, New York, 743.

Ivanov, A. Y., Matrosova, E. R., Kucheiko, A. Y., Filimonova, N. A., Evtushenko, N. V., Terleeva, N. V., & Libina, N. V. (2020). Search and detection of natural oil seeps in the seas surrounding the Russian federation using spaseborne SAR imagery. Izvestiya, Atmospheric and Oceanic Physics, 56, 1590-1604.

Jackson, M. P., & Hudec, M. R. (2017). Salt tectonics: Principles and practice. Cambridge University Press.

Jin, Z., Zhang, J., & Tang, X. (2022). Unconventional natural gas accumulation system. Natural Gas Industry B, 9(1), 9-19.

Jin, Z., Zhang, L., Wang, Y., Cui, Y., & Milla, K. (2009). Using carbon, hydrogen and helium isotopes to unravel the origin of hydrocarbons in the Wujiaweizi area of the Songliao Basin, China. Episodes Journal of International Geoscience, 32(3), 167-176.

Joye, S. B. (2020). The geology and biogeochemistry of hydrocarbon seeps. Annual Review of Earth and Planetary Sciences, 48, 205-231.

Judd, A., & Hovland, M. (2009). Seabed fluid flow: the impact on geology, biology and the marine environment. Cambridge University Press.

Judd, A., & Hovland, M. (2009). Seabed fluid flow: the impact on geology, biology and the marine environment. Cambridge University Press.

Karim, A., Hanley, J. J., Pe-Piper, G., & Piper, D. J. (2012). Paleohydrogeological and thermal events recorded by fluid inclusions and stable isotopes of diagenetic minerals in Lower Cretaceous sandstones, offshore Nova Scotia, Canada. AAPG bulletin, 96(6), 1147-1169.

Kessler, J. D., Reeburgh, W. S., Southon, J., & Varela, R. (2005). Fossil methane source dominates Cariaco Basin water column methane geochemistry. Geophysical Research Letters, 32(12).

Khilyuk, L. F., Chilingar, G. V., Robertson, J. O., & Endres, B. (2000). Typical composition of natural gases. Gas Migration, 238.

Kidnay, A. J., Parrish, W. R., & McCartney, D. G. (2019). Fundamentals of natural gas processing. CRC press.

Kohnert, K., Serafimovich, A., Metzger, S., Hartmann, J., & Sachs, T. (2017). Strong geologic methane emissions from discontinuous terrestrial permafrost in the Mackenzie Delta, Canada. Scientific Reports, 7(1), 5828.

Kvenvolden, K. A., & Lorenson, T. D. (2000). Methane and other hydrocarbon gases in sediment from the southeastern North American continental margin. In Proceedings of the Ocean Drilling Program, Scientific Results (Vol. 164, pp. 29-36). College Station Texas.

LeBlanc, C., Louden, K., & Mosher, D. (2007). Gas hydrates off eastern Canada: Velocity models from wide-angle seismic profiles on the Scotian Slope. Marine and Petroleum Geology, 24(5), 321-335.

Liu, Q., & Liu, Y. (2016). Clumped-isotope signatures at equilibrium of CH4, NH3, H2O, H2S and SO2. Geochimica et Cosmochimica Acta, 175, 252-270.

Løseth, H., Wensaas, L., Arntsen, B., Hanken, N. M., Basire, C., & Graue, K. (2011). 1000 m long gas blow-out pipes. Marine and Petroleum Geology, 28(5), 1047-1060.

Lu, Z., Rao, Z., He, J., Zhu, Y., Zhang, Y., Liu, H., Wang, T. and Xue, X. (2015). Geochemistry of drill core headspace gases and its significance in gas hydrate drilling in Qilian Mountain permafrost. Journal of Asian Earth Sciences, 98, 126-140.

Luheshi, M., Roberts, D. G., Nunn, K., Makris, J., Colletta, B., Wilson, H., ... & Dubille, M. (2012). The impact of conjugate margins analysis on play fairway evaluation–an analysis of the hydrocarbon potential of Nova Scotia. first break, 30(1).

MacDonald, I. R., Leifer, I., Sassen, R., Stine, P., Mitchell, R., & Guinasso Jr, N. (2002). Transfer of hydrocarbons from natural seeps to the water column and atmosphere. Geofluids, 2(2), 95-107.

Magoon, L. B., & Dow, W. G. (1991). The petroleum system-from source to trap. AAPG Bulletin (American Association of Petroleum Geologists) ;(United States), 75(CONF-910403-).

Mao, S. H., Zhang, H. H., Zhuang, G. C., Li, X. J., Liu, Q., Zhou, Z., ... & Yang, G. P. (2022). Aerobic oxidation of methane significantly reduces global diffusive methane emissions from shallow marine waters. Nature communications, 13(1), 7309.

Marcon, Y., Ondréas, H., Sahling, H., Bohrmann, G., & Olu, K. (2014). Fluid flow regimes and growth of a giant pockmark. Geology, 42(1), 63-66.

McCabe, P.J. (2012). Oil and Natural Gas: Global Resources. In: Malhotra, R. (eds) Fossil Energy. Encyclopedia of Sustainability Science and Technology Series. Springer, New York, NY. https://doi.org/10.1007/978-1-4939-9763-3_71

Meister, P., Liu, B., Ferdelman, T. G., Jørgensen, B. B., & Khalili, A. (2013). Control of sulphate and methane distributions in marine sediments by organic matter reactivity. Geochimica et Cosmochimica Acta, 104, 183-193.

Milkov, A. V. (2011). Worldwide distribution and significance of secondary microbial methane formed during petroleum biodegradation in conventional reservoirs. Organic Geochemistry, 42(2), 184-207.

Milkov, A. V., & Etiope, G. (2018). Revised genetic diagrams for natural gases based on a global dataset of> 20,000 samples. Organic Geochemistry, 125, 109-120.

Milkov, A. V., Vogt, P. R., Crane, K., Lein, A. Y., Sassen, R., & Cherkashev, G. A. (2004). Geological, geochemical, and microbial processes at the hydrate-bearing Håkon Mosby mud volcano: a review. Chemical Geology, 205(3-4), 347-366.

MoH. Wilson, M. Luheshi, and B. Colletta. (2011). "Detailed play fairway analysis sheds new light in Nova Scotia offshore,"Oil Gas J. 109, 48–63, 127 (2011).

Mokhatab, S., Poe, W. A., & Mak, J. Y. (2018). Handbook of natural gas transmission and processing: principles and practices. Gulf professional publishing.

Mokhatab, S., Poe, W.A., Speight, J.G. (2006). Handbook of Natural Gas Transmission and Processing. Elsevier, Amsterdam.

Mukhopadhyay, P. K. M., Brown, D. E., Kidston, A. G., Bowman, T. D., Faber, J., & Harvey, P. J. (2003). Petroleum systems of deepwater Scotian Basin, Eastern Canada: challenges for finding oil versus gas provinces. In Offshore Technology Conference. Offshore Technology Conference.

Nova Scotia Energy Department, 2011. Play Fairway Analysis (PFA) offshore Nova Scotia Canada. Published report. http://www.novascotiaoffshore.com/analysis

Oil, N. (2018). Gas Annual Report 2013. URL: http://www.aadncaandc.gc.ca/eng/1367341676920/1367341870731

Oliveira, L.C.V., Rodrigues, R., Duarte, L.V., Lemos, V., (2006). Avaliação do potencial gerador de petróleo e interpretação paleoambiental com base em biomarcadorese isótopos estáveis do carbono da seção Pliensbaquiano-Toarciano inferior (Jurássico inferior) da região de Peniche (Bacia Lusitânica, Portugal). Boletim de Geociências da Petrobras 14, 207-234.

Ono, S., Wang, D. T., Gruen, D. S., Sherwood Lollar, B., Zahniser, M. S., McManus, B. J., & Nelson, D. D. (2014). Measurement of a doubly substituted methane isotopologue, 13CH3D, by tunable infrared laser direct absorption spectroscopy. Analytical Chemistry, 86(13), 6487-6494.

Owino, Y. D. (2023). Integrative ArcGIS mapping study of direct hydrocarbon indicators within the Shelburne Subbasin of the Scotian Slope, Nova Scotia.

Pang, X. (2004). The Pearl River deep-water fan system & petroleum in South China Sea. Science In.

Pape, T., Bahr, A., Klapp, S. A., Abegg, F., & Bohrmann, G. (2011). High-intensity gas seepage causes rafting of shallow gas hydrates in the southeastern Black Sea. Earth and Planetary Science Letters, 307(1-2), 35-46.

Pe-Piper, G., Triantafyllidis, S., & Piper, D. J. (2008). Geochemical identification of clastic sediment provenance from known sources of similar geology: the Cretaceous Scotian Basin, Canada. Journal of Sedimentary research, 78(9), 595-607.

Pettingill, H. S. (2001). Giant field discoveries of the 1990s. The Leading Edge, 20(7), 698-704.

Pettingill, H. S. (2001). Global deep water exploration: Past, present and future frontiers, Petroleum systems of deep-water basins: Global and Gulf of Mexico experience. In Gulf Coast Section SEPM Foundation 21^< st> Annual Bob F. Perkins Research Conference, 2001.

Play Fairway Analysis: https://energy.novascotia.ca/oil-and-gas/offshore/play-fairway-analysis

Pohlman, J.W., Bauer, J.E., Canuel, E.A., Grabowski, K.S., Knies, D.L., Mitchell, C.S., Whiticar, M.J. and Coffin, R.B. (2009). Methane sources in gas hydrate-bearing cold seeps: Evidence from radiocarbon and stable isotopes. Marine Chemistry, 115(1-2), 102-109.

Potter II, R. W., Harrington, P. A., Sulliman, A. H., & Viellenave, J. H. (1996). Significance of geochemical anomalies in hydrocarbon exploration: one company's experience.

Racey, A. (2011). Petroleum geology. Geological Society of London.

Rasheed, M. A., Rao, P. S., Annapurna, B., & Hasan, S. Z. (2015). Implication of soil gas method for prospecting of hydrocarbon microseepage. Int J Petrol Petrochem Eng, 1(1), 31-41.

Rice, D. D., & Claypool, G. E. (1981). Generation, accumulation, and resource potential of biogenic gas. AAPG bulletin, 65(1), 5-25.

Rider, M. H. (2003). The Geological Interpretation of Well Logs (2nd ed.). Whittles Publishing. ISBN-13: 978-1870325411

Rojey, A., Jaffret, C., Cornot-Gandolphe, S., Durand, B., Julian, S., Valais, M. (1997). Natural Gas: Production, Processing, Transport. Editions Technip, Paris.

Ryder, R. T., & Zagorski, W. A. (2003). Nature, origin, and production characteristics of the Lower Silurian regional oil and gas accumulation, central Appalachian basin, United States. AAPG bulletin, 87(5), 847-872.

Sachse, V.F., Leythaeuser, D., Grobe, A., Rachidi, M., Littke. R., (2012). Organic Geochemistry and Petrology of a Lower Jurassic (Pliensbachian) Petroleum Source Rock from Aït Moussa, Middle Atlas, Morocco. Journal Petroleum Geology, 35, 5-24.

Schoell, M. (1983). Genetic characterization of natural gases. AAPG bulletin, 67(12), 2225-2238.

Schroot, B. M., & Schüttenhelm, R. T. E. (2003). Expressions of shallow gas in the Netherlands North Sea. Netherlands Journal of Geosciences, 82(1), 91-105.

Selley, R. C. (1998). Elements of Petroleum Geology (2nd ed.). Academic Press. ISBN-13: 978-0126363708

Selley, R. C. (1998). Elements of petroleum geology. Gulf Professional Publishing.

Serié, C., Huuse, M., & Schødt, N. H. (2012). Gas hydrate pingoes: Deep seafloor evidence of focused fluid flow on continental margins. Geology, 40(3), 207-210.

Sheriff, R. E., & Geldart, L. P. (1995). Exploration Seismology (2nd ed.). Cambridge University Press. ISBN-13: 978-0521468268

Silva, R.L., Duarte, L.V., Comas-Rengifo, M.J., Mendonça Filho, J.G., Azerêdo, A.C., (2011). Update of the carbon and oxygen isotopic records of the Early-Late Pliensbachian (Early Jurassic, ~187 Ma): Insights from the organic-rich hemipelagic series of the Lusitanian Basin (Portugal). Chemical Geology, 283, 177-184.

Smith, B. M., Makrides, C., Altheim B. and Kendell K. (2014). Resource Assessment of Undeveloped Significant Discoveries on the Scotian Shelf, Canada-Nova Scotia Offshore Petroleum Board, 182.

Song, C., Jiang, S., Wen, Z., & Wang, Z. (2020). Comparison of the petroleum geology in the deep-water basins between the passive margin of Morocco and its conjugate margin of Canada. Journal of Earth Science, 31(5), 919-929.

Sparrow, Katy J., John D. Kessler, John R. Southon, Fenix Garcia-Tigreros, Kathryn M. Schreiner, Carolyn D. Ruppel, John B. Miller, Scott J. Lehman, and Xiaomei Xu. (2018). Limited contribution of ancient methane to surface waters of the US Beaufort Sea shelf. Science advances, 4(1), eaao4842.

Speight, J. G. (2015). Liquid fuels from natural gas. Handbook of alternative Fuel technologies, 1, 153-170.

Speight, J. G. (2018). Natural gas: a basic handbook. Gulf Professional Publishing.

Speight, J.G. (2007). Natural Gas: a Basic Handbook. Gulf Publishing Company, Houston, Texas.

Spiess, V., Fekete, N., Ding, F., Caparachin, C., & Foucher, J. (2008, December). Gas and Fluid Expulsion at the Congo continental margin identfied from seismoacoustic data. In AGU Fall Meeting Abstracts (Vol. 2008, pp. OS32A-04).

Stolper D., Martini A., Clog M., Douglas P., Shusta S., Valentine D., Sessions A. & Eiler J. (2015). Distinguishing and understanding thermogenic and biogenic sources of methane using multiply substituted isotopologues. Geochim. Cosmochim. Acta 161, 219–247.

Stolper D., Sessions A., Ferreira A., Santos Neto. E., Schimmelmann A., Shusta S., Valentine D. & Eiler J. (2014a). Combined 13C–D and D–D clumping in methane: methods and preliminary results. Geochim. Cosmochim. Acta 126, 169–191.

Stolper, D. A., Lawson, M., Davis, C. L., Ferreira, A. A., Neto, E. S., Ellis, G. S. & Sessions, A. L. (2014c). Formation temperatures of thermogenic and biogenic methane. Science, 344(6191), 1500-1503.

Tagliabue, M., Farrusseng, D., Valencia, S., Aguado, S., Ravon, U., Rizzo, C., Corma, A., Mirodatos, C. (2009). Natural gas treating by selective adsorption: material science and chemical engineering interplay. Chem. Eng. J. 155, 533e566.

Thiagarajan, N., Kitchen, N., Xie, H., Ponton, C., Lawson, M., Formolo, M., & Eiler, J. (2020). Identifying thermogenic and microbial methane in deep water Gulf of Mexico Reservoirs. Geochimica et Cosmochimica Acta, 275, 188-208.

Thiagarajan, N., Xie, H., Ponton, C., Kitchen, N., Peterson, B., Lawson, M., Formolo, M., Xiao, Y. and Eiler, J. (2020). Isotopic evidence for quasi-equilibrium chemistry in thermally mature natural gases. Proceedings of the National Academy of Sciences, 117(8), pp.3989-3995.

Torres, M.E., McManus, J., Hammond, D.E., De Angelis, M.A., Heeschen, K.U., Colbert, S.L., Tryon, M.D., Brown, K.M. and Suess, E. (2002). Fluid and chemical fluxes in and out of sediments hosting methane hydrate deposits on Hydrate Ridge, OR, I: Hydrological provinces. Earth and Planetary Science Letters, 201(3-4), 525-540.

Valentine, D. L. (2011). Emerging topics in marine methane biogeochemistry. Annual review of marine science, 3, 147-171.

Ventura, G. T., Chowdhury, A., Lalk, E., Ono, S., Dooma, J. M., MacDonald, A. W., ... & Bennett, R. (2023, July). Methane formation and its isotopic alteration at two active deep ocean cold seeps from the scotian slope of atlantic canada. In Goldschmidt 2023 Conference. GOLDSCHMIDT. https://doi.org/10.3997/2214-4609.202333194

Walters, C. C. (2017). Origin of petroleum. Springer Handbook of Petroleum Technology, 359-379.

Webb, M. A., & Miller III, T. F. (2014). Position-specific and clumped stable isotope studies: comparison of the Urey and path-integral approaches for carbon dioxide, nitrous oxide, methane, and propane. The Journal of Physical Chemistry A, 118(2), 467-474.

Weimer, P., & Pettingill, H. S. (2007). Deep-water exploration and production: A global overview.

Weimer, P., Slatt, R. M., Bouroullec, R., Fillon, R., Pettingill, H., Pranter, M., & Tari, G. (2006). Introduction to the petroleum geology of deepwater setting. American Association of Petroleum Geologists.

Wenau, S., Spiess, V., Pape, T., & Fekete, N. (2015). Cold seeps at the salt front in the Lower Congo Basin II: The impact of spatial and temporal evolution of salt-tectonics on hydrocarbon seepage. Marine and Petroleum Geology, 67, 880-893.

Wesley, D., Dallimore, S., MacLeod, R., Sachs, T., & Risk, D. (2023). Characterization of atmospheric methane release in the outer Mackenzie River delta from biogenic and thermogenic sources. The Cryosphere, 17(12), 5283-5297.

Whiticar, M. J. (1994). Correlation of natural gases with their sources: Chapter 16: Part IV. Identification and Characterization.

Whiticar, M. J. (1999). Carbon and hydrogen isotope systematics of bacterial formation and oxidation of methane. Chemical Geology, 161(1-3), 291-314.

Whiticar, M. J., & Faber, E. (1986). Methane oxidation in sediment and water column environments—isotope evidence. Organic Geochemistry, 10(4-6), 759-768.

Wuebbles, D. J., & Hayhoe, K. (2002). Atmospheric methane and global change. Earth-Science Reviews, 57(3-4), 177-210.

Xie, H., Dong, G., Formolo, M., Lawson, M., Liu, J., Cong, F., ... & Eiler, J. (2021). The evolution of intra-and inter-molecular isotope equilibria in natural gases with thermal maturation. Geochimica et Cosmochimica Acta, 307, 22-41.

Young, E. D., Kohl, I. E., Lollar, B. S., Etiope, G., Rumble Iii, D., Li, S., & Bryndzia, L. T. (2017). The relative abundances of resolved l2CH2D2 and 13CH3D and mechanisms controlling isotopic bond ordering in abiotic and biotic methane gases. Geochimica et Cosmochimica Acta, 203, 235-264.

Young, E. D., Rumble III, D., Freedman, P., & Mills, M. (2016). A large-radius high-mass-resolution multiple-collector isotope ratio mass spectrometer for analysis of rare isotopologues of O2, N2, CH4 and other gases. International Journal of Mass Spectrometry, 401, 1-10.

Zhang, N., Snyder, G. T., Lin, M., Nakagawa, M., Gilbert, A., Yoshida, N. & Sekine, Y. (2021). Doubly substituted isotopologues of methane hydrate (13CH3D and 12CH2D2): Implications for methane clumped isotope effects, source apportionments and global hydrate reservoirs. Geochimica et Cosmochimica Acta, 315, 127-151.

Zhi-jun, J. I. N., & Jin-chuan, Z. H. A. N. G. (2003). Two typical types of mechanisms and models for gas accumulations. Acta Petrolei Sinica, 24(4), 13.

Zhuo, Q. G., Meng, F. W., Zhao, M. J., Li, Y., Lu, X. S., & Ni, P. (2016). The salt chimney effect: delay of thermal evolution of deep hydrocarbon source rocks due to high thermal conductivity of evaporites. Geofluids, 16(3), 440-451.

Chapter 2. Do Poorly Stored, Deep Marine Sediments Contain Useful Methane Signatures for Gas Geochemical Study?

Abstract

Methane is a highly volatile gas commonly found in deeply buried sediments. It easily escapes into the atmosphere and is largely oxidized in sediments making it difficult to contain and measure by most sampling techniques. Nonetheless, the measurement of methane is increasingly important as it, in association with sulfate, marks the boundary to the fundamental microbial process like anaerobic oxidation of methane in marine sediments. This study investigates the outcomes of measuring free phase methane gas concentrations sourced from poorly preserved sediments lacking traditional sampling protocols. Four complimentary experiments were performed, including two laboratory-based experiments. The first experiment examined the long-term sealing capability of Isojars. This experiment demonstrated that even when proper protocols are followed, within the first nine months of cold storage, frozen 500 mL plastic Isojars will likely leak more than 75.5% of their initially stored headspace gas. Given this, a second experiment was initiated that tested whether ice trapped in sediment porewater can better preserve methane and therefore be used to qualitatively measure gas concentrations when the headspace gas has been lost. In this second experiment known volumes of frozen methane-rich sediment were isolated in crimp-top, sealed serum vials. Methane concentrations were measured at the moment of sediment collection after sample retrieval from the ocean floor. The initial concentrations were then compared with a second analysis that followed one year of cold storage to determine the amount of methane released as porewater gas. For this experiment, substantial loss of methane was also observed. However, the remaining gas concentrations were statistically correlated to their initial sediment loadings suggesting that a meaningful signal could be extracted from the depleted frozen sediments – a sample characteristic we termed “methane loss”. Based on the results of this latter experiment, two

further field-related studies were performed. The first field study examined whether residual methane concentrations from poorly preserved sediment samples could still be used to track methane variations in sediments by comparing the relative gas concentrations to that of equivalent samples, which were more carefully preserved in Isojars. The second field experiment examined whether headspace methane gas concentrations yielded qualitatively meaningful stratigraphic interpretations about the natural abundance of methane present in deep marine sediments by comparing residual gas compositional trends to that of porewater anion variations. The findings from two laboratory experiments and comparative data analyses demonstrated that.: *i*) glass vials with rubber butyl septa and aluminium caps are best for long term headspace gas storage, *ii*) methane in unconfined frozen sediment samples are comparable to confined sediment samples. They can be used to resolve natural variations in *in situ* methane abundances from confined samples collected from the least bioturbated shallow sediment zones. The two field survey experiments further demonstrated that cores with methane concentrations >10,000 ppm can retain a usable methane gas for more than two years. These samples can be used to interpretate biogeochemically controlled stratigraphic methane trends such as the sulfate methane transition zone. From these surveys, in combination with comparisons to additional sulfate and carbonate data, the localized Scotian Slope sulfate methane transition zone for two eligible samples from 2016 cruise is purposed to be occur at ~2.0–4.5 mbsf.

2.1. Introduction

Shallow sea sediment (1-100 cm) serves as a repository of vital information about the subsurface hydrocarbon system and subsurface bio-geochemical interaction (Zhuang et al., 2019), with gas geochemistry playing a crucial role in deciphering this wealth of data (Torres et al., 2002). Drilling corers (Diplas and Fripp, 1992) are essential tools in extracting sediment cores (NMEP_Report, 2024) from the ocean floor, enabling scientists to access these invaluable records (LSASD_Report, 2023). Gas geochemistry involves the analysis of gases trapped within the sediment layers, providing insights into gas sources, gas generation process and subsurface microbial activity (Danovaro, 2014). Methane, for example, can indicate the presence of degraded organic matter, organic-rich source rock, petroleum generation and microbial activity, while carbon dioxide levels can reflect changes in oceanic circulation and climate (Kvenvolden and Lorenson, 2000).

By studying these gases, their fluctuation with depth, alongside other sediment properties (e.g., porosity, porewater geochemistry and organic matter abundance) (Dong et al, 2023), researchers can construct subsurface biogeochemical zones, track the evolution of marine ecosystems (Peoples et al., 2019) and understand the dynamics of global carbon cycling. To study the subsurface biogeochemical zone, downcore profiles are build tracking the enrichment and depletion of these gases (Hong et al., 2013) and other compound with sediment depth. Within the deep ocean, subsurface oxygen and sulfate levels decrease with sediment depth (Zhuang et al., 2019). Within anoxic sediments methane concentrations increase. This is particularly evident at the sulfate methane transition zone (SMTZ) where sulfate and methane cycling is microbially linkedvia the anaerobic oxidation of methane (AOM), which is responsible for consuming a majority (90%) of subsurface methane. The SMTZ is involved in regulating the release and production of methane and act as an indicator for high methane flux (Hu et al, 2017). Moreover, the downcore profile and

gas geochemistry helps in assessing the extent of these zones (sulfate reducing, SMTZ), estimating the natural gas hydrate sources and reserves (Torres et al., 2002) and identifying potential energy resources. Thus, the synergy between sediment cores and gas geochemistry (Smith and Johnson, 2020) is instrumental in advancing our understanding of the hydrocarbon (includes oil and natural gas) pathways, conversion of organic matter to hydrocarbons, estimating methane flux, and guiding sustainable resource management strategies.

The most accurate retrieval of shallow sediment from the ocean floor is achieved using push corers (Fig. 1C) from a remotely operated vehicle (ROV) or manned submersible (Johnson and Brown, 2019). Gas geochemists analyze the composition and concentration of interstitial gases in sediment cores to assess active petroleum systems in deep sea basins (Kvenvolden and Lorenson, 2000; Torres et al., 2002). However, obtaining samples for free phase hydrocarbon gas analysis is challenging due to their high volatility, necessitating immediate processing onboard the research vessel (Weisman, 1998). To prevent loss and degradation of gas samples, subsurface sediment samples for gas analysis are collected in specially designed airtight jars (Fig. 2.2D, Fig. 2.2E) for headspace gas analysis (Tipler, 2013; Dong et al, 2023). Headspace gas refers to the gas phase above a liquid or solid sample. This gas phase contains volatile compounds that have evaporated from the sample into the headspace of an Isojar/glass jar during desorption of gas from sediment cores. Headspace analysis is a non-mechanical method widely used by the petroleum industry to analyze the extracted interstitial gases from near-surface sediments. The headspace of the jars is typically flushed with inert gas before sealing to maintain anoxic conditions (US EPA, 2001; Gresov et al., 2016). Gas geochemical analyses are ideally performed onboard the research vessel (Miller and Thompson, 2021) or as soon as possible after collection (within a month) (Campbell, 2019). However, studying the post-preservation effects of these samples is limited by their

lifespan, storage requirements, transportation hazards, and associated costs (Voskuil, 1991). Investigating these effects could offer insights into improved storage methods and increase sample reusability.

2.1.1. The Scotian Slope and coring surveys

The Scotia Slope, offshore Nova Scotia (Fig. 2.1A), comprises an integral component of the Atlantic in Eastern Canada that is well known for its potential hydrocarbon reserves (Campbell, 2019). Five coring surveys (Fowler and Webb, 2018) have been conducted to estimate these resources using different surveying techniques (Fowler and Webb, 2015; Fowler and Webb, 2016; Fowler and Webb, 2018; Fowler et al., 2018). The samples for the present study (Fowler and Webb, 2015; Fowler and Webb, 2016; Fowler and Webb, 2018; Bennett and Desiage, 2022) have been acquired (2015, 2016, 2018, 2021 survey) as a part of a collaborative project between the Department of Natural and Renewable Resources (DNRR) and the University of Calgary in further collaboration with Natural Resources Canada with funding from Genome Atlantic as a Genome Application Partnership Program (GAPP), Research Nova Scotia, and Mitacs. GAPP conducted multiple geophysical and sampling surveys between 2015 and 2018, employing seismic attribute analysis and coring techniques (Fowler and Webb, 2015; Dong et al., 2023) to identify direct hydrocarbon indicators, including fluid-containing reservoirs, pockmarks, and gas vent chimneys, at the perspective seep sites.

Samples were collected from four different coring cruises in 2015, 2016, and 2018 using the CGCS Hudson (Fowler and Webb, 2015; Fowler and Webb, 2016; Fowler and Webb, 2018; Fowler et al., 2018), operated by the Bedford Oceanographic Institution. A final ROV push coring cruise was undertaken in 2021 using the Atlantic Condor operated by Helix Energy Solutions (Fig. 2.1)

and fitted with in situ modular research laboratories. The samples collected during 2015, 2016, 2018 surveys were gravity and piston core samples from the Scotian Margin.

For the 2021 ROV survey (Fig.2.1A), push cores were collected from transects and two active seep sites 2A-1 and 2B-1 (Fig. 2.1A). The discovery of these two active seep sites was a rare occurrence during the survey (Bennett and Desiage, 2022). The two active seep sites 2A-1 and 2B-1 were identified by observed seepage and visible microbial mats using live imaging survey methodology. The seabed at 2B-1 (2021 survey) is tabular in shape and characterized by sporadic bubble generation. It predominantly displays a flat terrain with significant bioturbation, evidenced by sea urchin tracks, shallow depressions possibly attributed to unknown organisms, and tubeworms. The survey area for this site is approx. 180 m × 240 m and it is located at ~2750 m water depth. The floor substrate is dominated by authigenic carbonate formations inhabited by mussels/bivalves and sessile organisms (Bennett and Desiage, 2022). Seep site 2A-1 (2021 survey) trends NW-SE, having an elongated shape characterised with continuous release of gas bubbles at the sampling station named The Hole. The survey area for this site is ~20 m × 200 m and it is located at ~2700 m water depth. The geomorphology changes near the edge, with several holes, and it is dominated by softer sediment. The substrate is comprised of authigenic carbonate formations, inhabited by mussels/bivalves and sessile organisms.

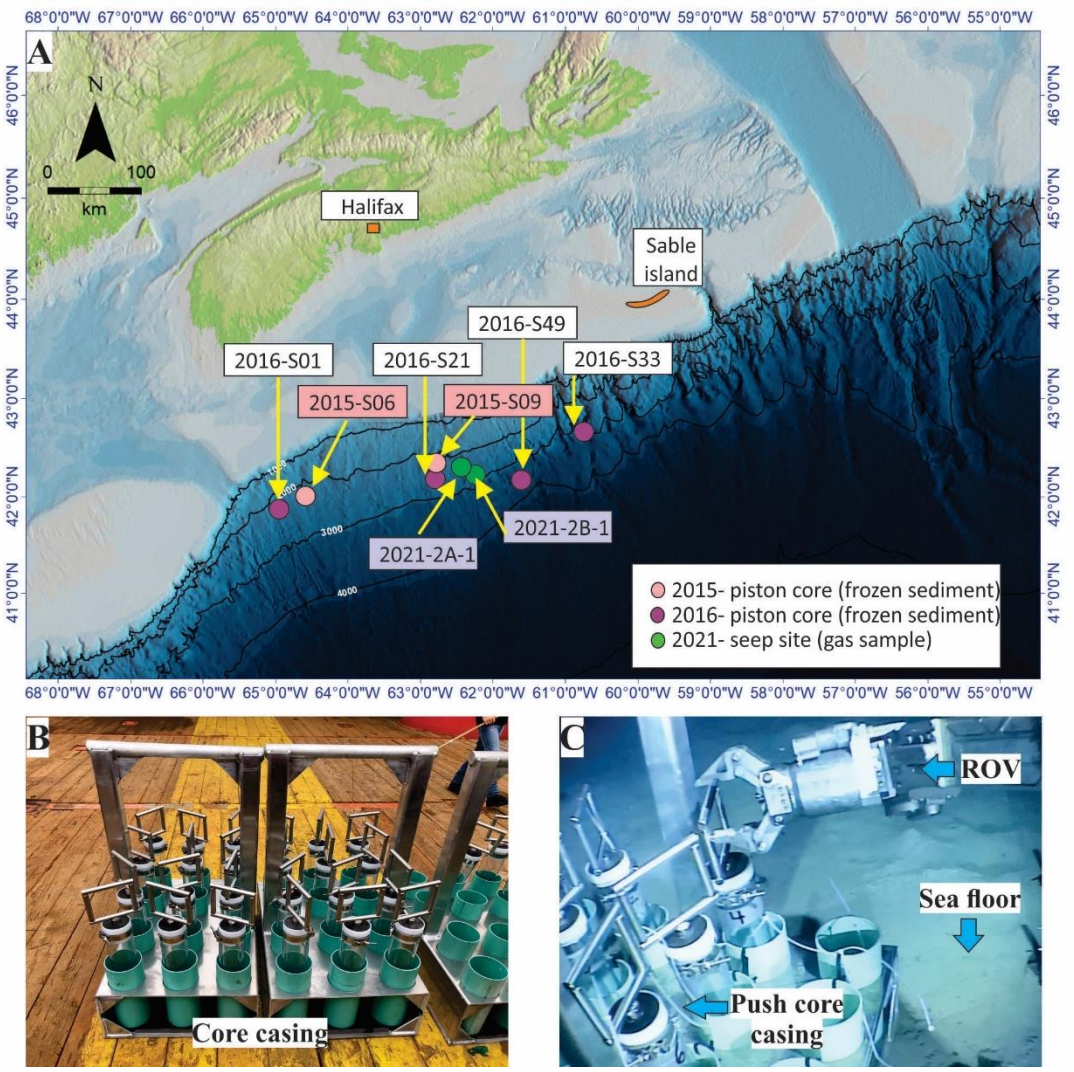

Figure 2.1. A) Map of the Scotian Slope and active seep sites marked in green (modified after Owino, 2023; Bennett and Desiage, 2022). B) Push cores baskets for sampling Scotia Slope seep sediments. B) Robotic arm of the ROV reaching for a push corer (modified after Bennett and Desiage, 2022).

2.2. Research objectives and hypothesis

This chapter describes how headspace methane gas in confined and unconfined frozen sediment samples can be impacted by long-term poor storage protocols. Furthermore, I examine methane loss with sample storage time, and the usefulness of porewater methane for unconfined frozen sediment samples through two experiments and two large-scale surveys. The results of these

studies are then used to help to identify local near surface biogeochemical zones like sulfate methane transition zone.

Our hypothesis posits that examining methane concentrations in the headspace of sediment samples obtained from the Scotian Slope through (piston, gravity and push coring methods), encompassing both confined (Isojar) and unconfined conditions, will advance our understanding of the application and the long-term viability (exceeding 1 year) of sediment gas storage. Additionally, this analysis aims to ascertain the longevity of these stored gas samples and their potential for attenuation over time.

2.3. Methodology

2.3.1. Sample description

Unconsolidated sediment core samples (Fig. 2.2 B) from 2021 survey (2A-1 and 2B-1) were used for the lab experiments and comparative study. The headspace gas measured from the sediment samples were of two types, *i*) confined sediments stored in jars (Fig. 2.2 C, Fig. 2.3 A, Fig. 2.3 B) and *ii*) unconfined sediment stored in Al foil. Both the confined and unconfined sediment samples were collected from the same seep sites (Fig. 2.2 B, Fig. 2.4). The major difference is in their storage methodology, where confined sediments are stored in airtight Isojar or serum vials designed for headspace gas analysis (Fig. 2.3 A), unconfined sediments are wrapped in Al foil and stored in Ziplock bags (Fig. 2.4).

2.3.1.1. Samples for lab-based methane preservation experiments

Confined and unconfined samples for the two lab experiments (Experiment 1 and Experiment 2) were exclusively selected from cores collected at or near 2A-1 and 2B-1 (Fig. 2.1A), 2021 ROV push core sampling sites (Fig. 2.1B, Fig. 2.1C). The samples from these sites were shown to have high gas concentrations that resulted in the formation of authigenic carbonate mounds and deep

ocean benthic fauna at these sites. Moreover, the geophysical data also indicated the presence of gas chimneys below the seep sites (Bennett and Desiage, 2022).

2.3.1.2. Samples for field-based experiments

Confined and unconfined samples for the two field experiments (Experiment 3 and Experiment 4) were selected from gravity and piston cores collected during 2015, 2016 and 2018 coring survey. These cores were 20 times deeper than 2021 push cores and have a build in library of porewater sulfate and carbonate data (Nikita, 2022).2.3.2. Sediment sample acquisition and storage methodology for on board research vessel

Most of the samples used for the survey and comparative study (Experiment 3 and Experiment 4) were gravity and piston cores (2015, 2016, 2018) (Fowler and Webb, 2015; Fowler and Webb, 2016; Fowler and Webb, 2018; Fowler et al., 2018) collected by the combined team members from APT, Calgary University and Saint Mary's University (Fowler and Webb, 2015; Fowler and Webb, 2016; Fowler and Webb, 2018). The length of the gravity and piston cores were 6 and 8 mbsf (2021 push cores max. 40 cmbsf), respectively (Fowler and Webb, 2015; Fowler and Webb, 2016; Fowler and Webb, 2018). The unconfined sediment core samples from 2015, 2016 and 2018 cruises (Fowler and Webb, 2015; Fowler and Webb, 2016; Fowler and Webb, 2018) were collected on board and wrapped in Al foil and placed in Ziploc bags. Sediment samples for gas analysis were stored in glass jars with plastic screw-top lids (termed confined sediment samples).

The push cores samples from site 2A-1 and 2B-1 were (Bennett and Desiage, 2022) collected during 2021 survey (Experiment 1 and Experiment 2) reached a maximum depth of 40 centimeters below the seafloor (cmbsf) and collected by 2021 cruise team members including Ellen Lalk, (MIT), Narges Ahangarian (SMU) and Dr. Todd Ventura (SMU) (Bennett and Desiage, 2022). Immediately following retrieval, push cores were sectioned into 2 cm thick intervals (Fig. 2.2)

onboard the research vessels (Bennett and Desiage, 2022). The unconfined samples were wrapped in Al foil and stored in -80 ℃ freezer. Three intervals from the bottom half of the core, as well as any locations displaying gas, were chosen for the geochemical analyses and stored in Isojars and serum vials as confined samples. For these intervals, sediment was scooped out of the core liner and added to an Isojar (confined) and to a 25 mL (confined) serum vial (Fig. 2.2). Several drops of NaOH were then added to the samples as a biocide and the samples were immediately frozen. Both containers were flushed with N_2 and sealed (Dong et al, 2023). The lid of each Isojar was wrapped with electrical tape and the jars were placed upside down in a -80 ˚C freezer alongside the serum vials. Interstitial gas analysis was later performed from the headspace of the Isojar (500 mL) using GC (Fowler and Webb, 2018; Fowler et al., 2018). During the 2021 cruise, additional subsamples from the Isojars were collected in separate glass vials (25 mL) for screening of the HC gases (confined). Also, six direct seep gas samples (2 sites) from the ocean floor were collected in Isobags for clumped isotope analysis.

2.3.3. Laboratory based experiments and sample preparation

The samples used for the two lab-based experiments were unconsolidated sediments stored in *i*) 500 mL Isojars or 25 mL glass vials (Fig. 2.2D, Fig. 2.2E; confined) and *ii*) frozen sediment slabs (5 – 10 cm) (stored in Ziploc bags and Al foil; unconfined) as shown in Figure 2.3C. The interstitial trapped gas accumulates in the headspace of the vial (headspace gas; Fig. 2.3) and is used for the gas analysis. In this process sediments are immediately stored in a jar after they are brought to the ship's deck (Fig. 2.2 and Fig. 2.3). They are usually flushed with inert gas before sealing (Dong et al, 2023). For this study, these samples are considered as gas released at zero time (T_0). These samples are preserved with minimum loss of gas as they are immediately stored in an -80 °C freezer.

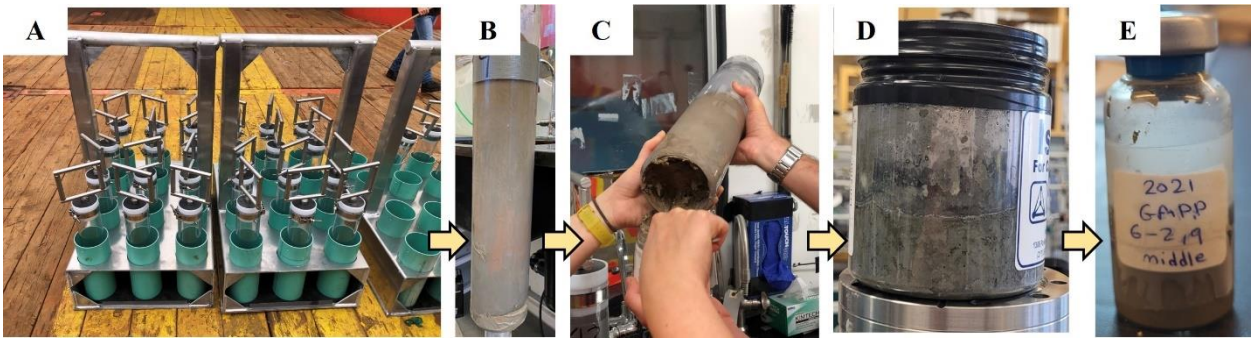

Figure 2.2. A) Core casing to retrieve sediment cores. B) Example of sediment filled core. C) Filled core sediment being scooped out for different study. D) Isojar with sediment samples for gas analysis (confined). E) Glass vial (airtight) with a smaller sample volume carrying a sub-sample for sediment headspace gas (confined).

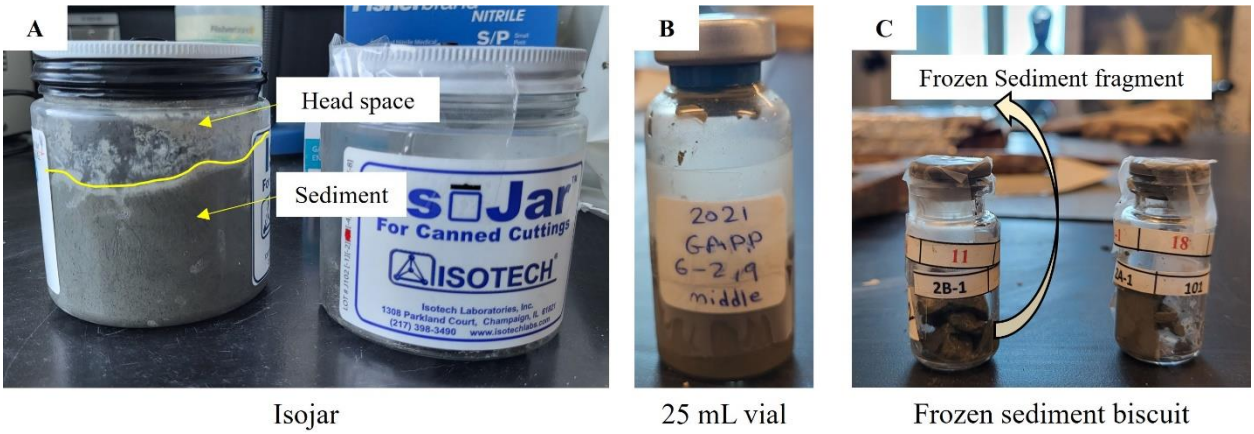

Isojar 25 mL vial Frozen sediment biscuit

Figure 2.3. A) 500 mL Isojar filled with sediment and showing the headspace. B) 25 mL vial filled with one third sediment (sub-sample). C) Glass vial (airtight) filled with frozen sediment fragments for sediment pore gas.

2.3.4. Headspace gas collection (unconfined samples)

The unconfined samples in this study consist of unsealed frozen sediment samples collected for geochemical and geomicrobiological analysis unlike the confined samples stored and frozen within the Isojar and serum vials. These samples were meticulously enveloped in aluminum foil and preserved at -80 °C until extraction and subsequent analysis (Fig. 2.4). These samples are also potentially capable of trapping small amounts of gas in their pore space. This stored gas remains trapped inside the pore space of the sediment as long as the sample is kept frozen and desorbs as

the sample is thawed. The released gas can be collected in the headspace of a sealed glass jar flushed with N_2, allowing the quantification of the pore space gas as schematically shown in Fig. 2.4. Pore gas can be released from the sediment at any time (1 month to 12 month) by thawing and is considered as gas released at time (T_x) and so on.

To obtain the trapped pore gas the frozen sediment (unconfined) was sub-sampled by quickly breaking fragments off the larger sample. The resulting shard was transferred to an airtight 25 mL glass jar (Fig. 2.3B).

2.3.5. Gas speciation analysis

All samples were analyzed using a Wasson ECE-Agilent 7890A gas chromatograph equipped with a flame ionization detector (GC-FID), in the Department of Geology at Saint Mary's University. The GC-FID system was modified with appropriate methodology (oven temp., standards) and injection systems provided by Wasson ECE Instrumentation. For the analysis of trace combustible hydrocarbon phases, an alumina-PLOT capillary analytical column (50 m × 0.53 mm × 10 um) was utilized, employing ultrapure He as the carrier gas at a flow rate of 11.9 ± 0.5 mL per minute. The initial oven temperature was maintained at 35 °C for 6 minutes before being ramped up at a rate of 10°C per min. to reach 200 °C, where it was held for 2.5 min. Samples of volumes from 100 µL to 1 mL were introduced into the chromatograph using a Hamilton airlock syringe. Identification and external calibration of gas species were carried out using standard gas mixtures supplied by Matheson Tri-Gas and SCOTTY® Specialty Gases, and Agilent ChemStation software (Kerr 2015, Kerr 2021).

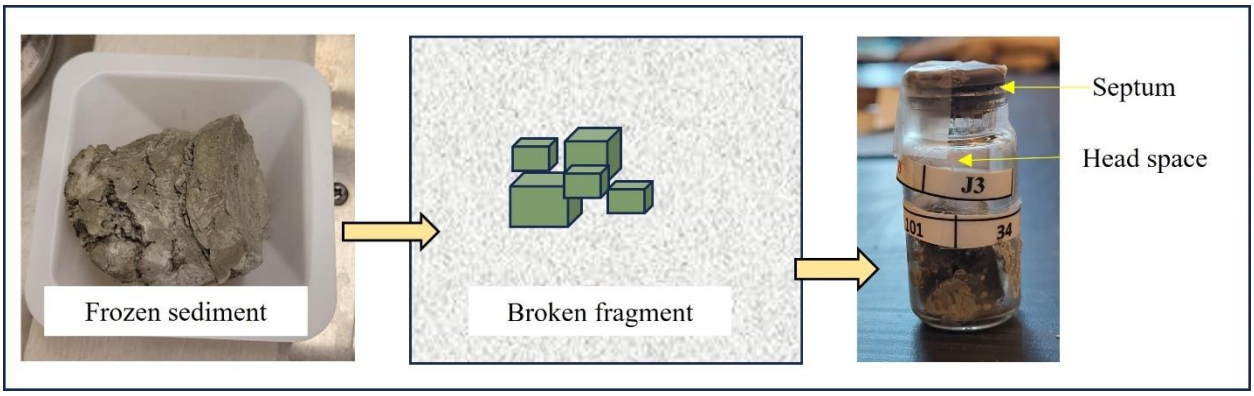

Figure 2.4. Schematic diagram showing the process of breaking a fragment from a frozen sediment core and storing it inside an airtight glass vial for gas analysis (unconfined samples).

2.4. Laboratory-based experiments

Two laboratory-based experiments were undertaken to assess methane gas leakage and storage potential in deep marine near-surface sediments. Experiment 1 evaluated the leakage rate of headspace gas stored in plastic Isojars (confined samples) over various time intervals. Experiment 2 explored the correlation between gas measured in confined samples stored in jars and that stored in the pore space of unfrozen sediment samples (unconfined samples).

2.4.1.1. Experiment 1 - Isojar leakage during long-term storage

Isojars are commonly utilized for headspace gas sampling and sediment sample storage in gas geochemical surveys. This experiment investigated gas leakage from Isojars when stored at -80 °C. Samples were selected from seep sites 2A-1 (n = 2) and 2B-1 (n = 3), known for their elevated methane concentrations compared to other sites surveyed in 2021 (Bennett & Desiage, 2022).

To estimate the gas loss, three different sampling time periods were chosen over a period of 12 months. T_0 is the initial month, T_1 represents 9 months and T_2 equals 11 months of storage (Table 2.1). We hypothesized that CH_4 would leak out of the Isojars in a systematic and predictable way.

This information could then be utilized to forecast the reliability of sample analysis from samples stored over extended durations.

2.4.1.2. Experiment 1: methods

A set of five Isojars (500 mL; Fig. 2.3) were selected for this experiment. The jars were loaded with frozen sediment and flushed with N_2 to remove air contamination (Table 2.1) before sealing. The frozen sediments in the Isojars capped with butyl septa (self healing black butyl stopper) were then thawed at room temperature (Fig. 2.3A) and sonicated to release the trapped pore gas into the headspace (T_0) (Lalk, 2023; Oremland et al., 1987). Methane concentrations were then measured (marking sampling time; T_0) using a GC-FID and ~100 µL gas volume injections. The jar was then flushed with N_2 and returned to the -80 ℃ freezer where it was stored for 9 months (T_1) until another round of gas measurements were taken (Table 2.1). The same procedure was repeated again after 11 months (T_2).

Table 2.1. Experimental design describing the different stages of sample processing leading to T_0, T_1 and T_2 samples.

Steps	**Procedure**				**Time**
Step1	Empty isojar flushed with N_2	Loading samples	Sealing the jar after flushing	Thawing samples at room temp.	-
Step 2	GC analysis	100 µL injection	Methane value recorded	Storage of isojar in -80 ℃ freezer	T_0
Step 3	After 9 months	100 µL injection	Methane value recorded	Storage of isojar in -80 ℃ freezer	T_1
Step 4	After 11 months	100 µL injection	Methane value recorded	Storage of isojar in -80 ℃ freezer	T_2

2.4.1.3. Experiment 1: results

Changes in methane concentration are reported in ppm and presented in Table 2.2. Samples ISO-J1 and ISO-J2 from site 2A-1, core 78 (02–08 cmbsf) have the lowest (17.0–17.9 ppm) initial (T_0)

gas concentrations. ISO-J2, ISO-J3, and ISO-J4 from site 2B-1, core 38 (10–20 cmbsf) have the highest methane concentrations (479.6–373.5 ppm). The leakage test shows an average of 75.5 % of the gas escaped from the Isojar headspace in 9 months (Fig. 2.5) of storage time (T_0–T_1) and an average of an additional 16.5 % in the following 2 months (T_1–T_2). Sample ISO-J3 recorded a disproportionately large methane shift with 99.3 % of the gas being lost (Fig. 2.5). From the data, the average loss of gas was calculated to be 8.4 % per month for the first 9 months (T_0–T_1) and 1.6 % per month for the subsequent two months (T_1–T_2) (Fig. 2.5).

2.4.1.4. Experiment 1: discussion and conclusions

The long-term storage leak test conducted with Isojars revealed non-uniform gas loss among samples, with those containing higher methane concentrations exhibiting faster leakage rates. From T_0 to T_1, when gas concentration was highest, the average rate of gas loss was 8.4% per month, decreasing to 1.6% per month from T_1 to T_2 (Table 2.2, Fig. 2.5). This change in leakage rate likely resulted from variations in internal headspace pressure and container sealing integrity. Sample ISO-J3 deviated from this trend, experiencing a significant gas loss of 99.3% from T_0 to T_1, likely due to a defective jar and poor seal. Analysis of leakage data from T_0 to T_1 and T_1 to T_2 (Fig. 2.5) clearly demonstrates that Isojars are most suitable for short-term gas storage (2–3 months, maximum ~9 months) and exhibit nonlinear leakage patterns. These results highlight the necessity for an improved preservation methodology when measuring headspace gas where sample storage is required.

Table 2.2. Methane concentration measured for Experiment 1 Isojar samples.

Name	Seep site	Core	Frozen sediment core	Depth	Sampling date	Methane (ppm)	Gas loss (%)
			T_0 (time = 0 days)				
ISO-J1	2A-1	78	2A-1,78	2-4	12-Mar-22	17.0	-
ISO-J2	2A-1	78	2A-1,78	6-8	12-Mar-22	17.9	-
ISO-J3	2B-1	38	2B-1,78	0-2	13-Mar-22	479.6	-
ISO-J4	2B-1	38	2B-1,38	10-12	13-Mar-22	396.9	-
ISO-J5	2B-1	38	2B-1,38	18-20	13-Mar-22	373.5	-
			T_1 (time = 9 months)				
ISO-J1	2A-1	78	2A-1,78	2-4	18-Jan-23	4.5	73.6
ISO-J2	2A-1	78	2A-1,78	6-8	19-Jan-23	4.1	77.3
ISO-J3	2B-1	38	2A-1,78	0-2	19-Jan-23	3.6	99.3
ISO-J4	2B-1	38	2A-1,38	10-12	19-Jan-23	159.0	59.9
ISO-J5	2B-1	38	2A-1,38	18-20	19-Jan-23	121.7	67.4
						Avg.	75.5
						Std Dev.	14.8
						T_0 to T_1 per month gas loss	8.4
			T_2 (time = 11 months)				
ISO-J1	2A-1	78	2A-1,78	2-4	02-May-23	4.8	0.1
ISO-J2	2A-1	78	2A-1,78	6-8	02-May-23	3.3	18.2
ISO-J3	2B-1	38	2A-1,78	0-2	02-May-23	2.2	37.7
ISO-J4	2B-1	38	2A-1,38	10-12	02-May-23	127.8	19.6
ISO-J5	2B-1	38	2A-1,38	18-20	03-May-23	113.4	6.9
						Avg.	16.5
						Std Dev.	14.4
						T_1 to T_2 per month gas loss	1.6

*The table describes the samples used for this study, their seep site names, and the depths. The loss of gas over three phases (0, 9, 11 months) are shown in percentage. An average of 75.5% of the gas escapes from the Isojar within 9 months of storage. Three-time interval of 0, 9, 11 months are recorded and named T_0, T_1 and T_2 respectively.

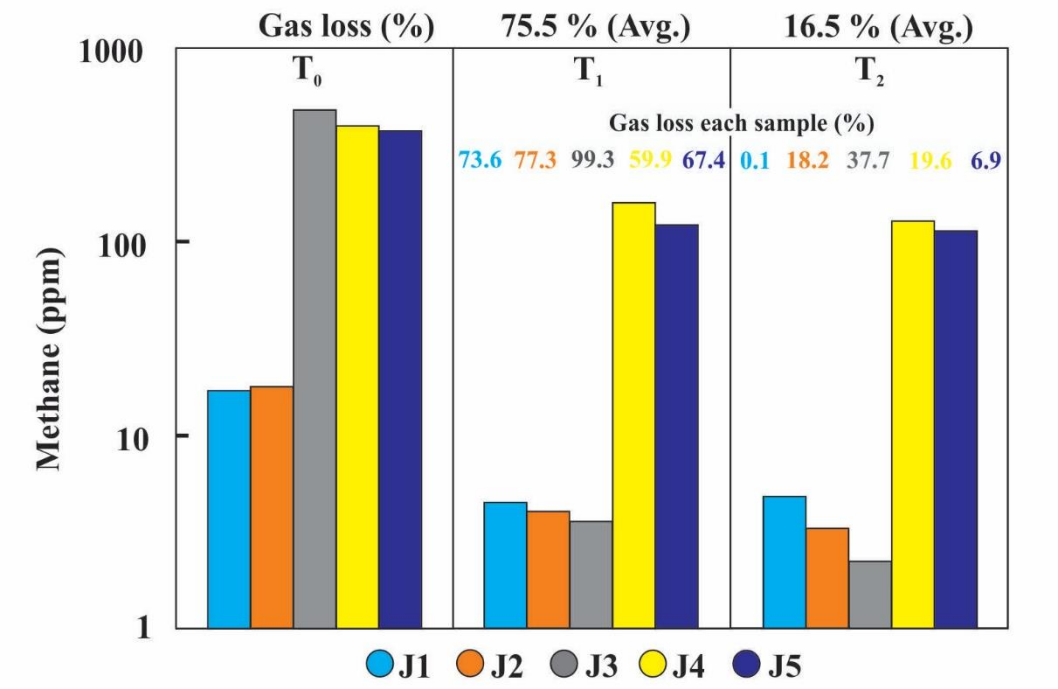

Figure 2.5. Bar graph showing gas leakage from Isojars at three different time intervals (T_0 - 0 months, T_1 - 9 months, and T_2 - 11 months).

2.4.2.1. Experiment 2: methane retention for confined and unconfined sediment samples

The findings from Experiment 1 highlight the necessity for alternative sampling methods and improved gas preservation techniques to establish a more leak-resistant system for long-term storage of gas samples. To address these challenges, the following adjustments were made: *i*) the size of the sample vials was changed from 500 mL to 25 mL, *ii*) glass vials were used, *iii*) self-healing butyl rubber stoppers were used (ID-27232, ®MilliporeSigma, USA) and *iv*) aluminium caps were added to enhance the sealing (Fig. 2.3B). The adapted methodology from Experiment 2 was utilized to investigate methane loss, which refers to the methane concentration retained in the sediment pore space per gram of sediment weight in unconfined samples.

2.4.2.2. Experiment 2: methods

Two sets of samples that were collected during 2021 cruise, from the two active seep sites were used for this experiment (Fig. 2.2A). Sample set 1 (confined), taken immediately after core recovery (T_0) and stored in a 25 mL serum glass vial capped with a butyl septum (confined, Fig. 2.3B). Sample set 2 (unconfined), were stored for 365 days (T_1) in aluminum foil, then placed in a Ziploc bag (see Fig. 2.4). Both the samples were stored at -80 ℃ freezer for one year. Seven samples from seep sites 2A-1 (n = 4) and 2B-1 (n = 3) were selected for this study based on their high methane concentrations during T_0 analysis (Fig. 2.4). The details of the samples and their sites are listed in Table 2.3. Both the T_0 and T_1 samples originate from identical seep sites, are prepared in a similar manner, and extracted from cores of comparable depth.

The time difference between T_0 and T_1 analysis was 365 days. Methane concentration per gram of sediment weight was used for the comparative study to eliminate errors arising from contrasting mass differences between two similar samples. It was expected that the pore space of unconfined frozen sediments would retain a fraction of the original trapped gas. The goal of the experiment was to analyse if the gas concentrations at T_0 and T_1 showed any qualitative or quantitative correlation.

2.4.2.3. Experiment 2: results

Table 2.3 gives the collected data and Figure 2.6 shows the loss of gas from T_0 to T_1. Figure 2.7 shows the correlation between the measured concentrations for each seep site. The part of Table 2.3 highlighted in green are samples from site 2A, and those highlighted in purple are the samples collected from site 2B. Tables 2.3 and Figure 2.7 illustrate the methane concentration per unit gram of samples taken at comparable depths. Key observations from the analysis include:

a) Sample J3, J4, J7, J9 and J10 have greater than 100 ppm of headspace methane at T_0 and gas lost at T_1 80-90 % of T_0 (Fig. 2.6, Table 2.3).

b) Methane concentration of the samples from site 2A-1 (n = 4) exhibit a high correlation (R^2 = 0.98) between in unconfined (T_1) and confined (T_0) conditions, whereas samples from site 2B (n = 3) display a lower correlation (R^2 = 0.40).

c) There is no discernible trend in methane concentration with depth for samples collected from both site 2A (n = 4) and 2B (n = 3).

2.4.2.4. Experiment 2: discussion and conclusions

The gas retained by samples at T_1 are gas bubbles trapped in the sediment pore space of the sample. The samples with high initial methane concentration at T_0 degas faster due to limited sorption capacity of the sediment pore space (Table 2.3). The contrasting correlation between samples from 2A-1 (n = 4) and 2B-1 (n = 3) arises due to the spatial location of the sampling sites, from the seep sites and from bioturbation. The samples from 2A-1 (n = 4) were collected following a spatial grid pattern and had the least bioturbation (Bennett, & Desiage, 2022), whereas 2B-1 sample locations were not equidistant spatially and showed bioturbation (Bennett, & Desiage, 2022). Unequal spatial distance can cause variation in sediment property (change in sediment texture, grain size) inducing heterogeneity in methane concentration (Berberich et al., 2020). Bioturbation often mixes geochemical or redox gradients and introduces oxygen into anoxic sediments, leading to heterogenous methane concentrations. However, the extent of bioturbation's impact on methane is not quantified (Bertics & Ziebis, 2009; Kristensen et al., 2012). The samples reached a maximum depth of 40 cm and lay within the zone of unconsolidated sediments, which show a lack of layering structure. The impact of bioturbation also plays a key role in this zone (Bennett and Desiage, 2022).

Inclusion of a depth parameter for the push core (max. 40 cm) is not sufficient to show a change in porosity vis a vis gas concentration. However, gravity or piston cores of more than 200 cm depth would be ideal samples for studying gas concentration variation with depth as they fall well below the bioturbation zone (Henderson et al., 1999).

The findings of Experiment 2 indicate that methane gas retained within the pore space of small frozen sediment slabs (CH_4 concentration at T_1) demonstrate correlation with its original value (CH_4 concentration at T_0) under specific circumstances, as elaborated below. The headspace gas collected at times T_0 and T_1 are comparable if *i*) samples are collected from a zone having minimal bioturbation, and *ii*) the sediment gas is measured within a period of 365 days. Samples with lower gas concentration at T_0 e.g. J5 (0.57 ppm for 12.72 g sediment weight and 25 mL vial volume; table 2.3, Fig. 2.7) can yield quantifiable results but the T_1 (after 365 days) values approaches to near zero (Fig. 2.7). Other factors, like sediment characteristics (porosity), may induce in situ error during sampling and storage. Furthermore, the concentration of methane per unit weight of sediment provides a better means of comparison than methane per unit depth for samples taken from closer to the subsurface (~ 40 cm).

Table 2.3. Methane concentration (ppm and µliter) for two sets of samples from 2A and 2B sites at times T_1 and T_0. T_1 was analysed 365 days after T_0 for this study. The size of the vials is the same (25 mL) to reduce error.

Name	Seep site	Core	Sampling location name	Sed. Wt. (g)	Push core depth (cmbsf)	Sampled depth (cmbsf)*	Methane Conc. (mol/100 uL injection vol.)	Methane (ppm)	Methane (ppm/g)
Headspace gas (25 mL vial); time = T_0									
J1	2A-1	27	Holey ground	12.97	22	21	4.75E-03	26.15	2.0
J3	2A-1	101	Holey ground	12.2	42	34	2.25E-02	123.64	10.1
J4	2A-2	63	Purple Haze	10.56	32	36	3.82E-02	210.18	19.9
J5	2A-5	5	NW-875m	12.72	40	40	1.03E-04	0.57	0.0
J7	2B-1	53	Clamshell	12.18	40	32	2.97E-02	163.42	13.4
J9	2B-1	46	Tiny bubble	10.66	14	10.5	3.83E-02	210.71	19.8
J10	2B-1	46	Tiny bubble	10.93	14	3.5	1.97E-02	108.61	9.9
Frozen sediment (25 mL vial); time = T_1 (365 days) **									
J1	2A-1	18	Holey ground	2.23	24	22	1.16E-09	6.38	2.9
J3	2A-1	18	Crusty white clams	3.18	24	19	2.02E-09	11.11	3.5
J4	2A-2	44	Purple Haze	2.7	38	26	2.00E-09	11.02	4.1
J5	2A-5	66	NW-525m	3.38	40	38	1.48E-11	0.08	0.0
J7	2B-1	11	Clam Shell	1.97	30	27	5.72E-10	3.14	1.6
J9	2B-1	38	Tiny bubbles	3.65	25	23.5	3.32E-10	1.83	0.5
J10	2B-1	38	Tiny bubbles	1.15	25	17	2.07E-10	1.14	1.0

* Sampled sediment were 2 cm-thick sections extracted from the push core liners.
** Sample were frozen and stored in -80 °C in unconfined form.

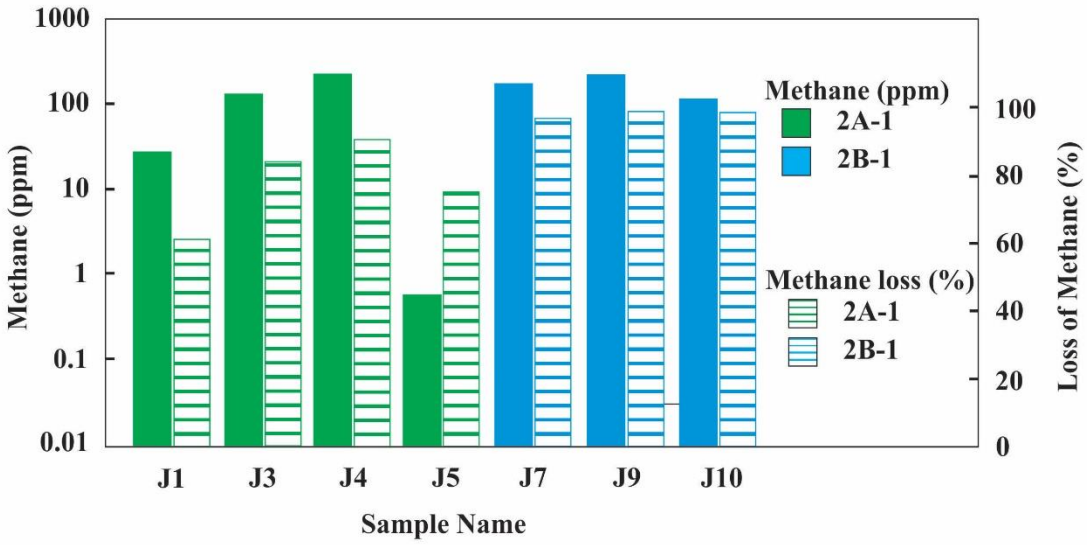

Figure 2.6. A) Plot showing the loss of gas from time T_0 to T_1. The green bars are samples from site 2A-1, and the blue are samples from site 2B-1. The solid bars display methane (ppm) at T_0. Striped bars mark the loss of gas in the stored frozen sediment biscuit from T_0 to T_1. The left side of the Y axis marks methane concentration while the right side marks the percentage of methane lost from T_0 to T_1.

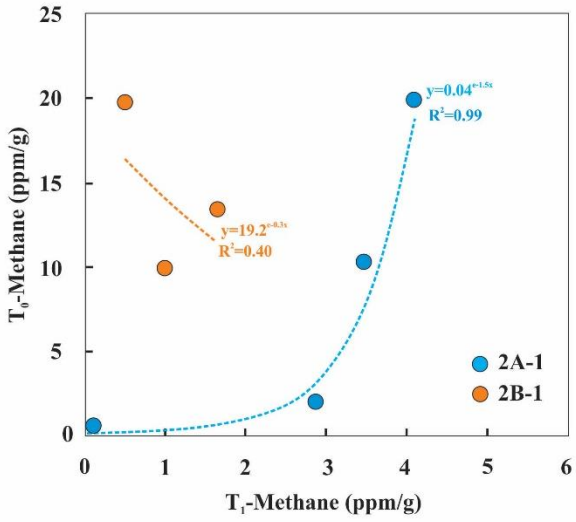

Figure 2.7. Cross-plot showing the correlation between the seven sample sets at time T_1 (unconfined, 365 days) and T_0 (confined, blue and orange circles are samples from site 2A-1 and 2B-1, respectively). Samples represented by T_1 are preserved in unconfined state at -80 ℃ refrigerator.

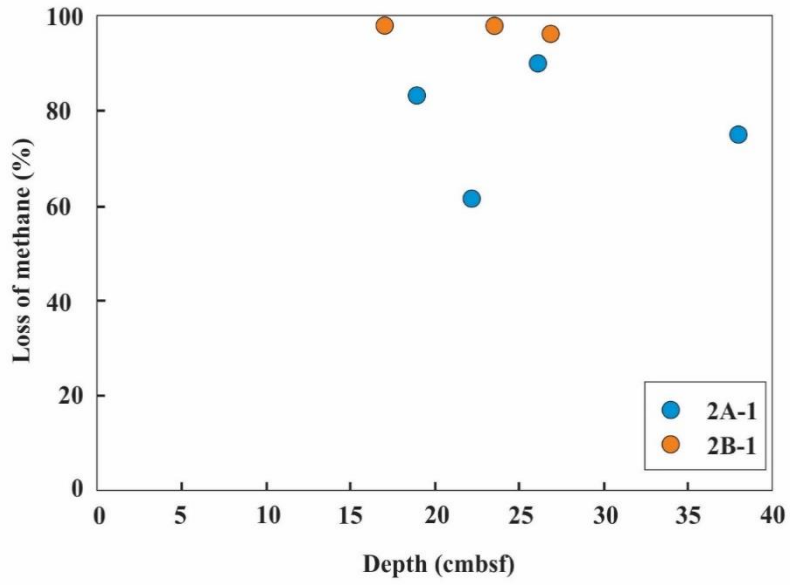

Figure 2.8. Cross-plot showing methane concentration and lack of correlation between T_1 (confined) and T_0 (unconfined) sample sets vs depth (blue and orange circles are samples from site 2A-1 and 2B-1, respectively).

2.5. Field-based experiments

2.5.1.1. Experiment 3: field verification of methane loss

This experiment involved a comparative study of methane concentrations for unconfined and confined sediment samples stored for more than 2 years in frozen condition (-80 °C), utilizing the samples collected during the 2015 and 2016 cruises. Based upon the results of Experiment 2, it was clear that sediment gas at T_1 can retain a comparable methane in pore space if the corresponding T_0 headspace gas samples had enough methane concentrations and least bioturbation (Table 2.3). This study built upon the results of Experiment 2 (see: section 2.4.2.1. Experiment 2) and was intended to verify if the retained methane (in pore space) after gas loss could be used to make a downcore profile (when $T_1 > 2$ years) for unconfined piston core samples stored over two years.

2.5.1.2. Experiment 3: methods

Methane potentially stored in the pore space of unconfined frozen cores collected during the 2015, 2016 and 2018 cruises formed the T_1 sample set for this experiment (experiment 3) were examined for this study. The T_1 samples were analysis using gas chromatograph equipped with a flame ionization detector (GC-FID), in the Department of Geology at Saint Mary's University. Applied Petroleum Technology Ltd. (APT) collected and analysed the T_0 samples for the present study and conducted the analysis on board. The frozen core sediment samples were stored for >2 years. The study involved gas analysis of 14 cores (n = 82) that included 2 cores (n = 7) from 2015, 4 cores (n = 19) from 2016 and 8 cores (n = 56) from the 2018 cruise. The selection of the 14 cores (n = 82) from the 2015 to 2018 cruises was based on a published report of higher hydrocarbon gas concentration (Fowler et al., 2018; Fowler et al., 2016).

2.5.1.3. Experiment 3: result

Figure 2.9 provides methane concentrations of each core taken during the 2015, 2016, and 2018 cruises as analysed by Applied Petroleum Technology (APT) (representing a comparative T_0 value in x-axis) with that of long-term stored samples that had largely degassed (T_1 of ≥ two-years storage, y-axis). The solid circles in Figure 2.9 represent the average methane data (Fowler and Webb, 2015; Fowler and Webb, 2016; Fowler and Webb, 2018; Fowler et al., 2018) of a core.

The results show (Fig. 2.9) the stored samples from the 2018 cruise (Fig. 2.9, blue solid circles) have degassed completely. Total six cores (Fig. 2.9, solid orange circles) of which two cores from 2015 survey (2 cores, S09 and S06) and 4 cores from 2016 survey (S49, S21, S33, S01) showed a trend (Fig. 2.9). Table 2.4 presents the gas analysis results, while Figure 2.10 illustrates the down-core methane profile for six cores.

The methane core profiles (Table 2.4; Fig. 2.10) of six cores show that two cores (S49, S21) that had high methane concentration at T_0 (>10,000 ppm) and show spike in methane concentration at depths between 2.5 to 3.5 m (Fig. 2.10).

2.5.1.4. Experiment 3: conclusions

The 2 cores from the 2016 cruise S49 (n = 9) and S21 (n = 6) retain enough gas to construct a methane profile (Table 2.4; Fig. 2.9). From the Isojar leak test (Experiment 1) it was clear that samples with low gas concentration will lose most of their methane within a year. However, unconfined frozen core samples with methane concentrations greater than 10,000 ppm (Table 2.4; Fig. 2.9) can retain sufficient methane after 2 years of storage, to enable a core profile to be constructed. Although, core S09 from the 2015 survey sample list displays a spike in methane concentration (Fig. 2.10) at a depth of 3 to 4 m, the gas concentrations of this sample are much lower (< 0.001 ppm), too low for the determination of recognisable biogeochemical zone.

The cores 2016-S49 and S2016-21 qualified for Experiment 4 and were used for further investigation, to test whether these core profiles could be used to identify recognisable shallow biogeochemical zones.

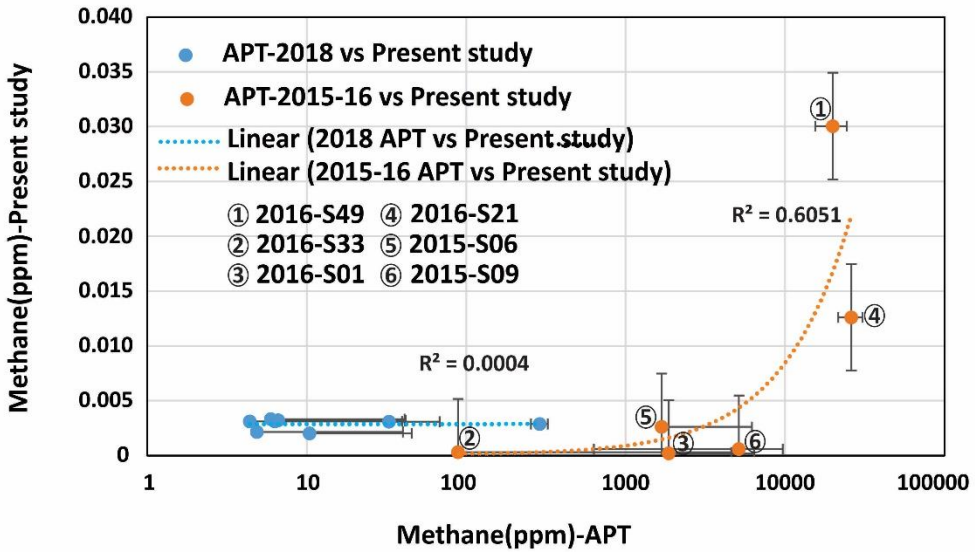

Figure 2.9. Cross-plot comparing methane concentration values from the present study and from similar confined samples analyzed by Applied Petroleum Technology (APT) survey. The unconfined sample sets were collected during the 2015, 2016 and 2018 cruises. Only six cores (hollow circle numbered 1-6) show a correlation (orange trend line) and two cores S49 (4) and S21 (1) from the 2016 cruise had more than 10^4 ppm of methane and could be used to find the SMTZ.

Table 2.4. Methane analysis from unconfined samples collected during the 2016 and 2015 cruises.

Name	Site	Core	Sample type	Push core depth (mbsf)	Depth Avg. (m)	Sample preserved time (Year)	Methane (ppm)
2016-cruise (4 cores, n=21)							
S49-1	S49	49	frozen core	0.82	0.80	2	0.0032
S49-2	S49	49	frozen core	1.49	1.47	2	0.0402
S49-3	S49	49	frozen core	2.31	2.29	2	0.4565
S49-4	S49	49	frozen core	2.89	2.87	2	0.0007
S49-5	S49	49	frozen core	3.67	3.65	2	0.0084
S49-6	S49	49	frozen core	4.09	4.06	2	0.0857
S49-7	S49	49	frozen core	4.48	4.46	2	0.0688
S49-8	S49	49	frozen core	4.65	4.63	2	0.1268
S49-9	S49	49	frozen core	6.25	6.23	2	0.0797
S21-1	S21	21	frozen core	0.17	0.15	2	0.0100
S21-2	S21	21	frozen core	1.55	1.51	2	0.0108
S21-3	S21	21	frozen core	2.15	2.13	2	0.0099
S21-4	S21	21	frozen core	2.36	2.33	2	0.0276
S21-5	S21	21	frozen core	2.41	2.39	2	0.0926
S21-6	S21	21	frozen core	2.55	2.53	2	0.0108

S33-1	S33	33	frozen core	1.75	1.73	2	0.0003
S33-2	S33	33	frozen core	3.25	3.23	2	0.0003
S33-3	S33	33	frozen core	6.15	6.13	2	0.0003
S1-1	S1	1	frozen core	2.70	2.68	2	0.0002
S1-2	S1	1	frozen core	4.60	4.58	2	0.0003
S1-3	S1	1	frozen core	6.36	6.34	2	0.0002
2015-cruise (2 cores, n=8)							
S9-1	S9	9	frozen core	1.49	1.47	3	0.0003
S9-2	S9	9	frozen core	3.02	3.00	3	0.0003
S9-3	S9	9	frozen core	3.69	3.66	3	0.0021
S9-4	S9	9	frozen core	4.38	4.36	3	0.0004
S6-1	S6	6	frozen core	2.26	2.23	3	0.0004
S6-2	S6	6	frozen core	3.33	3.30	3	0.0014
S6-3	S6	6	frozen core	3.65	3.63	3	0.0035
S6-4	S6	6	frozen core	5.05	5.03	3	0.0259

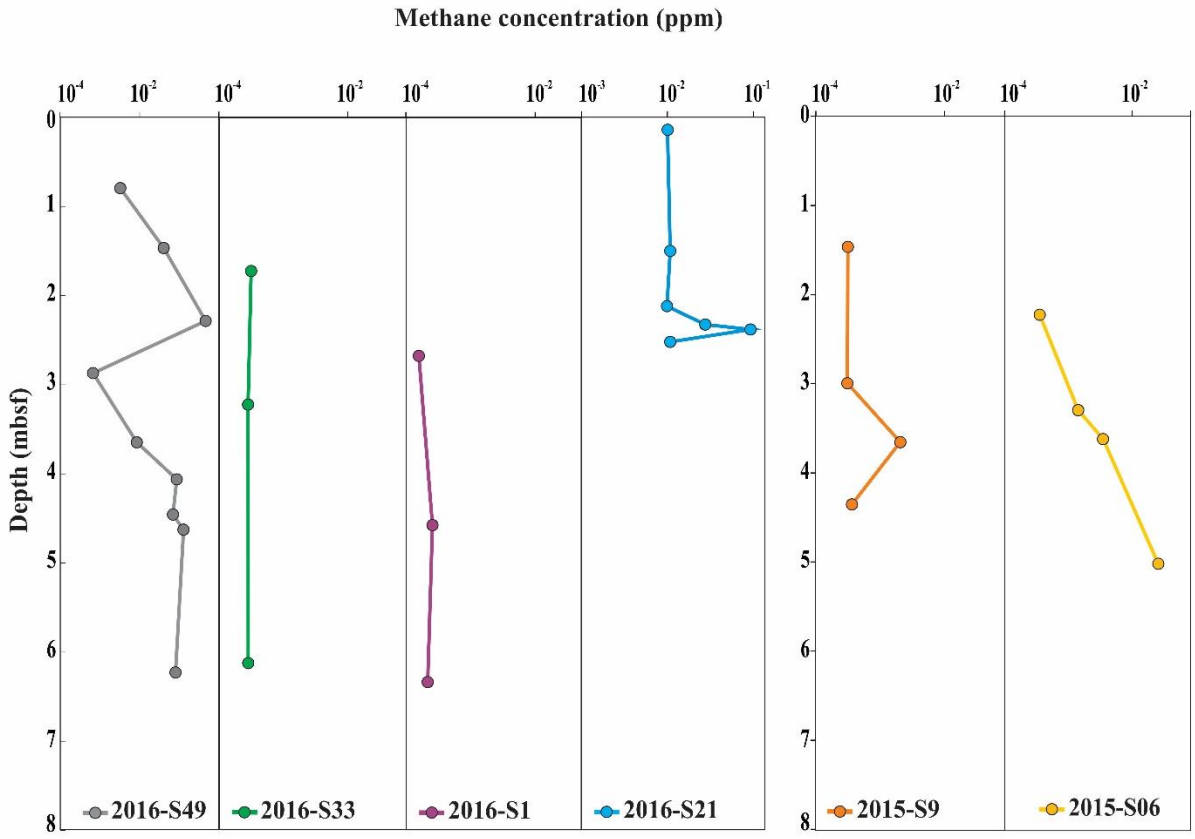

Figure 2.10. Methane core profiles of unconfined frozen sediment samples from the 2016 survey (4 cores (S49, S33, S21, S01), n = 21) and 2015 survey (2 cores (S09, S06), n = 8) cruises, collected from the Scotian Slope. Each core has 3-9 sample points (solid circle) at different depth, the total sample point from one survey is indicated by n value.

2.5.2.1. Experiment 4: identifying shallow biogeochemical zones at the Scotia Slope

Methane builds up below the sulfate zone (Mogollón et al., 2012; Mogollón et al., 2013), often reaching concentrations that surpass the in situ hydrostatic pressure, resulting in the formation of free gas bubbles trapped within the soft sediment. Porewater geochemistry provides insights into the dynamic processes occurring within the subsurface biogeochemical zone (Borowski et al., 1996). Experiment 4 seeks to find such potential biogeochemical zones in my study area. To achieve this objective, we selected the two most promising cores (S49 and S21; Fig. 2.10) from samples collected during the 2016 cruise, along with their corresponding profiles obtained from Experiment 3. The results from Experiment 3 indicated that a high initial methane gas concentration in sediment at T_1 (>10,000 ppm) was necessary for constructing a methane downcore profile. However, in Experiment 4, additional measurements of sulfate and carbonate were introduced to delineate the mechanism causing fluctuation in methane concentration.

2.5.2.2. Experiment 4: methods

Porewater sulfate (SO_4^{2-}) and carbonate (CO_3^{-}) data (Barker & Ridgwell, 2012) were collected from core sediment. To isolate the porewater within sediment cores, 30-35 mg of sediment was centrifuged in 50 mL centrifuge tubes at 2000 rpm for 10-15 minutes. This process physically separated the porewater from the sediment, after which the porewater was meticulously filtered using filter paper to eliminate any contamination (Nikita, 2022). The concentration of sulfate and carbonate was determined using a Thermo Scientific Dionex Aquion Ion Chromatography Conductivity Detector System equipped with an anion-exchange column and a DS6 Heated Conductivity Cell, which included an AERS_4mm suppressor pump and a Dionex AXP Auxiliary pump and pump ECD. To enable precise analysis of seawater samples, the Ion chromatography

system was additionally set up with an in-line Thermo Scientific 9×24 mm Dionex InGuard Ag sample prep cartridge and Thermo Scientific Dionex InGuard Na prep cartridge (Nikita, 2022).

The downcore profiles of residual methane and sediment porewater sulfate and carbonate concentrations were joined for two sediment cores (S49 and S21) from the 2016 cruise (Fig. 2.11) to determine whether the SMTZ could be located. Sulfate and carbonate data for this experiment were imported from published results (Nikita, 2022).

2.5.2.3. Experiment 4: results

Table 2.5 shows the sulfate and carbonate concentrations of the two cores of 2016 survey S49 and S21 at different depth.

The merged methane, sulfate and carbonate down core profile shows the changes in the concentration gradient at different depth (Fig. 2.11). Core S49 of 2016 (Fig. 2.11) shows a steady decrease in sulfate concentration from 0.77 m 1.44 m and core S21 of 2016 (Fig. 2.11) shows a steady decrease in sulfate concentration from 0.12 m 1.48 m. The carbonate down core profile for both the cores shows a steady increase in the concentration gradient (Fig. 2.11). Methane concentration decreases sharply after 2.5 m for core 2016-S21 followed by similar trend in sulfate curve (Fig. 2.11), and methane concentration decreases gradually after 3.5 m depth for core 2016-S49 followed by similar trend in sulfate curve (Fig. 2.11).

2.5.2.4. Experiment 4: conclusions

The SMTZ refers to a relatively thin region near the seafloor where the decrease in porewater sulfate intersects with the increase in methane concentrations as a result of AOM (Borowski et al., 1999). While microbes can consume sulfate using solid organic carbon (Berner, 1980), AOM tends

to dominate sulfate depletion in sediments containing gas hydrates and experiencing moderate methane fluxes.

The methane, sulfate and carbonate down core profile (Fig. 2.11) suggest the sulfate is getting reduced for both the core till a depth of 1.48 m and the SMTZ would exist below the depth of 2.5 m for core 2016-S21, and 3.5 m for core 2016-S49 as there is a steady decrease in both sulfate and methane gradient (Fig. 2.11). However, the thickness of SMTZ cannot be determined from the available sample set.

Table 2.5. Sulfate and carbonate concentrations for samples collected on the 2016 cruise (Nikita, 2022).

Name	Site	Core	Frozen sediment core (unconfined)	Core bottom depth (mbsf)	Averaged sampling depth (mbsf)	Sample preservation time (year)	Sulfate SO_4^{-2} (ppm)	Carbonate CO_3^{-2} (ppm)
2016-cruise (2 cores, n=13)								
S49-1	S49	49	frozen core	0.82	0.77	2	845.24	202.20
S49-2	S49	49	frozen core	1.49	1.44	2	119.47	457.30
S49-3	S49	49	frozen core	2.31	2.26	2	106.55	623.21
S49-5	S49	49	frozen core	3.67	3.62	2	146.06	528.82
S49-6	S49	49	frozen core	4.09	4.03	2	49.07	496.33
S49-8	S49	49	frozen core	4.65	4.6	2	24.10	887.33
S49-9	S49	49	frozen core	6.25	6.2	2	8.19	443.04
S21-1	S21	21	frozen core	0.17	0.12	2	1607.16	201.67
S21-2	S21	21	frozen core	1.55	1.48	2	181.07	570.37
S21-3	S21	21	frozen core	2.15	2.1	2	200.59	770.50
S21-4	S21	21	frozen core	2.36	2.3	2	224.78	776.84
S21-5	S21	21	frozen core	2.41	2.5	2	237.25	1649.00
S21-6	S21	21	frozen core	2.55	2.85	2	50.60	2075.56

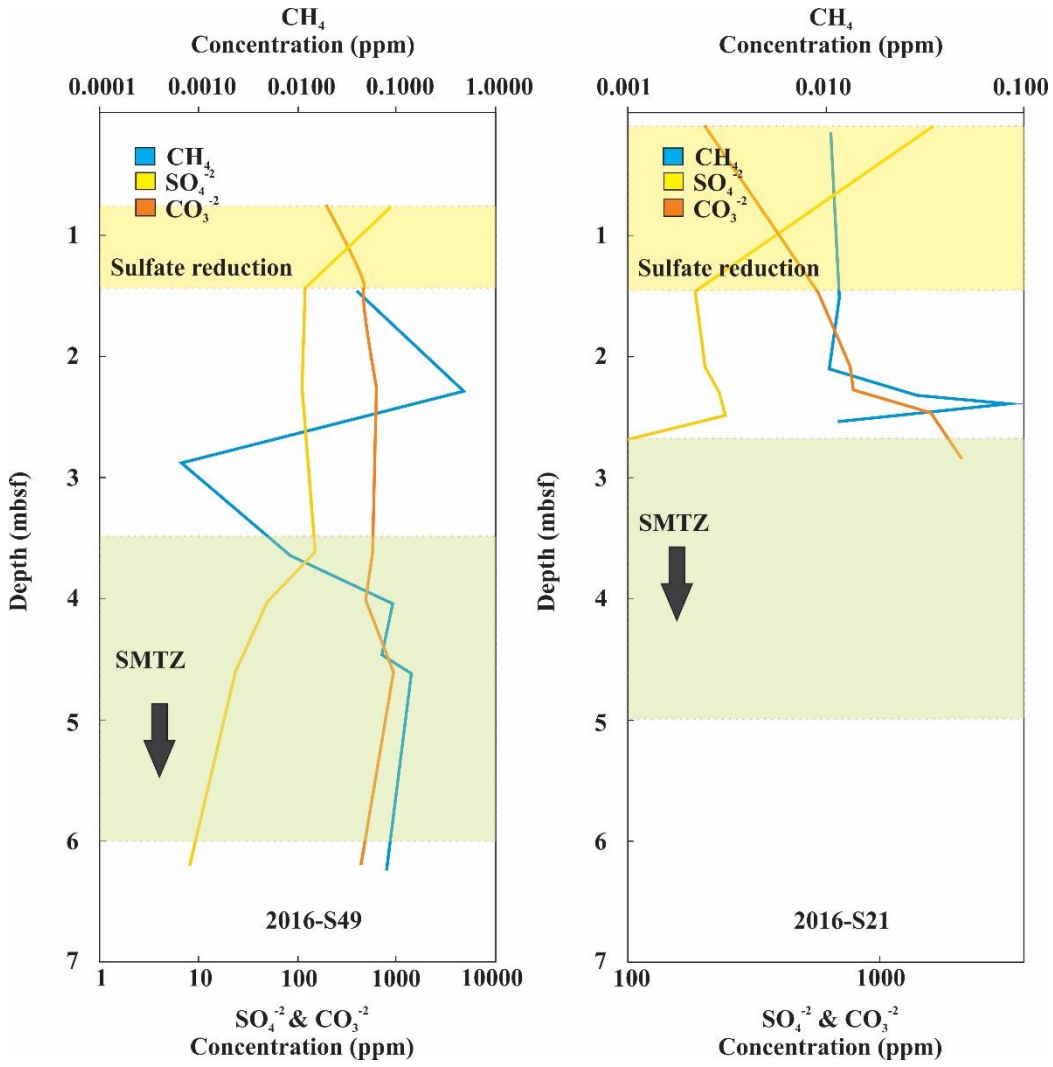

Figure 2.11. The sulfate reduction zone and tentative location of SMTZ was deduced from the methane core profiles combined with sulfate and carbonate data (Nikita, 2022) for two cores (S49, S21) collected during the 2016 cruise.

2.6. Conclusions from all experiments

Plastic Isojars are suitable only for short-term storage of gas (<2 months). On an average 75.5 % of the headspace gas is lost in the first nine months of storage. Cores stored for more than three years are likely to be totally degassed and lose any recognisable fraction of methane. A stored sediment's methane gas retention is dependent on the initial concentration of methane (T_0) and the duration of storage. Only some cores will be able to retain methane concentration that can be used

to build a downcore profile. Two cores from the 2016 cruise, S49 and S21, showed high enough methane concentrations and were able to predict the tentative depth of SMTZ below 3.5 and 2.5 mbsf for core S49 and S21 respectively and aligned with the methane downcore profile.

References

Barker, S., & Ridgwell, A. (2012). Ocean acidification. Nature Education Knowledge, 3(10), 21.

Bennett, R. & Desiage, P. (2022). Expedition report 21CONDOR: Scotian slope, august 14-29, 2021. Geological Survey of Canada.

Berberich, M. E., Beaulieu, J. J., Hamilton, T. L., Waldo, S., & Buffam, I. (2020). Spatial variability of sediment methane production and methanogen communities within a eutrophic reservoir: Importance of organic matter source and quantity. *Limnology and oceanography*, *65*(6), 1336-1358.

Bertics, V. J., & Ziebis, W. (2009). Biodiversity of benthic microbial communities in bioturbated coastal sediments is controlled by geochemical microniches. *The ISME journal*, *3*(11), 1269-1285.

Campbell, D. C. (2019). CCGS Hudson Expedition 2016-011, phase 2. Cold seep investigations on the Scotian Slope, offshore Nova Scotia, June 15–July 6, 2016. Geological Survey of Canada, Open File, 8525, 88.

Danovaro, R., Snelgrove, P. V., & Tyler, P. (2014). Challenging the paradigms of deep-sea ecology. Trends in ecology & evolution, 29(8), 465-475.

Diplas, P., & Fripp, J. B. (1992). Properties of various sediment sampling procedures. Journal of Hydraulic Engineering, 118(7), 955-970.

Dong X, Rattray JE, Campbell DC, Webb J, Chakraborty A, Adebayo O, Matthews S, Li C, Fowler M, Morrison NM, MacDonald A. (2020). Thermogenic hydrocarbon biodegradation by diverse depth-stratified microbial populations at a Scotian Basin cold seep. Nature communications, 11(1), 5825.

Fowler, M. and Webb, J. (2015) Geochemistry Data Report for 2015 Scotian Slope Piston Coring Program http://documents.oera.ca/files

Fowler, M. and Webb, J. (2016) Geochemistry Data Report for 2016 Scotian Slope Piston Coring Program.

Fowler, M. and Webb, J. (2018) Geochemistry Data Report for 2018 Scotian Slope Piston Coring Program.

Fowler, M., Webb, J., Hubert, C., Li, C. and Macdonald, A. (2018) Implications for Petroleum Systems in the Deep-Water Scotian Slope, Offshore Nova Scotia based on Geochemical and Microbiological Analyses of Piston Core Samples. Geoconvention 2018, Calgary May 2018.

Fowler, M., Webb, J., Hubert, C., Li, C., & Macdonald, A. (2018). Implications for Petroleum Systems on the deep waterdeep-water Scotian Slope, offshore Nova Scotia based on geochemical and microbiological analyses of piston core samples. Geoconvention2018, Vol. 55, 1-3.

Gresov, A. I., Shakhova, N. E., Sergiyenko, V. I., Yatsuk, A. V., & Semiletov, I. P. (2016). Isotope and geochemical parameters of hydrocarbon gases in bottom sediments of the shelf of the East Siberian Sea. In Doklady Earth Sciences (Vol. 469, pp. 864-866).

Henderson, G. M., Lindsay, F. N., & Slowey, N. C. (1999). Variation in bioturbation with water depth on marine slopes: a study on the Little Bahamas Bank. Marine Geology, 160(1-2), 105-118.

Hong, W. L., Torres, M. E., Kim, J. H., Choi, J., & Bahk, J. J. (2013). Carbon cycling within the sulfate-methane-transition-zone in marine sediments from the Ulleung Basin. Biogeochemistry, 115, 129-148.

Hu, C.Y., Yang, T.F., Burr, G.S., Chuang, P.C., Chen, H.W., Walia, M., Chen, N.C., Huang, Y.C., Lin, S., Wang, Y. and Chung, S.H. (2017). Biogeochemical cycles at the sulfate-methane transition zone (SMTZ) and geochemical characteristics of the pore fluids offshore southwestern Taiwan. Journal of Asian Earth Sciences, 149, 172-183.

Johnson, T. R., & Brown, S. M. (2019). Accurate sediment retrieval from the ocean floor using push corers from a remotely operated vehicle (ROV) or manned submersible. Marine Technology Journal, 12(2), 78-89.Kerr, M. J., Hanley, J. J., & Kontak, D. J. (2021). Application of bulk fluid volatile chemistry to exploration for metasedimentary rock-hosted orogenic gold deposits: An example from the Meguma terrane, Nova Scotia, Canada. Journal of Geochemical Exploration, 226, 106764.

Kerr, M., Hanley, J., Morrison, G., Everest, J., & Bray, C. (2015). Preliminary evaluation of trace hydrocarbon speciation and abundance as an exploration tool for footwall-style sulfide ores associated with the Sudbury Igneous Complex, Ontario, Canada. Economic Geology, 110(2), 531-556.

Klasek, S.A., Hong, W.L., Torres, M.E., Ross, S., Hostetler, K., Portnov, A., Gründger, F. and Colwell, F.S. (2021). Distinct methane-dependent biogeochemical states in Arctic seafloor gas hydrate mounds. Nature communications, 12(1), 6296.

Kristensen, E., Penha-Lopes, G., Delefosse, M., Valdemarsen, T., Quintana, C. O., & Banta, G. T. (2012). What is bioturbation? The need for a precise definition for fauna in aquatic sciences. Marine ecology progress series, 446, 285-302.

Kvenvolden, K. A., & Lorenson, T. D. (2000). Methane and other hydrocarbon gases in sediment from the southeastern North American continental margin. In Proceedings of the Ocean Drilling Program, Scientific Results (Vol. 164, pp. 29-36). College Station Texas.

Lalk, E. (2023). The Biogeochemistry of Methane Isotopologues in Marine and Lacustrine Sediments. Massachusetts Institute of Technology. Chapter 4, pp. 138.

LSASD_Report, (2023). United States Environmental Protection Agency. EnviroAtlas. Laboratory Services & Applied Science Division Athens, Georgia; Sediment Sampling. Retrieved: Jan,11,2024 from https://www.epa.gov/sites/default/files/2015-06/documents/Sediment-Sampling.pdf.

Miller, A. B., & Thompson, R. L. (2021). Gas geochemical analyses: Optimal timing for onboard research vessel performance. Oceanographic Research Quarterly, 18(3), 56-68.

Mogollón, J. M., Dale, A. W., Fossing, H., & Regnier, P. (2012). Timescales for the development of methanogenesis and free gas layers in recently-deposited sediments of Arkona Basin (Baltic Sea). Biogeosciences, 9(5), 1915-1933.

Mogollón, J. M., Dale, A. W., Jensen, J. B., Schlüter, M., & Regnier, P. (2013). A method for the calculation of anaerobic oxidation of methane rates across regional scales: an example from the Belt Seas and The Sound (North Sea–Baltic Sea transition). Geo-marine letters, 33, 299-310.

Nikita, N. (2022). Survey of porewater geochemistry within deep marine hydrocarbon seep sediments of the Scotian Slope, Canada. [Undergraduate Honours thesis, Saint Mary's University]. http://library2.smu.ca/xmlui/handle/01/30976

NMEP_Report. Seafloor Sampling (11 Jan, 2024). The National Marine Equipment Pool (NMEP) is the largest centralised marine scientific equipment pool in Europe. https://noc.ac.uk/facilities/national-marine-equipment-pool/scientific-engineering/seafloor-sampling.

Oremland, R. S., Miller, L. G., & Whiticar, M. J. (1987). Sources and flux of natural gases from Mono Lake, California. Geochimica et Cosmochimica Acta, 51(11), 2915-2929.

Owino, Y. D. (2023). Integrative ArcGIS mapping study of direct hydrocarbon indicators within the Shelburne Subbasin of the Scotian Slope, Nova Scotia.

Peoples LM, Grammatopoulou E, Pombrol M, Xu X, Osuntokun O, Blanton J, Allen EE, Nunnally CC, Drazen JC, Mayor DJ and Bartlett DH (2019) Microbial Community Diversity Within Sediments from Two Geographically Separated Hadal Trenches. Frontiers in microbiology, 10, 347.

Smith, J. K., & Johnson, L. M. (2020). Synergy between deep sea sediment cores and gas geochemistry: Advancements in Earth's history, climate research, and sustainable resource management. Journal of Oceanographic Science, 15(3), 102-117.

Tipler, A. (2013). An introduction to headspace sampling in gas chromatography fundamentals and theory. Perkinelmer report, 1-35.

Torres, M.E., McManus, J., Hammond, D.E., De Angelis, M.A., Heeschen, K.U., Colbert, S.L., Tryon, M.D., Brown, K.M. and Suess, E. (2002). Fluid and chemical fluxes in and out of sediments hosting methane hydrate deposits on Hydrate Ridge, OR, I: Hydrological provinces. Earth and Planetary Science Letters, 201(3-4), pp.525-540.

US EPA. (2001). Methods for collection, storage and manipulation of sediments for chemical and toxicological analyses: Technical manual. EPA 823-B-01-002. US.

Voskuil, T. (1991). Handbook: Remediation of contaminated sediments (No. PB-93-116275/XAB; EPA-625/6-91/028). Environmental Protection Agency, Washington, DC (United States). Office of Research and Development.

Weisman, W. (Ed.). (1998). Analysis of petroleum hydrocarbons in environmental media (Vol. 1). Amherst Scientific Publishers.

Zhuang, G. C., Xu, L., Liang, Q., Fan, X., Xia, Z., Joye, S. B., & Wang, F. (2019). Biogeochemistry, microbial activity, and diversity in surface and subsurface deep-sea sediments of South China Sea. Limnology and Oceanography, 64(5), 2252-2270.

Chapter 3. Cold Seep Formation from Salt Diapir–Controlled Deep Biosphere Oases

Authors: Chowdhury, A.[1], Ventura, G.T.[1], Owino, Y.[1], Lalk, E.[2], MacAdams, N.[3], Dooma, J.[1], Ono, S.[2], MacDonald, A.[3], Fowler, M.[4], Bennett, R.[5], MacRae, R.A.[1], Hubert, C.[6], Bentley, J.[1], Kerr, M. J.[1]

Author Affiliations:

1. Department of Geology, Saint Mary's University, 923 Robie Street, Halifax, Nova Scotia B3H 3C3, Canada

2. Department of Earth, Atmospheric, and Planetary Sciences, Massachusetts Institute of Technology, Cambridge MA 02139, USA

3. Nova Scotia Department of Natural Resources and Renewables, 1690 Hollis St., Halifax, Nova Scotia B3J 3J9, Canada

4. Applied Petroleum Technology Ltd., 5227 Carney Road NW, Calgary, AB T2L 1G1, Canada

5. Natural Resources Canada, Dartmouth, NS B2Y 4A2, Canada

6. Energy Bioengineering and Geomicrobiology Group, 2500 University Dr NW, University of Calgary, Calgary, Alberta T2N 1N4, Canada

Citation: Chowdhury A, Ventura GT, Owino Y, Lalk EJ, MacAdam N, Dooma JM, Ono S, Fowler M, MacDonald A, Bennett R, MacRae RA, Hubert CRJ, Bentley JN, Kerr MJ. (2024). Cold seep formation from salt diapir–controlled deep biosphere oases. Proceedings of the National Academy of Sciences, 121(12), e2316878121.

The paper has been blended (the margin, position of the figures) to create a chapter within the thesis

Abstract

Deep sea cold seeps are sites where hydrogen sulfide, methane, and other hydrocarbon-rich fluids vent from the ocean floor. They are an important component of Earth's carbon cycle in which subsurface hydrocarbons form the energy source for diverse benthic micro and macro fauna in what is an otherwise vast and spartan sea scape. Passive continental margin cold seeps are typically attributed to the migration of hydrocarbons generated from deeply buried source rocks. Many of these seeps occur over faults formed by salt tectonics. The movement of salt diapirs and canopies creates complex fault systems that can enable fluid migration or create seals and traps for reservoir formation. Additionally, the elevated advective heat transport from these salt structures produces a directly overlying chimney effect. Here we provide geophysical and geochemical evidence that the salt chimney effect in conjunction with diapiric faulting drives a subsurface groundwater circulation system bringing dissolved inorganic carbon (DIC), nutrient-rich deep basinal fluids, and potentially overlying seawater onto the crests of deeply buried salt diapirs. The mobilized fluids fuel methanogenic archaea locally enhancing the deep biosphere. The elevated biogenic methane production, alongside the upward heat-driven fluid transport, represents a previously unrecognized mechanism of cold seep formation.

3.1. Introduction

Cold seeps are among the most biologically diverse ecosystems of deep ocean environments (Paull et al., 1984; Jørgensen et al., 2007; Vanreusel et al., 2009; Levin and Sibuet, 2012; Pop Ristova et al., 2015). The rich biota is sustained by a chemosynthetic fauna that primarily derives energy from the oxidation of venting hydrocarbons and reduced sulfur expelled from deeper within the sedimentary basin (Foucher et al., 2009). The dominant biogeochemical process is sulfate driven anaerobic oxidation of methane (AOM)

$$CH_4 + SO_4^{2-} \rightarrow HCO_3^- + HS^- + H_2O \quad (1)$$

that consumes a significant proportion of the methane rising to the seabed thereby marking the main hydrocarbon sink in marine sediments (Boetius, 2000; Orphan et al., 2001).

Globally, cold seeps are common features of petroleum producing basins (Joye, 2010; Suess, 2018) making them important guides to offshore exploration for oil and gas deposits (Judd and Hovland, 2007). Cold seeps are also common to deeper continental slope salt tectonic provinces of passive plate margins. Over 29 sedimentary basins around the world host extensive salt provinces (Hudec and Jackson, 2007), with many of these being among the world's great hydrocarbon producing regions (i.e., Gulf of Mexico, the Persian Gulf, and Campos Basin). The salt-tectonic-related traps in these provinces make-up an estimated 50% of the world's known total petroleum reserve (Grunau, 1987).

Salt deposition during early basin formation, coupled with the mineral's less dense and ductile nature upon sediment loading, creates a great diversity of basin stratigraphic and structural effects that makes these ideal systems for petroleum reservoir creation (Hudec and Jackson, 2007). In these settings, hydrocarbons and formation waters migrate from the adjacent strata and interact with the salt or other evaporites. The fluids then continue to migrate generally up-dip following pressure gradients along the domal structure. By deforming the surrounding strata, salt structures often produce radial, concentric, and other faults along their flanks and above their crests that act to further channelize migrating fluids (Römer et al., 2021). This leakage by the disruption of overlying sedimentary strata can produce cold seeps reaching up to 100 m wide on the ocean floor (Suess, 2014).

Seismic reflection surveys not only enable documentation of geologic basin structure they are also commonly used to find hydrocarbon-bearing reservoirs through the detection of seismic amplitude and continuity anomalies, termed direct hydrocarbon indicators (DHIs), that form in the presence of subsurface gas chimneys and other hydrocarbon fluid hosted structures. Although not all hydrocarbon occurrences produce DHIs, the technique has become a common industrial method for offshore petroleum prospecting. DHIs are globally observed above salt diapirs across many major oil producing basins (Serié et al. 2012; Liu et al., 2022; Portnov et al., 2019).

The Scotian Slope is home to a large salt tectonic system that is subdivided into diapir-dominated and canopy-dominated provinces (Albertz et al. 2010; Deptuk et al., 2017). Here cold seeps capable of hosting a rich diversity of benthic life (Bennett and Desiage, 2012) are associated with salt diapirs along the continental slope of the Shelburne Subbasin, offshore Nova Scotia, Canada (Campbell, 2016). Recent studies indicate there is also an active and diverse microbial community that inhabits the near-surface and deeply buried sediments within and around the Scotian Slope cold seeps (Dong et al., 2020; Gittins et al., 2022; Rattray et al., 2023; Li et al., 2023). Near-surface hydrocarbon seep sediments have been shown to host microbial communities with C3 heterotrophic affinities (Dong et al., 2020). Bacterial thermophilic endospores have been shown to rise up from within a petroleum producing reservoirs deep within the basin at active cold seeps (Gittins et al., 2022; Rattray et al., 2023).

The manner in which passive margin cold seeps are formed and maintained maybe only be partially understood. Migration of thermogenic hydrocarbons or periodic gas hydrate instability and release (both ultimately resulting in autogenic carbonate production by AOM) represent known pathways. In this study, we provide evidence that, contrary to expectation, biologically diverse ocean floor cold seeps can also be an extension of methanogenic archaeal deep biosphere oases that are

supported by the interplay between salt-generated deformation and heat-driven groundwater circulation.

3.2. Results

Two wide-azimuth 3D seismic surveys (named Shelburne and Tangier), totalling an area of 18,400 km^2 spanning 500 m to >4,000 m water depth within the Scotian Slope, were mapped to a sediment basin depth of 3,000 mbsf (meters below seafloor) (Fig. S1). Here the margin is home to a complex allochthonous salt province extending across much of the slope. Vertical diapirs dominate, but other salt structures, such as salt canopies, are present in the northeastern region of the Tangier survey. For the mapped region, 99 diapirs were identified and basic parameters were measured (Fig. S2). These diapirs rise from the Late Triassic-Early Jurassic Argo Formation, initially deposited near the bottom of the basin (Figs. S3). Their emplacement has disturbed the overlying and laterally adjacent basin rock strata, creating complex polygonal, radial, and crestal faults systems as well as subsided minibasins adjacent to the salt structures (Fig. 3.1 and S1; S10–S18). Diapirs located further down the continental slope (≥ 2,500 m water depth) reach closer to the seafloor (~0–400 mbsf) than those nearer to the shelf break that are thickly covered (~1500 mbsf) (Fig. S3).

Seismic attribute root mean square (RMS) amplitude maps were generated for multiple depth intervals (300 mbsf ±100 m; 1100 mbsf ±400 m; and 1250 mbsf ±250 m) resulting in a near-continuous survey down to 1500 mbsf (Fig. 3.1; Fig S1) for both the Shelburne and Tangier 3D data blocks. Coherence maps were also generated to enhance discontinuous structural geologic features such as faults, paleochannels, salt diapirs, and intervening minibasins. Detected strong amplitude anomalies (“bright spots” in RMS amplitude maps) were interpreted to be DHIs if they are not likely lithologically controlled (such as basal fill of incised paleocanyons). These two

seismic attribute maps were overlain and interpreted using associated vertical sections to identify potential fluid-flow migration pathways from 1500 mbsf to the seafloor (Fig. 3.1). Across the geographic area, 37 DHIs were identified (Table S1). All of these are located directly above salt structures (Fig. 3.1; Figs. S10–18).

The location of the gas hydrate stability zone (GHSZ), marking the depth methane becomes trapped within clathrates, was identified in the seismic data by a pronounced bottom simulating reflector located at 0–100 mbsf. Below the GHSZ methane gas has the potential to move more freely to shallower basin zones. All of the detected DHIs in our survey are below the GHSZ, at 200–500 mbsf (Mosher, 2011), where they commonly occupy fault-bounded crestal half-grabens draped by a seal of relatively impermeable contourite muds and mass transport deposits. Most of these relatively shallow DHIs (n=22) are intersected by diapir-generated faults, some of which reach to unconsolidated sediments near the ocean floor, thereby providing potential migration pathways for deeply-sourced fluids (Fig. 3.3, Figs S10–S18). The fluids forming these DHIs appear to be vertically ascending, based on their position at local structural culminations; potentially following the structural conduits formed by the underlying diapirs along flanking anticlinal bedding planes of adjacent minibasins and the diapir-related crestal faults. Two more shallow seepage anomalies interpreted to be gas chimneys were found directly over salt diapirs in the Shelburne survey (referred to as site 48 and 49), but do not have an associated DHI. These reside along a portion of the slope interpreted to have an inadequate seal to form a trap (Fig. S2). Surprisingly, in the Shelburne and Tangier surveys virtually no verified DHIs, including major resolvable gas chimneys, exist away from salt bodies even when potential structural features for fluid transport and fluid trapping are present off axis of the diapir crest (Fig. 3.1 and 3.3, S10–S18; Table S6).

3.2.1. Ocean floor cold seeps

In 2020 an automated underwater vehicle (AUV) cruise surveyed 10 prospective seep sites in the Shelburne and Tangier area based on the presence of DHI mapping, geophysical evidence of fluid escape structures, and geochemical data generated from three prior piston and gravity coring surveys (Fowler et al., 2017; Fowler et al., 2019). The acquired multibeam benthic maps were then used to direct a 2021 remotely operated vehicle (ROV) push coring survey that targeted seven prospective seep locations (Fig. S4–S6). Only two of these sites, 2A-1 (The Hole) and 2B-1 (Clamshell); marking DHI #s 34 and 32 (Fig. 3.1A and Fig. S2) located at 2691.9 and 2740 m water depth, respectively, had observable gas bubbling up from the seafloor. Gas seepage rates were estimated at 1.48 and 0.01 $Mg \cdot yr^{-1}$ for 2A-1 and 2B-1, respectively (Table S2).

3.2.2. Gas geochemistry speciation and source origin of hydrocarbons

The hydrocarbon gases methane (C_1), ethane (C_2), propane (C_3), and carbon dioxide (CO_2) captured at these sites were measured by three different sampling techniques: *i*) captured ocean floor bubbling seep gas, *ii*) void gas pockets collected from the push core sediment by drilling through the corer liner, and *iii*) from the push core sediment's headspace gas trapped within either crimp sealed glass serum vials or Isojars. The bubbled seep gas collected at the ocean floor of both sites by the non-isobaric gas sampler is methane dominated (92.6% for 2A-1, The Hole and 90.7% for 2B-1, Clamshell, respectively) with the sum of all other hydrocarbon gases making up less than 0.1% of the bulk volume. The C_1/C_{2+3} ratios at both sites is >1000 (Table S3) indicating a biogenic origin for the gas (Whiticar, 1999; Milkov and Etiope, 2018). Where known, CO_2 averaged 2.2% of the gas volume.

3.2.3. Carbon and hydrogen isotope geochemistry

Methane carbon ($\delta^{13}C$) and hydrogen (δD) isotopic composition of the non-isobaric gas collected bubbled seep gas from The Hole and Clamshell are nearly identical ($\delta^{13}C$ narrowly ranging from -70.6 ±0.2 to -71.0 ±0.3‰ and δD ranging from -193.5 to -199.5‰) (Fig. 3.2A; Table S4). The $\delta^{13}C$ values closely align between seep, void, and sediment headspace gas indicating a biogenic origin (Fig. 3.2B and S7). However, the void space and headspace gas isotope values of each site have larger ranges that likely indicate a significant kinetic isotope effect (KIE). Site 2A-1 where the gas discharge rate is highest has a max/avg ^{13}C fractionation range ($\varepsilon_{\text{seep–sediment sampled gas}}$) of 13.4 and 6.3‰, respectively. For ^{2}H it is -66.8 and -58.2‰, respectively (Table S5). For site 2B-1 where the gas discharge rate is low the max/avg range of ^{13}C fractionation ($\varepsilon_{\text{seep–sediment sampled gas}}$) is 13 and 5.5‰, respectively and for ^{2}H is -35.5 and -20.7‰. The contrast in the range of isotope values is likely due to the different seepage rates at each site along with potentially variable sources of methane production and oxidation reaction occurring by the chemosynthetic seep fauna within the shallow sediments.

3.2.4. Clumped methane isotope geochemistry

Nine samples from site 2A-1 (The Hole) and 2B-1 (Clamshell) seep sites were collected for methane clumped isotope analyses (Table S4). These represent two seep gas samples with replicates (n=4), three void gas samples and two sediment gas samples. Collectively the gas speciation, carbon and clumped isotopic data indicate the methane emitted from these two seeps was formed by microbial carbonate reduction (i.e., hydrogenotrophic methanogenesis) (Fig. 3.2B):

$$CO_2 + 4H_2 \rightarrow CH_4 + 2H_2O \quad (2)$$

Clumped isotopes of methane can be used to determine the formation temperature of the hydrocarbon gas when under equilibrium conditions (Stopler et al., 2014; Stopler et al., 2015).

Only the gas samples collected directly from the bubbling seep of both sites yielded clumped methane isotope values marking an equilibrium fractionation (Wang et al., 2015) (Fig. 3.2C). The other sampling methods (void and sediment headspace gas collection) produce a range of increasingly fractionated isotope values that progressively depart from meaningful equilibrium formation temperature estimates. These results therefore indicate methane oxidation of gas microseepage in shallow sediments either overprints the original methane formation temperature or represents methane entirely sourced from the shallow sedimentary environment that undergoes its own non-equilibrium fractionation kinetics (Giunta et al., 2022; Gropp, 2022). These results also suggest the accurate determination of deep basin methane formation temperatures can only be achieved through direct sampling of ebullient gas.

The ebullient methane of the non-isobaric gas collected seep samples from sites 2A-1 and 2B-2 produced $\Delta^{13}CH_3D$ values of 4.6 and 4.9 ‰ (Table S4; Fig. 3.2B-C and Fig. S8) that record apparent geothermal temperatures of $64^{+9.5}_{-9.5}$, $55^{+9.5}_{-12.5}$ °C, respectively. These temperatures are at or near the 60 to 80 °C upper limit of microbial methanogenesis for marine sedimentary environments (Wilhelms et al., 2001; Inagaki, 2015) and may require faster CO_2 supply rates to sustain the archaeal community (Wilhelms et al., 2001; Head et al., 2003). Mapping these temperatures to the locally derived geophysical and modeled geothermal depth changes (OETRA, 2011) at the seep sites results in a methane formation depth of ~1000 m (Fig. 3.3) for both seeps. The predicted methane formation depths extend far below the underlying DHI onto the crest of the more deeply buried salt diapirs. This thickness of rock strata marks an organic lean interval with known poor petroleum generative potential. All other ROV visited seep sites produced elevated sediment head space gas of biogenic (n=7) and mixed biogenic/thermogenic (n=1) origin or no elevated gas content (n=3). Collectively, for this region of the Scotian Slope, when the gas geochemical results

of this cruise are merged with three prior piston and gravity coring surveys (2015, 2016, and 2018) on the Scotian Slope (Fowler et al., 2017; Fowler et al., 2019), all but two gas producing sites yielded biogenic or a mixed biogenic/thermogenic gas (corresponding to diapirs hosting DHI #8 of the Shelburne survey area and DHI #37 of the Tangier survey; Table S1; Fig. 3.1, and Fig. S2 and S18).

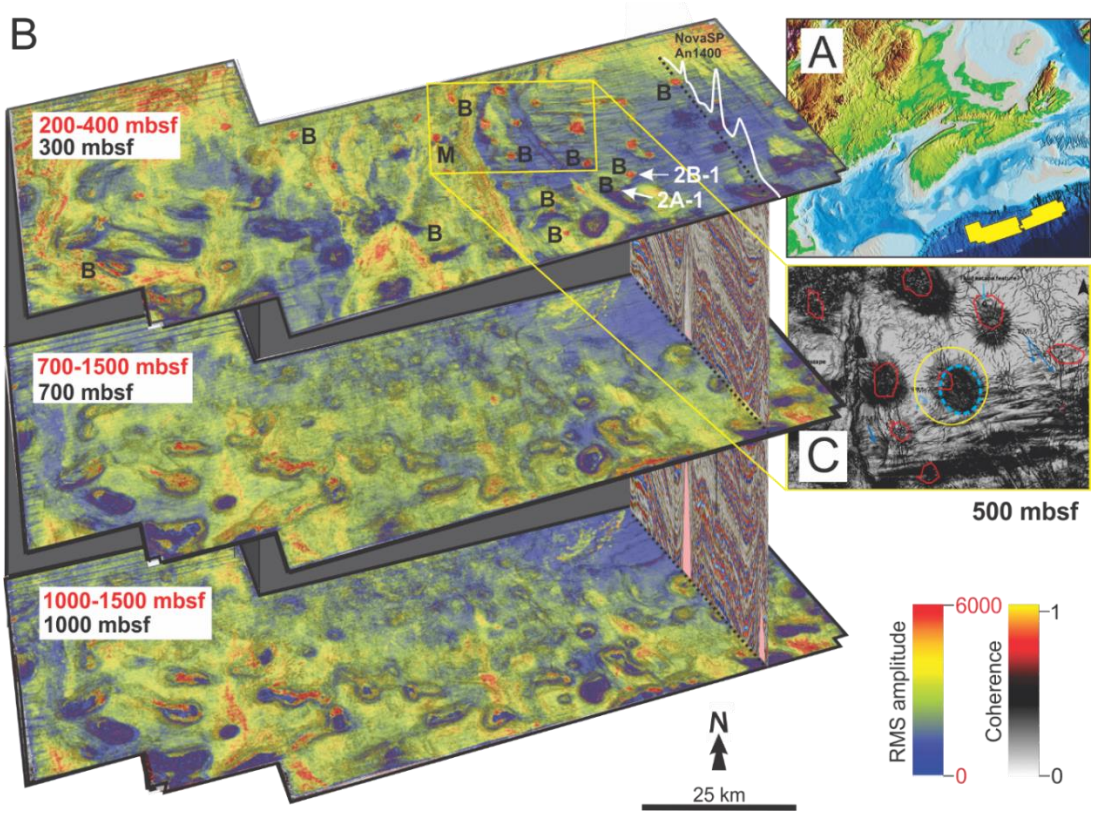

Figure 3.1. A) Map of the Scotian Slope, with yellow polygons indicating the locations of the Shelburne and Tangier 3D seismic surveys. B) Combined RMS amplitude and coherence maps of the Shelburne 3D data block for three different depth intervals in metres below sea floor (mbsf; red and black font for RMS amplitude and coherence, respectively) (see Fig. S1 for separate maps that include the Tangier survey). Brighter map colors indicate seismic amplitude anomalies with DHIs illuminated in red and other types of amplitude anomalies. The white line on right marks the ocean bottom sediment heat flow transect line from Negulic and Louden (2017) with a recorded DHI directly over a diapir (pink polygon in vertical 2D seismic crossline). Letters B and M indicate biogenic and mixed biogenic/thermogenic gas discoveries from ROV push core, gravity and piston coring surveys (Bennett and Desiage, 2012; Campbell and MacDonald, 2016; Campbell, 2016; Campbell and Normandeau, 2018). Locations of seep sites 2A-1 and 2B-1 are marked with arrows (See Fig. 3.3). C) Coherence maps showing the structure of the subsurface geology at 500 m depth below sea bottom showing geological structures such as radial and other crestal faults, effects of contourites, and intersected salt bodies. Ellipses indicates the boundary of radial faults (yellow), the boundary of intersected salt diapir (blue), and the region covered by the overlying DHI located at ~300mbsf (red).

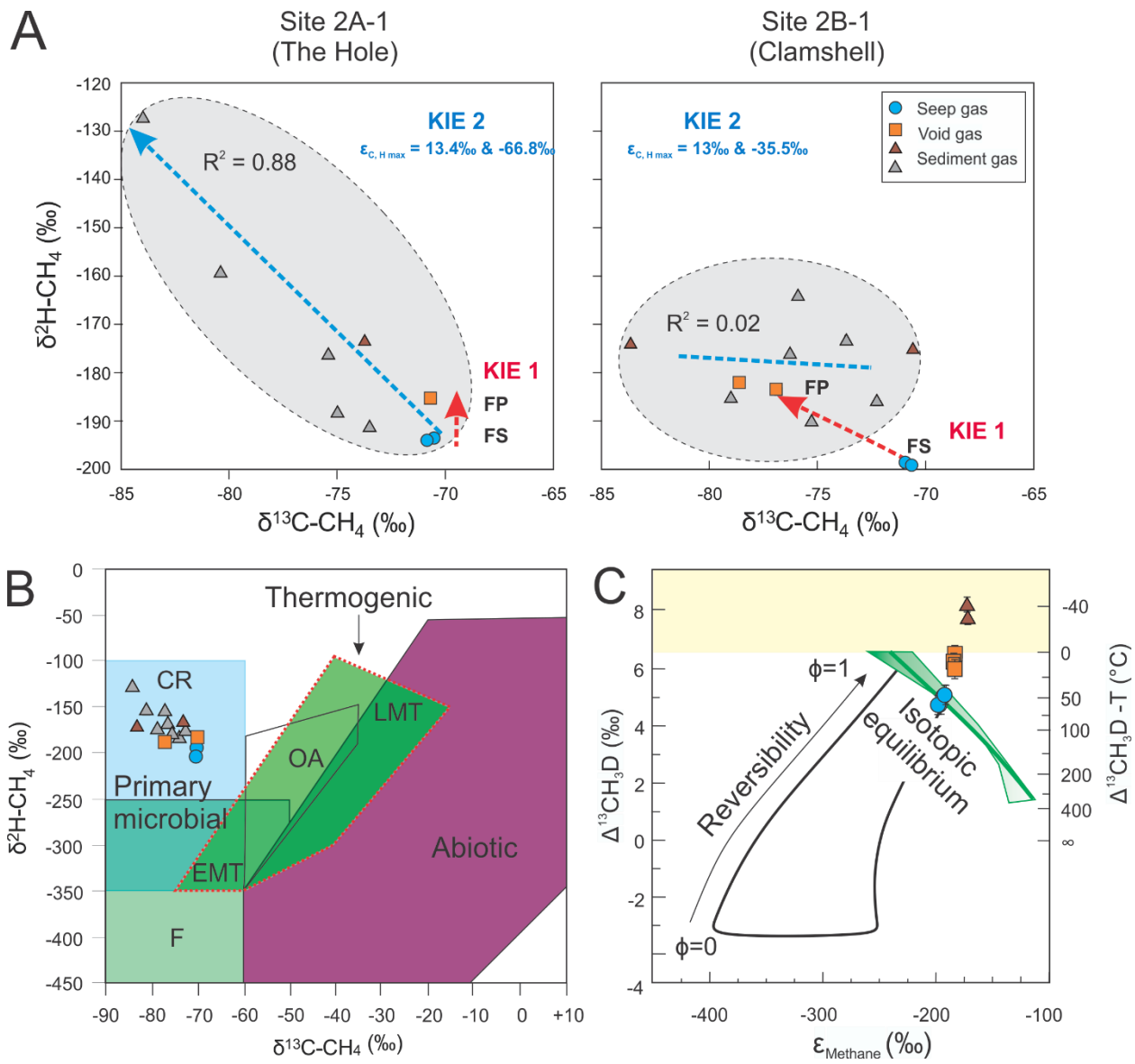

Figure 3.2. A) Bulk hydrogen and carbon isotope cross-plots from sites 2A-1 and 2B-1 for directly sampled seep gas (blue circles), push core void space (orange squares), and sediment head space gas (gray triangles, this study; brown triangles, Fowler, 2022). Two kinetic isotope effects (KIEs) are identified with FP and FS indicating fractionation from substrate and product, respectively (grey circle 90% confidence ellipse). B) Bulk methane carbon and hydrogen isotope cross-plot with microbial carbonate reduction (CR), fermentation (F), early mature thermogenic gas (EMT), oil-associated thermogenic gas (OA), and late mature thermogenic gas (LMT) source fields (Whiticar, 1999; Milkov and Etiope, 2018). C) Methane clumped isotope vs $\varepsilon_{Methane}$ cross-plot showing $^{13}CH_3D$=$^{12}CH_4$ chemical isotopic reversibility (Φ ranging 0 to 1), derived methane formation temperatures in relationship to isotopic equilibrium (Wang et al., 2015).

3.3. Discussion

3.3.1. Salt tectonism and the local petroleum system

Almost all identified DHIs across this portion of the Scotian Slope are found directly over top salt diapirs. They extend laterally outward to no further than the radius of the underlying salt structure (Fig. 3.4A). Such a confined fluid hosted setting is difficult to explain for this petroleum-producing basin. Prominent potential structural traps are abundant off-axis of most DHI hosted salt structures due to the extensive network of crestal faulting, the presence of anticline-generating bedforms in contourite deposits at a similar stratigraphic level, and widespread distribution of a variety of other potential stratigraphic seals at lateral pinch-outs at sites of onlap or truncation beneath erosional unconformities (Fig. 3.3, and S10–S18). Furthermore, larger fault systems including growth faults are common adjacent to, but also sometimes independent of the salt diapirs themselves. The many stratigraphic pinch-outs on the flanks of minibasins or growth-fault-related anticlinal traps would similarly also produce seismic amplitude anomalies if they were appropriately charged. Yet these off-diapir structures do not have clear DHIs in the investigated 1500 m thickness of the RMS amplitude maps or seismic sections. Furthermore, only 27 % of the diapirs have recognizable DHIs or gas chimneys. Most DHIs appear in the northern, more shallow-water sections of the Shelburne survey, where the diapirs are more deeply buried, suggesting the thickness of cover also has a relationship to DHI development (Fig. 3.1 and S2–S3).

3.3.2. Methane and its assent from the subsurface

The sampled methane directly seeping from the deep subsurface may in some cases have changed from its original isotopic composition. Equilibrated free methane can become trapped at the base of the GHSZ where it is unlikely to re-equilibrate. The gas is then subject to release by sublimation on the top horizon of the GHSZ (Lalk et al., 2022). Isotope fractionation associated with this

process is poorly constrained but expected to affect δD and not $\delta^{13}C$ values by a few per mil (Hachikubo et al., 2007). Furthermore, for our study, the small DHIs along with a high discharge rate over a pronounced daipir crest to seafloor reaching crestal fault suggests a GHSZ bypass for site 2A-1, The Hole (Fig. 3.3; Table S2). The ascent of methane from the deep subsurface is therefore unlikely to have significantly changed the recorded formation temperatures. Equilibrium or near-equilibrium isotopologue values reflect environmental condition and process not source material. As such, clumped methane isotopologues cannot clearly resolve initial microbial metabolism carbon substrates derived from the biodegradation of thermogenic hydrocarbons as opposed to direct carbonate reduction. Nonetheless for our survey, the biodegradation of thermogenic hydrocarbons is unlikely given the absence of thermogenic gas and the $\delta^{13}C_{CH4}$ and δD_{CH4} being most consistent with non-biodegradation (Fig. S7).

3.3.3. Gas production by deep biosphere oases

The dominance of biogenic gas production in what are traditionally viewed as a potential thermogenic petroleum play areas is noteworthy. While active microbial activity is known to occur in relation to salt tectonism, the processes have largely focused on downward migrated marine and meteoric water sourced fluid dissolution of anhydrite supplying Ca^{+} and importantly sulfate that is in turn coupled to hydrocarbon oxidation by AOM (Drake et al., 2017; Caesar et al., 2019). The sustained production of Ca^{+} and bicarbonate (DIC) is regarded as a mechanism of cap carbonate formation in a process that may reduce methane emissions, and thus represents a largely previously unrecognized carbon sink (Kotelnikova, 2002; Caesar et al., 2019).

Recent studies indicate there is an active and diverse microbial community inhabiting the near surface and deep buried sediments within the Scotian Slope (Dong et al. 2020; Gittins et al., 2022; Rattray et al., 2023; Li et al., 2023). Bacterial thermophilic endospores have been detected in

shallow surface and core sediments in the area, that are originally sourced from deep within the basin, brought to the surface through cold seeps (Gittins et al., 2022; Rattray et al., 2023). Their presence necessitates the existence of a deep biosphere that is likely related to biodegradation of hydrocarbons from yet unknown petroleum-hosting reservoirs. However, little is known about methanogenic archaea in this region's deep biosphere or how such communities exist beyond their coupled linkage to MSR via AOM in other passive margin settings. Mechanisms for why salt tectonism enhances deep biosphere carbonate methanogenesis are also largely absent in the literature. Methanogenic archaea require an inorganic carbon source such as CO_2 or acetate (more common to freshwater environments) and nutrients for their metabolic function. Many archaea, especially those engaging in methanogenesis, AOM and anaerobic oxidation of ammonia further require metabolites to keep their cells actively growing. The most likely sources of metabolites are input from adjacent formation waters, the partial dissolution of halite, anhydrite, and gypsum, and by input from the overlying ocean water column (Caesar et al., 2019). Why such biologic growth factors should be preferentially enriched above a select number of salt diapirs requires further mechanistic influences.

3.3.4. Heat chimney effect and convective flow model

Salt is an effective conductor of heat. Its thermal conductivity is 6.1 $W \cdot m^{-3} \cdot K^{-1}$ at 0 °C, decreasing to 4.1 $W \cdot m^{-3} \cdot K^{-1}$ at 100 °C (Canova et al., 2018). The thermal conductivity is much higher than typical clastic and carbonate sediments values that range from 1.5–2.5 $W \cdot m^{-3} \cdot K^{-1}$ (Birch and Clark, 1940). This well-known feature within salt provinces is credited for elevating the thermal maturity of source rocks above salt structures and the cooling of rocks that lie below or adjacent to salt bodies (Mello et al., 1995). The differential heat flow focused atop diapirs is known as a salt chimney effect (Wilson and Ruppel, 2007; Zhuo et al., 2016; Canova et al., 2018). For the

Shelburne Subbasin, a regional seafloor surface sediment heat flow of 35 $mW \cdot m^{-2}$ has been established (Negulic and Louden, 2016). The heat flow dramatically increases precisely overtop deeply buried diapirs (for example reaching 45 $W \cdot m^{-2}$ over top of diapir #14; Fig. 3.1 and Fig. 3.4A) (Negulic and Louden, 2016). The dramatic and predictable heat flow changes provide direct evidence of salt chimney effects within the Shelburne diapiric province. While the elevated heat flow represents a mechanism for deep formation water to reach the cold seep, it is unclear why biogenic methane production within such a diapiric petroleum system would also be elevated. Here we posit the contribution of convective flow from adjacent formation waters or from the overlying water column linked by radial faulting increase bicarbonate and nutrient supplies in a subsurface circulation cell. To evaluate hypothesis, we adopted a 2D isotropic numerical groundwater model for the prediction of subsurface convection based on classical Rayleigh-Taylor instability theory for a homogeneous sedimentary system (Fig. 3.4B; Table S6). For this model, Rayleigh numbers (R_e) ≥ 40 indicate unstable systems where convective heat transfer dominates the thermal behavior. Péclet numbers (P_e) ≥ 1 indicate groundwater flow will begin to alter the subsurface temperature field (Huysmans and Dassargues, 2005). A groundwater system undergoes convective flow when these two conditions are collectively met (Canova et al., 2018). The geothermal temperature estimates and depth profiles of DHI sites for three hypothetical seafloor linked convective cells were tested in the isotropic sediment-groundwater flow model: (1) down to the depth of the DHI; (2) to the top of the diapir; and (3) to the base of the diapir. From these parameters, only the deepest convective cell (3) is predicted to form in a partial number of DHI locations (Fig. 3.4B; Table S6). However, changing the sediment permeability (see Table S6 for details) to incorporate expected fluid movement along the radial fault splays results in predicted convective flow for the hypothesized ocean floor-top of the salt diapir circulation cell (2). The shallowest circulation cell

reaching down to the DHI (1) was not found to have favorable conditions for fluid circulation (Fig. 3.4B; Table S6).

While direct evidence of advective flow comes from the presence of the seeps, and more specifically, the seepage rate of gas ebullition at sites 2A-1 and 2B-1 (Table S2); evidence of convective seawater flow is expectedly more difficult to obtain as the net downward flux is expected to be non-linearly divided across the total number of radial fault limbs (i.e., >20 faults for site 2A-1). Additionally, although numerical modeling suggests conditions could enable convective flow, other factors must also affect seep formation as not all diapirs form DHIs or produce gas chimneys. We therefore investigated the geometric relationship between a diapir and the overlying sediment strata as a further control on a cold seep–diapir complex. A ratio of the diameter of the salt's heat chimney (assumed here to be the diameter of the salt diapir) to the diameter of the radial fault system at its closest point to the seafloor (herein referred to as its η value) is used as a means of determining the capacity for convective flow from the overlying ocean water column. When compared to the diapir's depth from the ocean floor (Fig. 3.4C), DHI sites appear to have variable $\eta \geq 1.2$ values. Except for the only detected thermogenic gas site (Fig. S19), DHI-hosting diapirs are also deeply buried ($\geq$ 1000 mbsf). For our study region, diapirs that do not host DHIs have a broader range of diapir depths, but generally much less extensive radial fault systems (lower η values). These results suggest convective influxes of DIC- and nutrient-rich seawater may contribute to the elevate methanogenic activity of the deep biosphere if the radial fault system sufficiently extends beyond the permitter of the diapir's heat chimney.

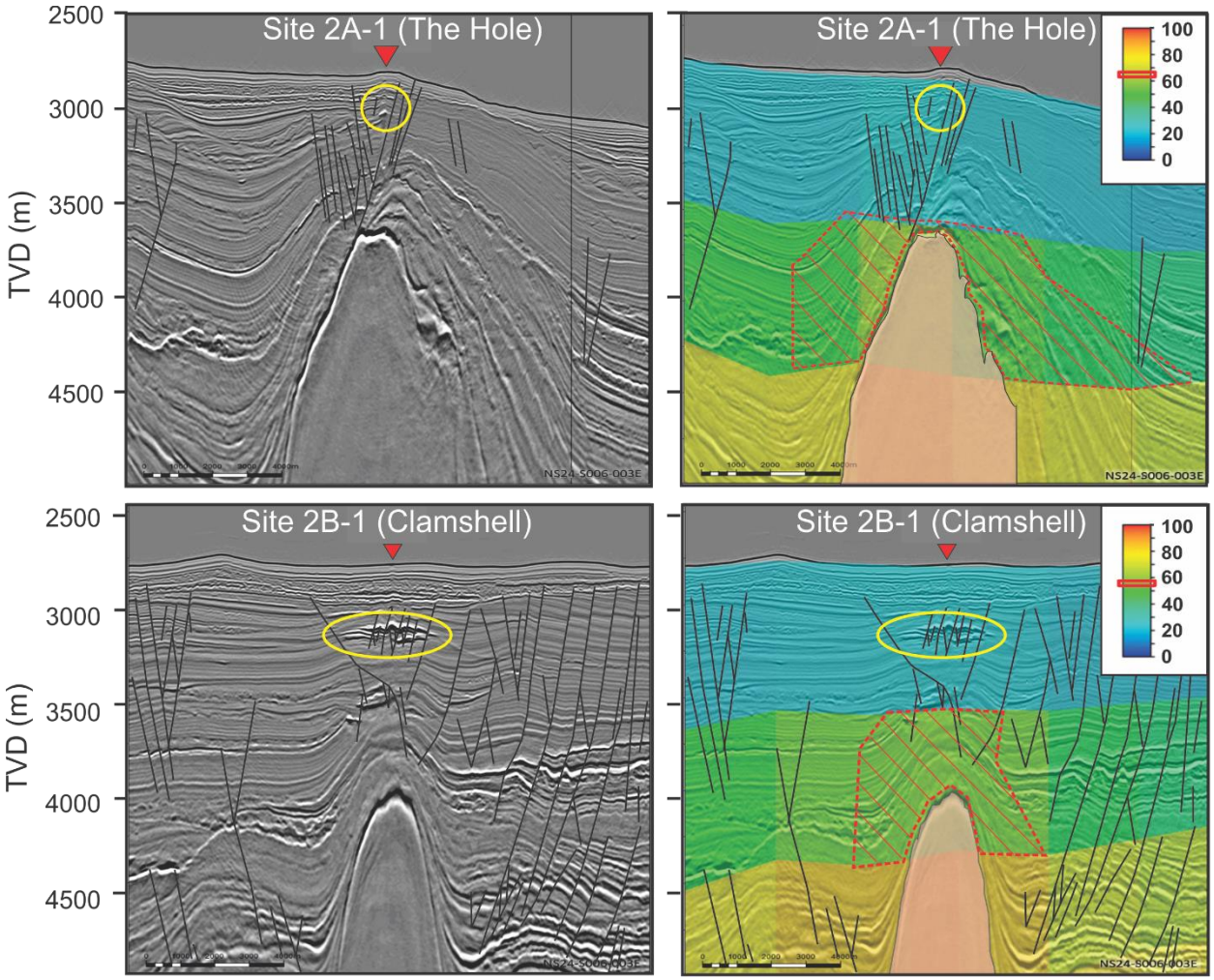

Figure 3.3. 2D seismic inline cross-sections of seep sites 2A-1 and 2B-1 (red upside-down triangles). Yellow ellipses mark DHI locations. Black lines denote faults. Colored background (right-hand panels) show modeled geothermal temperature changes (OETRA, 2011). Red polygons outline the possible area of methane formation based on derived methane isotopologue formation temperatures, modeled geothermal basin temperature gradients showing heat chimney effects, and structural relationships in the basin that could allow for fluid transport.

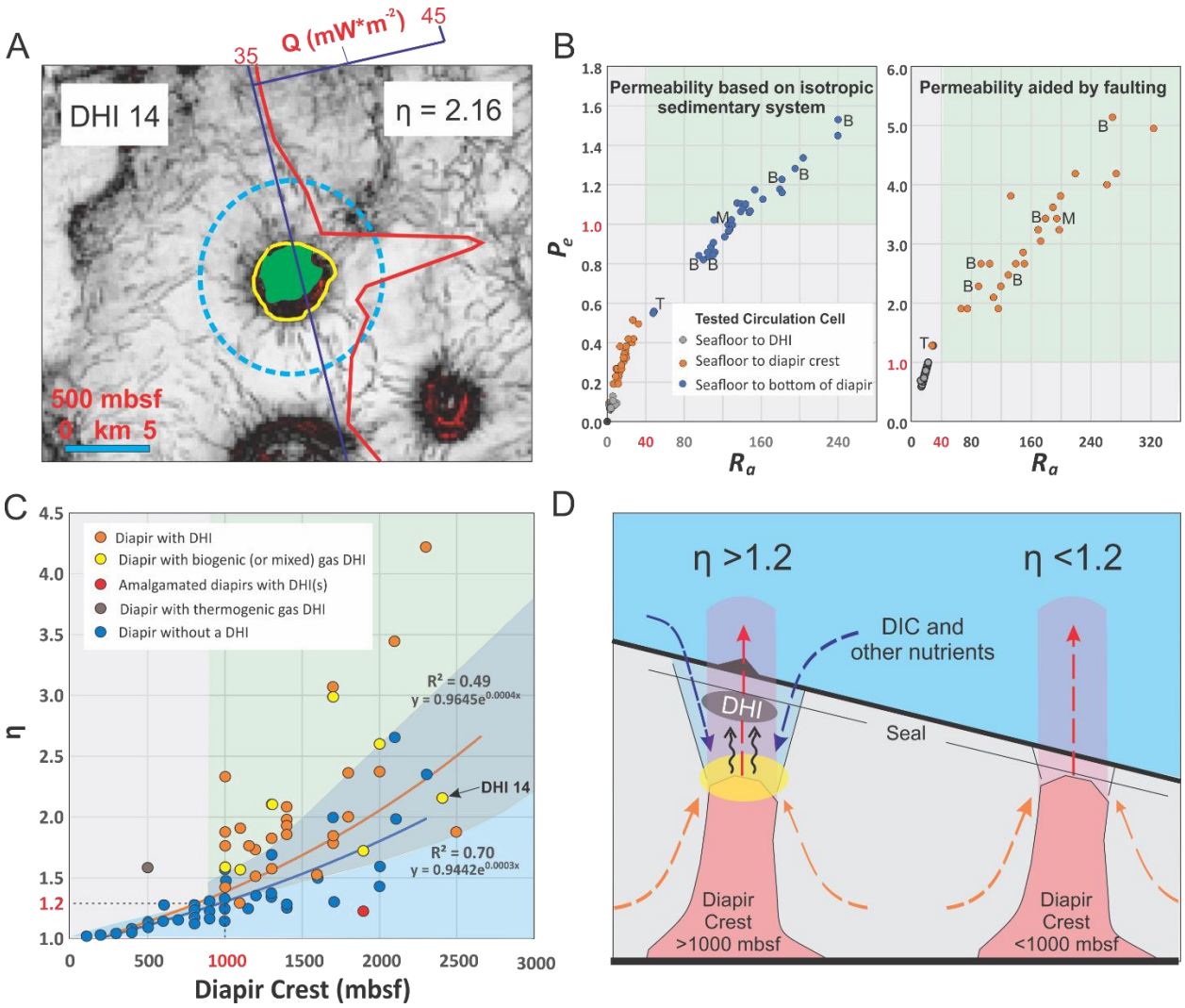

Figure 3.4. A) Coherence map of DHI 14 (green polygon) showing the location and diameters of its underlying salt diapir (yellow line) and the horizontal extent of the resulting radial fault system (blue dotted line). Red lined graph indicates measured ocean floor sediment heat anomalies resulting from the salt diapir (Negulic and Louden, 2016). B) Cross-plots of numerical modeled Rayleigh (R_a) and Péclet numbers (P_e) for different hypothesized basin circulation depths considering isotropic sediment (left) and fault impacted (right) permeabilities (green fields indicate conditions favorable for convective flow) (B, T, and M mark diapir sites with biogenic, thermogenic and mixed source methane) (Table S6). Conditions for ground water circulation are reached when R_a and P_e values are ≥ 4 and 1, respectively. C) Cross-plot of the Shelburne and Tangier salt diapir depths and the ratio of a diapir's diameter to its overlying radial fault diameter (referred to here as its η value) indicating diapirs are typically found at ≥1000 mbsf with a η ≥ 1.2. D) Model of DHI and cold seep formation. When diapirs that produce radial fault systems have high enough η, cold, nutrient-rich seawater is able to convectively flow to the diapir crest where it enhances deep biosphere methane production. When diapirs reach close to the ocean floor or have narrow radial faults their η values converge to 1, thereby removing the potential of convective flow from the overlying water column.

3.4. Conclusion

This study provides evidence that cold seeps can form as a complex interdependent system linking the deep biosphere to salt tectonism and ocean and groundwater circulation. In this context the deep biosphere is shown to be responsible for creating and sustaining the existence of what can be some of the most diverse ecosystems on the deep ocean floor. We provide a model for downward transport of DIC- and nutrient-rich ocean bottom water through the crestal fault network that elevates biogenic methane production to create a deep biosphere oasis of methanogenic Archaea immediately around and above deeply buried salt diapirs. The produced fluids rising up are aided by the elevated geothermal gradient from the salt diapirs that appears to be fueling many of the ocean floor cold seeps along the continental slope of the Scotian Margin. As the biotic feedback loop appears dependent on the larger diapir-fault architecture, the source of gas for many salt provinces' cold seeps may be predictable based on their deeper geophysical character. These results may therefore lead to better predictive models of where cold seeps can form and the type of hydrocarbons they might host.

3.5. Methods

3.5.1. Geophysical Surveys

The upper 5500 m of the Shelburne 3D Seismic Survey (conducted by Shell Canada Ltd. in 2013), a large, wide azimuth survey with a coverage of 10400 km^2 (RPS, 2013; Canada-Nova Scotia Offshore Petroleum Board (CNSOPB) program number NS24-S6-3E) was investigated alongside the Tangier 3D Seismic Survey (conducted by BP Canada Exploration Ltd. in 2014, CNSOPB program number NS24-B71-1E) spanning 8000 km^2. Common depth point (CDP) bin spacing/output grid for Shelburne 3D is 6.25-m by 50-m (time sampling rate: 2 ms). The Shelburne survey used both full 3D anisotropic Kirchhoff prestack time migration (PSTM) and full-volume

anisotropic Kirchhoff prestack depth migration (PSDM) with vertical transverse isotropy. BP Exploration Ltd. acquired four exploration licenses (Parcels 5 to 8; EL 2431-2434) from the Nova Scotia Call for Bids NS12-1 in the deep-water Scotian Slope. CDP bin spacing/output grid for Tangier 3D is 25 m and 25 m (time sampling rate: 2 ms). Size of the 3D seismic surveys (uncompressed). Both seismic surveys are in SEG-Y format and are post-stack, depth-migrated. Together these surveys range from ~500 to >4000 m water depths along the Scotian Slope.

These data blocks were mapped for the presence of DHIs and other types of seepage evidence and basin structural features that could promote migration of hydrocarbons using v2019 Schlumberger's Petrel © seismic software. Seismic horizons were picked based on the difference in reflection geometry, continuity, and configuration, known as seismic facies. Horizons were commonly chosen for mapping based on strong reflections with good continuity and differences in seismic facies. For this study, we picked and regionally mapped horizons across the shallow subsurface for both surveys. Seismic attributes analysis included root mean square (RMS) amplitude and coherence attribute extraction. For the Shelburne data block, RMS amplitude extraction search windows was ± 20 m from the chosen horizon. RMS amplitude maps were extracted for: 0, 200, 500, 750, 1000, 1500, and 2500 mbsf. For the Tangier data block, RMS amplitude extraction search window was ±25 m from the chosen horizon. RMS amplitude maps were extracted are: 3250 m (P1), 3000 m (N1), 2750 m (N2), 2500 m (N3), 2250 m (N4), 2000 m (N5), 1750 m (N6) from sea level. For both seismic surveys, the search window for coherence extraction was 0 m (i.e., at the horizon itself). DHIs are evaluated based on the nature of the amplitude anomalies (e.g., bright spots, dim spots, polarity reversal, etc.) which are unusual for their stratigraphic context (e.g., isolated amplitude anomalies). An anomaly was assigned as a fluid-derived "bright spot" DHI if a strong lateral amplitude variation is seen in seismic section

without characters typical of a stratigraphic feature (e.g., paleocanyon with expected distinct lithology, or an unconformity surface with compaction or cementation expected beneath it). If stratigraphic explanations are not tenable, and especially if there is a plausible structural control (e.g., truncation against a fault at a structural culmination), the amplitude anomalies are interpreted to be created by fluid migration. Seismic sections with prospective DHIs are annotated and highlighted to document the abundance of fluid-related amplitude anomalies. Isocore maps of seafloor to diapir crests for the Shelburne data block were also used to determine diapir depths (Table S1; Fig. S3).

3.5.2. Seep surveys

A 2020 autonomous underwater vehicle (AUV) cruise conducted by the Bedford Institute of Oceanography's CCGS Hudson, surveyed 10 prospective seep sites in the Shelburne and Tangier area based on the presence of DHI mapping and other geophysical data relating to fluid escape features and/or geochemical data generated from three prior piston and gravity coring surveys (Fig. S4) (Campbell, 2016; Campbell and MacDonald, 2016; Campbell and Normandeau, 2018). In 2020 the HUGIN 6000 AUV (Kongsberg Maritime) was deployed from the offshore supply ship Pacific Constructor. The AUV collected high-resolution geophysical data over a 2.5-km by 2.5-km area. It was steered ~40 m above the seafloor for multibeam bathymetric, side scan sonar, and sub-bottom profiling. Data collection was by a Kongsberg EM 2040 multibeam echosounder and an EdgeTech 2205 sonar system. The EM 2040 multibeam bathymetric data were acquired at a 400 kHz frequency, with a continuous waveform pulse and synchronized with Doppler velocity log. CARIS and EIVA suite was used for multibeam bathymetric data processing performed on the. Side scan sonar data was acquired at 230 kHz frequency with post data processing being completed with SonarWiz. The sub-bottom profiler operated over a 1–9 kHz frequency range with

a 20-ms pulse. High-resolution seismic data were integrated and analyzed using I Kingdom SuitIIHS Markit Ltd.). Acoustic travel times for high-resolution sub-bottom profiler lines were converted into depths using an average seismic velocity of 1500 $m \cdot s^{-1}$.

The resulting multibeam benthic maps were then used to direct a 2021 Triton XLX remote operated vehicle (ROV) operated by Helix Robotics Solutions Ltd., push core survey of the seep sites using the Atlantic Condor, operated by Atlantic Towing Ltd. Push core devices and core transport units (quivers) were designed by Todd Ventura and Jeremy Bentley at Saint Mary's University and built by Velocity Machining and Welding Ltd. in Dartmouth NS. Push core sediments were collected at "hot spot" locations deemed to be of scientific interest for all seep sites (Table S1; Fig. S5–S6) (Bennett and Desiage, 2012). High-definition video recordings were made using a Simrad OE 1366 SD color zoom camera (Kongsberg, Norway).

3.5.3. Sample collection and geochemical analysis

3.5.3.1. Seepage rate analysis

A seepage rate was measured by the collection of gas using a graduated funnel and measurement of the area of gas ebullition on the seafloor (Table S2). An annual rate of methane emission assuming all the hydrocarbon gas reached the ocean surfaces was calculated as

$$\frac{[(CH_4 molar\ mass \times CH_4 mole\ emission\ rate) \times 525{,}600s]}{1000000} \quad (3)$$

where the mole rate CH_4 emission is

$$\frac{P_{ocean\ bottom} \times Seepage\ rate}{RT_{ocean\ bottom}} \quad (4)$$

and the $P_{ocean\ bottom}$ was estimated by:

$$\rho \times g \times h \quad (5)$$

with ρ being the density of seawater at 1030 $kg \cdot m^{-3}$, g the acceleration due to gravity 9.81 $m \cdot s^{-2}$, and *h* the height of the overlying water column.

3.5.3.2. Gas sampling and analysis

Hydrocarbon gases (methane, ethane, and propane) were analyzed as captured from *i*) ocean floor bubbling seep gas, *ii*) void gas pockets inside of push corer liner, and from *iii*) push core sediment headspace gas (Tables S3-S4). Seep gas was directly collected from bubbles escaping the seafloor at sites 2A-1 and 2B-2 using a custom designed non-isobaric seep gas sampler (United States Provisional Application No. 63/392,224). Once onboard the vessel, the collected seep gas was transferred by hand pump to Isobags. Subsamples of push cores were collected for geochemical headspace analyses in which 5 mL of sediment from the base of the push corer was subsampled into a 20 mL glass serum vial with 5 mL 1M NaOH as a biocide. The serum vials were sealed using pre-treated (1 M KOH bath and rinsed overnight) Bellco blue butyl stoppers and stored in the refrigerator.

A 1 mL small aliquot of the head space gas was removed using a Hamilton airtight syringe and injected into an Agilent 7890 series gas chromatograph with a flame ionization detector (GC-FID) at Saint Mary's Department of Geology. The GC-FID was adapted with appropriate valve and injection systems by Wasson-ECE Instrumentation. Analysis of trace combustible hydrocarbon phases used an alumina-PLOT capillary analytical column (50-m×0.53-mm×10-μm) with a flow rate of 11.9 ±0.5 $mL \cdot min^{-1}$ of ultrapure He carrier gas. The initial oven temperature was set to 35 °C for 6 min, and then ramped 10 $°C \cdot min^{-1}$ to 200 °C for 2.5 min. Analysis of non-combustible volatile species (e.g., CO_2) were made using an alumina-PLOT analytical column (30-m×0.53-

mm×10-μm) with an 8.65 ±0.5 $mL \cdot min^{-1}$ flow rate of ultrapure He as the carrier gas. The oven temperature was initially set to 35 °C for 6 min, and then ramped 10 $°C \cdot min^{-1}$ to 110 °C for 7 min followed by a second ramp of then 20 $°C \cdot min^{-1}$ to 200 °C for 10 min. Identification and standardization of gas species was performed using standard gas mixtures supplied by Matheson Tri-Gas and SCOTTY® Specialty Gases. Lower limits of quantification are approximately 10^{-12} $mol \cdot L^{-1}$ varying slightly based on compound and further based on a minimum integration area of 0.5 units (i.e., in Agilent ChemStation software). Standards for quantification of gas and identification of gas peak retention time used Scott 1, Scott 2, and customised diluted standards. GC-FID runs were replicated at intervals to check for error and sensitivity of the process.

3.5.3.3. Void and sediment gas sampling and analysis

Void space samples were extracted from the push core liners using a hand drill and syringe. They were then stored in pre-evacuated 50 mL glass serum bottles. Whole-round core sediment samples (1.5-cm) were sectioned, and vacuum sealed into gas-barrier bags, and frozen at -80 °C until extraction. Extraction of gas from frozen sediment samples was accomplished using a custom designed gas extractor that thaws sediment samples under vacuum to minimize air contamination. The stainless-steel sample chamber in the gas extractor was kept at -20 °C using an isopropanol/LN bath while being loaded with frozen sediment. The cylinder was then placed under vacuum for 15 min before the cold bath was removed, and then warmed overnight to room temperature. A GC-FID was then used to measure the C_1 to C_3 gas concentrations of extracted gas. The GC-FID was equipped with a 10´column packed with HayeSep-Q (VICI), and operated at a temperature of 90 °C, with helium as the carrier gas, and calibrated using SCOTTY® gas mixes. Methane was extracted and purified from the total gas with a series of cryogen traps (dry ice, LN_2) using an automated preparative GC system (Wang et al., 2015).

3.5.3.4. Bulk stable isotope analyses

Stable isotope ratios of carbon (δ^{13}C-CH_4) and hydrogen (δD-CH_4) are reported (Table S4) using standard delta notation with Vienna Pee Dee Belemnite (VPDB) and Vienna Standard Mean Ocean Water (VSMOW) standards for the ratios $^{13}C/^{12}C$ and D/H:

$$\delta^{13}C = \frac{\left(\frac{^{13}C}{^{12}C}\right)sample}{\left(\frac{^{13}C}{^{12}C}\right)VPDB} - 1, \quad \delta D = \frac{\left(\frac{D}{H}\right)sample}{\left(\frac{D}{H}\right)VPDB} - 1 \qquad (6, 7)$$

Measured isotope values are reported in per mil (‰). The isotope scale was calibrated by the measurements of IAEA reference standards NGS-1 and NGS-3 (Wang et al., 2015). The δ^{13}C-CH_4 and δD-CH_4 values in this study are based on isotopologue absorption that are proportionally comparable to $^{13}CH_4/^{12}CH_4$ and D/H values (Lalk et al., 2022).

3.5.3.5. Clumped isotope analyses

The abundances of methane isotopologues were quantified using a Tunable Infrared Laser Direct Absorption Spectrometer (TILDAS) at the Isotope Geobiology Lab at MIT (Ono et al., 2014; Gonzalez et al, 2019). Cryogenically purified methane was extracted from each gas sample. The instruments' two bellows were loaded with equal volumes of commercial methane reference gas (AL1) along side a natural sample gas for 8-10 measurement cycles (Wang et al., 2015). Approximately 7–10 mL of methane (at room temperature and pressure) was used for analysis of seep gas collected by the nonisobaric gas sampler. For void and sediment gas samples, 1 mL of methane (at room temperature and pressure) was used for analysis. The TILDAS is a non-destructive analytical method. All measured sample-standard gas sample pairs were recovered for future use. Methane isotopologue abundances of the sample with respect to the stochastic

distribution was determined relative to the AL1 calibration reference gas (Wang et al., 2015). Isotopologue values are reported in per mil (‰) notation.

$\Delta^{13}CH_3D$ values are reported in per mil (‰) notation and represent the deviation of multiply substituted isotopologue $^{13}CH_3D$ abundance from that of the stochastic distribution in which:

$$\Delta^{13}CH_3D = ln\frac{[^{13}CH_3D][^{12}CH_4]}{[^{13}CH_4][^{12}CH_3D]} \quad (8)$$

A methane formation temperature is calculated from the $\Delta^{13}CH_3D$ sample values assuming the measurement us reflecting equilibrium conditions (Urey, 1947; Bigeleisen and Mayer, 2004). These measurements are therefore referred to as an 'apparent temperature'. The temperature-dependent equilibrium constant (K) from the isotopologue exchange reaction:

$$CH_4 + {}^{12}CH_3D \leftrightarrow {}^{13}CH_3D + {}^{12}CH_4 \quad (9)$$

is primarily a function of temperature, and the apparent temperature of equilibrium in Kelvin can be derived from $\Delta^{13}CH_3D$ values as:

$$\Delta^{13}CH_3D(T) = (-0.1101)\left(\frac{1000}{T}\right)^3 + (1.0415)\left(\frac{1000}{T}\right)^2 - (0.5223)\left(\frac{1000}{T}\right) \quad (10)$$

(Bigeleisen and Mayer, 2004; Urey, 1947). The temperature dependence for the value of $\Delta^{13}CH_3D$ (Eq. 10) can yield slightly different results from recent experimental calibrations (Webb and Miller, 2014; Wang et al., 2015; Lui and Lui, 2016; Eldridge et al., 2019) affecting both a reported $\Delta^{13}CH_3D$ value and the apparent temperature. However, the calibration uncertainty for $\Delta^{13}CH_3D$

values is less than the 95% confidence interval of our measurements (<0.1‰ vs ca. 0.2‰) and does not significantly alter the results with both approaches yielding consistent apparent temperatures within 1.5–4.0 °C with the calibration using Eq. (10) yielding slightly higher apparent temperatures (Lalk et al., 2022).

3.5.4. Heat flow modeling

The 2D modeled capacity for subsurface convection were based on modeled conditioned as presented by Canova et al. (2018). Calculation of the critical permeability threshold is based on the classical Rayleigh-Taylor instability theory to demarcate convective flow in a homogeneous system. Rayleigh numbers (R_a) were calculated based on the formula:

$$R_a = \frac{kz\beta\nabla T g}{\tilde{\nabla} K_\theta} \quad (11)$$

Where k is permeability, z is thickness of the reservoir, β water expansivity, ∇T is temperature chance over domain, g is gravity, K_θ is thermal diffusivity of saturated matrix, $\tilde{\nabla}$ is water viscosity (see supplemental for further details). For $R_a \geq 40$ indicate conditions of unstable systems where convective heat transfer will dominate the thermal behavior. Calculation of Péclet numbers was based on the formula:

$$P_e = \frac{Advectivetranferrate}{Diffusivetransferrate} = 0.056\left(\frac{kzg}{\tilde{\nabla}\Gamma K_\theta}\right)\gamma \quad (12)$$

Where Γ and ϒ are the ratio of volume heat capacity of saturated matrix to fluid and the coefficient of fluid density dependence on salinity, respectively. $P_e \geq 1$ indicate groundwater flow will begin to alter the subsurface temperature field. Data for the modeled parameters are obtained from this study's geophysical surveys (Table S1) as well as other published sources detailed in Table S6. We also introduce a fault convective transport capacity measure (η):

$$\eta = \frac{D_f}{D_d} \quad (13)$$

where D_f and D_d are the diameters of upper overlying radial fault system and the diameter of underlying salt diapir. The upward fault propagation angle (θ) was held to a constant 35° with the vertex residing within the diapir. The angle was determined based on a comparative review of diapir containing 2D seismic sections. The radial fault diameters were predicted based on the following function:

$$b_2 = 2\left(\frac{\lceil(h_2-200)+\left(\frac{0.5b_1}{tan\,(180-\theta)}\right)\rceil}{tan\theta}\right) \quad (14)$$

were b_1 is the measured diapir diameter and h_2 is based on isocore determined depths, Table S6; Fig. S3) and b_2 is the calculated diameters of the upper extent of diapiric radial fault propagation. Several DHI cross sections were mapped to test their agreement to the model based on a η value measured from the 2D inline cross sections (n=5). These tests resulted in ≥10% variance from the predicted diapir fault propagation estimate. The modeled diameters assume circular salt structures in aerial view. However, not all DHI hosted diapirs conform to this design. Some are more elliptical, or canopy shaped.

Acknowledgments

Technical support: Thanks to the Nova Scotia Provincial Government for support of this project and spear-heading the various research cruises and surveys that made the integrative data collection possible. A special thanks is given to Carey Ryan of Net Zero Atlantic was the GAPP Partnership Program manager responsible for the larger group research initiatives. Carey also managed the procuration and organization of the research cruises. An additional special thanks is given to Kim Doane, the executive director of the Department of Natural Resources and

Renewables for her support of the Organic Geochemistry Research Group at Saint Mary's University. Natural Resources Canada provided one of the AUV multibeam bathymetric maps used for the ROV seep survey. The push core cruise was conducted on the Atlantic Condor using Dalhousie University's MARUM MORI infrastructure. Jeff Seewald of Woods Hole Oceanographic Institution, Peter Guirguis of Harvard, and Andres Teske of University of North Carolina helped with push corer designs. Thanks to Britta Fiander of Genome Atlantic for supervision and guidance over the GAPP application and funding period. Thanks also to Andrew Stevens of Velocity Machining & Welding Inc., Dartmouth Nova Scotia for help with the manufacture of the non-isobaric gas sampler. Porewater chemical analysis was aided by undergraduate students Macy Giles, Elish Redshaw, and Andrew Drane. Clifford Voss of the Water Resources Research Center, University of Hawaii at Mānoa provided guidance for the numerical groundwater model. Funding for this project was sourced from: Genome Atlantic and Genome Canada; Research Nova Scotia (grant no. 2142); Mitacs (grant no. IT12481), NetZero Atlantic and the Nova Scotia Provincial Government for funding support to facilitate the AUV and ROV survey cruises. This research has been supported by the Natural Sciences and Engineering Research Council of Canada (grant no. RGPIN-2018-06147; NSERC), NSERC Canada Research Chairs (CRC) program, Canada Foundation for Innovation (CFI; JELF–CRC, John R. Evans Leaders Fund), NSERC Discovery Grants program (application no. RGPIN-2017-05822).

References

Albertz, M., Beaumont, C., Shimeld, J. W., Ings, S. J., & Gradmann, S. (2010). An investigation of salt tectonic structural styles in the Scotian Basin, offshore Atlantic Canada: 1. Comparison of observations with geometrically simple numerical models. Tectonics, 29(5), n/a.

Bennett, R., & Desiage, P.-A. (2022). Expedition report 21CONDOR: Scotian Slope, August 14-29, 2021. 53.

Bigeleisen, J., & Mayer, M. G. (1947). Calculation of equilibrium constants for isotopic exchange reactions. Journal of Chemical Physics, 15(6), 261–267. doi:10.1039/JR9470000562

Birch, A. F., & Clark, H. (1940). The thermal conductivity of rocks and its dependence upon temperature and composition. American Journal of Science, 238(8), 529–558.

Boetius, A., Ravenschlag, K., Schubert, C. J., Rickert, D., Widdel, F., Gieseke, A., ... & Pfannkuche, O. (2000). A marine microbial consortium apparently mediating anaerobic oxidation of methane. Nature, 407(6804), 623–626.

Caesar, K. H., Kyle, J. R., Lyons, T. W., Tripati, A., & Loyd, S. J. (2019). Carbonate formation in salt dome cap rocks by microbial anaerobic oxidation of methane. Nature Communications, 10, Article 808.

Campbell, D. C. (2019). CCGS Hudson Expedition 2016-011, phase 2. Cold seep investigations on the Scotian Slope, offshore Nova Scotia, June 15-July 6, 2016. (Report No. 88). Retrieved from https://geoscan.nrcan.gc.ca/starweb/geoscan/servlet.starweb?path=geoscan/fulle.web&search1=R=313603

Campbell, D. C., & MacDonald, A. (2016). CCGS Hudson Expedition 2015-018, geological investigation of potential seabed seeps along the Scotian Slope, June 25-July 9, 2015. (Report No. 75). Retrieved from file:///C:/Users/s8061240/Zotero/storage/XQXF32PU/servlet.html

Campbell, D. C., & Normandeau, A. (2019). CCGS Hudson Expedition 2018-041: High-resolution investigation of deep-water seabed seeps and landslides along the Scotian Slope, offshore Nova Scotia, May 26–June 15, 2018. Retrieved from https://geoscan.nrcan.gc.ca/starweb/geoscan/servlet.starweb?path=geoscan/fulle.web&search1=R=314695

Canova, D. P., Fischer, M. P., Jayne, R. S., & Pollyea, R. M. (2018). Advective heat transport and the salt chimney effect: A numerical analysis. Geofluids, 2018.

Deptuck, M. E., & Kendell, K. L. (2017). A review of Mesozoic-Cenozoic salt tectonics along the Scotian Margin, eastern Canada. In J. I. Soto, J. F. Flinch, & G. Tari (Eds.), Permo-Triassic Salt Provinces of Europe, North Africa and the Atlantic Margins (pp. 287–312). Elsevier. doi:10.1016/B978-0-12-809417-4.00014-8.

Dong, X., Cai, H., Ruppel, C. D., & Guo, J. (2020). Thermogenic hydrocarbon biodegradation by diverse depth-stratified microbial populations at a Scotian Basin cold seep. Nature Communications, 11(1), Article 5825.

Drake, H., Tullborg, E. L., & Åström, M. E. (2017). Isotopic evidence for microbial production and consumption of methane in the upper continental crust throughout the Phanerozoic eon. Earth and Planetary Science Letters, 470, 108–118.

Eldridge, D. L., Giunta, T., & Seewald, J. S. (2019). Comparison of experimental vs theoretical abundances of 13CH3D and 12CH2D2 for isotopically equilibrated systems from 1 to 500 °C. ACS Earth and Space Chemistry, 3(11), 2747–2764.

Foucher, J. P., Westbrook, G. K., Boetius, A. N. T. J. E., Ceramicola, S. I. L. V. I. A., DUPR, S., MASCLE, J., & MIENERT, J. (2009). Cold Seep Ecosystems. Oceanography, 22(1), 92.

Fowler, M., Webb, J., Gulbrandsen, S., Austnes, L.-K., & Ashraf, F. (2019). Geochemistry data report for 2018 Scotian Slope coring program.

Fowler, M., Webb, J., Olsen, H., Ashraf, F., & Guldbrandsen, S. (2017). Geochemistry data report for 2016 Scotian Slope piston coring program (Report No. 310).

Gittins, D. A., Heuer, V. B., Oni, O. E., Elvert, M., & Hinrichs, K.-U. (2022). Geological processes mediate a microbial dispersal loop in the deep biosphere. Science Advances, 8(3), eabn3485.

Giunta, T., Ashraf, F., Webb, J., Whiticar, M. J., Fowler, M., & Guldbrandsen, S. (2022). Extreme methane clumped isotopologue bio-signatures of aerobic and anaerobic methanotrophy: Insights from the Lake Pavin and the Black Sea sediments. Geochimica et Cosmochimica Acta, 338, 34–53.

Gonzalez, Y., Ono, S., Shusta, S. S., & Eiler, J. M. (2019). Precise measurements of 12CH2D2 by tunable infrared laser direct absorption spectroscopy. Analytical Chemistry, 91(23), 14967–14974.

Gropp, J., Jin, Q., & Halevy, I. (2022). Controls on the isotopic composition of microbial methane. Science Advances, 8(3), eabm5713.

Grunau, H. R. (1987). A worldwide look at the cap-rock problem. Journal of Petroleum Geology, 10(3), 245–265.

Hachikubo, A., Sakagami, H., & Tsutomu, U. (2007). Isotopic fractionation of methane and ethane hydrates between gas and hydrate phases. Geophysical Research Letters, 34(24).

Head, I. M., Jones, D. M., & Larter, S. R. (2003). Biological activity in the deep subsurface and the origin of heavy oil. Nature, 426(6964), 344–352.

Hudec, M. R., & Jackson, M. P. A. (2007). Terra infirma: Understanding salt tectonics. Earth-Science Reviews, 82(1-2), 1–28.

Huysmans, M., & Dassargues, A. (2005). Review of the use of Péclet numbers to determine the relative importance of advection and diffusion in low permeability environments. Hydrogeology Journal, 13(5-6), 895–904.

Inagaki, F., Hinrichs, K. U., Kubo, Y., Bowles, M. W., Heuer, V. B., Hong, W. L., ... & D'Hondt, S. (2015). Exploring deep microbial life in coal-bearing sediment down to ∼2.5 km below the ocean floor. Science, 349(6246), 420–424.

Jørgensen, B. B., & Boetius, A. (2007). Feast and famine—microbial life in the deep-sea bed. Nature Reviews Microbiology, 5(10), 770-781.

Joye, S. B., Bowles, M. W., Samarkin, V. A., Hunter, K. S., & Niemann, H. (2010). Biogeochemical signatures and microbial activity of different cold-seep habitats along the Gulf of Mexico deep slope. Deep Sea Research Part II: Topical Studies in Oceanography, 57(21-23), 1990–2001.

Judd, A., & Hovland, M. (2009). Seabed fluid flow: the impact on geology, biology and the marine environment. Cambridge University Press.

Kotelnikova, S. (2002). Microbial production and oxidation of methane in deep subsurface. Earth-Science Reviews, 58(3-4), 367–395.

Lalk, E., Diercks, A., Loher, M., Greinert, J., & Bohrmann, G. (2022). Clumped methane isotopologue-based temperature estimates for sources of methane in marine gas hydrates and associated vent gases. Geochimica et Cosmochimica Acta, 327, 276–297.

Levin, L. A., & Sibuet, M. (2012). Understanding continental margin biodiversity: a new imperative. Annual review of marine science, 4, 79-112.

Li, C., Peng, Y., Xu, H., Li, J., Xu, W., & Guo, J. (2023). Bacterial anomalies associated with deep sea hydrocarbon seepage along the Scotian Slope. Deep Sea Research Part I: Oceanographic Research Papers, 193, Article 103955.

Liu, L., Xu, W., Guo, J., Liang, J., Yang, C., & Ye, Y. (2022). Gas sources, migration, and accumulation systems: The shallow subsurface and near-seafloor gas hydrate deposits. Energies, 15(23), 6921.

Liu, Q., & Liu, Y. (2016). Clumped-isotope signatures at equilibrium of CH4, NH3, H2O, H2S and SO2. Geochimica et Cosmochimica Acta, 175, 252–270.

Mello, U. T., Karner, G. D., & Anderson, R. N. (1995). Role of salt in restraining the maturation of subsalt source rocks. Marine and Petroleum Geology, 12(6), 697–716.

Milkov, A. V., & Etiope, G. (2018). Revised genetic diagrams for natural gases based on a global dataset of >20,000 samples. Organic Geochemistry, 125, 109–120.

Mosher, D. C. (2011). A margin-wide BSR gas hydrate assessment: Canada's Atlantic margin. Marine and Petroleum Geology, 28(8), 1540–1553.

Negulic, E., & Louden, K. E. (2016). The thermal structure of the central Nova Scotia Slope (eastern Canada): Seafloor heat flow and thermal maturation models. Canadian Journal of Earth Sciences, 54(2), 146–162.

OETRA. (2011). Play Fairway Analysis Atlas – Offshore Nova Scotia. Nova Scotia Department of Energy Report, 347. Retrieved from https://oera.ca/research/play-fairway-analysis-atlas

Ono, S., Shusta, S. S., Boering, K. A., & Eiler, J. M. (2014). Measurement of a doubly substituted methane isotopologue, 13CH3D, by tunable infrared laser direct absorption spectroscopy. Analytical Chemistry, 86(13), 6487–6494.

Orphan, V. J., House, C. H., Hinrichs, K.-U., McKeegan, K. D., & DeLong, E. F. (2001). Methane-consuming Archaea revealed by directly coupled isotopic and phylogenetic analysis. Science, 293(5530), 484–487.

Paull, C.K., Hecker, B., Commeau, R., Freeman-Lynde, R.P., Neumann, C., Corso, W.P., Golubic, S., Hook, J.E., Sikes, E. & Curray, J. (1984). Biological communities at the Florida Escarpment resemble hydrothermal vent taxa. Science, 226(4677), 965-967.

Portnov, A., Pecher, I. A., Chen, T., Ruppel, C. D., & Paull, C. K. (2019). Clustered BSRs: Evidence for gas hydrate-bearing turbidite complexes in folded regions, example from the Perdido Fold Belt, northern Gulf of Mexico. Earth and Planetary Science Letters, 528, Article 115843.

Rattray, J. E., Zhang, Y., Xu, W., & Li, M. (2023). Elevated bacterial endospores associated with thermogenic hydrocarbon seeps in deep sea sediments. Organic Geochemistry, 177, Article 104568.

Ristova, P. P., Wenzhöfer, F., Ramette, A., Felden, J., & Boetius, A. (2015). Spatial scales of bacterial community diversity at cold seeps (Eastern Mediterranean Sea). ISME Journal, 9, 1306–1318.

Römer, M., Wintersteller, P., Elger, J., de Haas, H., Lepland, A., & Böttner, C. (2021). Seafloor methane seepage related to salt diapirism in the northwestern part of the German North Sea. Frontiers in Earth Science, 9, Article 649512.

Serié, C., Huuse, M., & Schødt, N. H. (2012). Gas hydrate pingoes: Deep seafloor evidence of focused fluid flow on continental margins. Geology, 40(3), 207–210.

Stolper, D. A., Lawson, M., Davis, C. L., Ferreira, A. A., Santos Neto, E. V., Ellis, G. S., ... & Formolo, M. J. (2014). Formation temperatures of thermogenic and biogenic methane. Science, 344(6191), 1500–1503.

Stolper, D. A., Sessions, A. L., Ferreira, A. A., Santos Neto, E. V., Schimmelmann, A., Shusta, S. S., ... & Eiler, J. M. (2015). Distinguishing and understanding thermogenic and biogenic sources of methane using multiply substituted isotopologues. Geochimica et Cosmochimica Acta, 161, 219–247.

Suess, E. (2014). Marine cold seeps and their manifestations: geological control, biogeochemical criteria and environmental conditions. International Journal of Earth Sciences, 103, 1889-1916.

Suess, E. (2018). Marine cold seeps: background and recent advances. Hydrocarbons, oils and lipids: Diversity, origin, chemistry and fate, 747-767.

Urey, H. C. (2014). The thermodynamic properties of isotopic substances. Journal of Chemical Society Resumed, 562–581. doi:10.1039/JR9470000562

Vanreusel, A., ANdERSEN, A.C., BoETIUS, A., Connelly, D., Cunha, M.R., Decker, C., Hilario, A., Kormas, K.A., Maignien, L., Olu, K. and Pachiadaki, M. (2009). Biodiversity of cold seep ecosystems along the European margins. Oceanography, 22(1), 110-127.

Wang, D. T., Gruen, D. S., Lollar, B. S., Hinrichs, K. U., Stewart, L. C., Holden, J. F., ... & Sessions, A. L. (2015). Nonequilibrium clumped isotope signals in microbial methane. Science, 348(6233), 428–431.

Webb, M. A., & Miller, T. F. I. (2014). Position-specific and clumped stable isotope studies: Comparison of the Urey and path-integral approaches for carbon dioxide, nitrous oxide, methane, and propane. Journal of Physical Chemistry A, 118(2), 467–474.

Whiticar, M. J. (1999). Carbon and hydrogen isotope systematics of bacterial formation and oxidation of methane. Chemical Geology, 161(1-3), 291–314.

Wilhelms, A., Larter, S. R., Head, I., Farrimond, P., di Primio, R., Zwach, C., ... & Zimmer, M. (2001). Biodegradation of oil in uplifted basins prevented by deep-burial sterilization. Nature, 411(6841), 1034–1037.

Wilson, A., & Ruppel, C. (2007). Salt tectonics and shallow subseafloor fluid convection: Models of coupled fluid-heat-salt transport. Geofluids, 7(4), 377–386.

Zhuo, Q. G., Meng, F. W., Zhao, M. J., Li, Y., Lu, X. S., & Ni, P. (2016). The salt chimney effect: delay of thermal evolution of deep hydrocarbon source rocks due to high thermal conductivity of evaporites. Geofluids, 16(3), 440-451.

Chapter 4. Key Conclusion and Future work

This thesis will help to further improve our sampling methodology for gas geochemistry studies and subsurface geochemistry within the Scotia Basin. The first experimental chapter (Chapter 2) elucidates the optimal storage container, the anticipated gas loss over varying durations, and the degree of methane retention within frozen sediment cores preserved in an unconfined state. Chapter 3 compares the optimal gas samples obtained from three distinct sampling methods, thereby elucidating the mechanisms underlying gas formation in the deep biosphere.

4.1. Chapter 2: gas loss and methane retention

Chapter 2 identified the extent of gas loss from plastic Isojars, demonstrating their suitability for short-term storage (<2-3 months) to determine head space gas composition, but lack of suitability for long term storage as over 75.5% of the gas was leaked from the headspace within 9 months. Furthermore, I found that frozen, unconfined sediment cores can retain methane gas for up to 3 years if the gas concentration exceeds 10,000 ppm. Two cores S49 and S21, exhibiting higher methane concentration (methane concentration) and a storage period of 3 years, revealed that the local SMTZ lies below 3.5 m for core S49 and 2.5 m for core S21.

4.2. Chapter 3: salt tectonics and deep biosphere

Chapter 3, which has been published (Chowdhury et al., 2024), led to the following conclusions: i) seep sites with higher rates of seepage exhibit lower kinetic gas fractionation; ii) direct seep gases represent the least attenuated samples; and iii) the source depth for direct seep gas at the Scotian Shelf is approximately 1 kilometer below the seafloor. The model facilitated understanding the circulation of fluids and nutrients through large-scale fractures in salt diapir active provinces, thereby triggering the production of deep biosphere biogenic gas seeps.

4.3. Future work

Based on the findings presented in Chapter 2 and Chapter 3, potential avenues for future research include:

i) Long-term gas storage evaluation: further investigation is warranted to explore the long-term storage capabilities of different container materials (butyl stopper capped 25 mL glass vial) beyond the 6-month timeframe (Lalk, 2023) assessed in Chapter 2. This could involve extended monitoring of gas retention (C_2–C_6) and leakage rates to inform the development of more durable storage solutions for gas samples in geochemical studies.

ii) Methane loss (storage) mechanisms: deeper exploration into the mechanisms underlying methane loss (storage potential) in frozen sediment cores, particularly focusing on the interplay between gas concentration levels and storage duration, could provide valuable insights. Understanding these mechanisms could enhance our ability to interpret methane dynamics in subsurface environments over extended timeframes.

iii) SMTZ characterization: continued investigation into the spatial variability and characteristics of the sub-seafloor methane oxidation zone (SMTZ), as inferred from the findings of Chapter 2, is essential. Detailed profiling of SMTZ depth and extent across different geological settings can contribute to a more comprehensive understanding of methane cycling processes and their implications for carbon cycling and climate dynamics.

iv) Refinement of gas seepage dynamics: building upon the conclusions drawn from Chapter 3 regarding the relationship between seepage rates and gas fractionation, future research could focus on refining models to better quantify these dynamics. This may involve integrating additional environmental parameters and observational data like (CH_2D_2 isotopologue) to enhance the

predictive capabilities of models for assessing gas seepage fluxes and their implications for biogeochemical cycling.

v) Exploration of salt diapir influence: further investigation into the role of salt tectonics in shaping deep biosphere processes, as highlighted in Chapter 3, is warranted. This could involve detailed geological and geochemical characterization of salt diapir provinces to elucidate their influence on fluid circulation patterns, nutrient transport, and the distribution of biogenic gas seeps in marine environments.

By addressing these research directions, future studies can contribute to advancing our understanding of gas geochemistry, subsurface biogeochemical processes, and the influence of geological factors on deep biosphere dynamics.

Reference

Lalk, E. (2023). The Biogeochemistry of Methane Isotopologues in Marine and Lacustrine Sediments. Massachusetts Institute of Technology. Chapter 4, pp. 138.

Supplementary Figures and Tables for Chapter 3

****

Supplementary figures and tables for Chapter 3

Title: Cold Seep Formation by Salt Tectonic Driven Deep Biosphere Enrichment

Authors: Chowdhury, A.[1], Ventura, G.T.[1], Owino, Y.[1], Lalk, E.[2], MacAdams, N.[3], Dooma, J.[1], Ono, S.[2], MacDonald, A.[3], Fowler, M.[4], Bennett, R.[5], MacRae, R.A.[1], Hubert, C.[6], Bentley, J.[1], Kerr, M. J.[1],

Supplemental Information

1. Supplemental Text
    a. Seep site descriptions
    b. Descriptions of structural constraints to the locations of DHIs.
2. Tables (S1 – S6)
3. Figures (Fig. S1 – S18)
4. Supplemental References

Supplement Text – Seep site dive descriptions summarized from Bennett and Desiage (2022)

Site 2A-1

The seep is characterized by an elongate shape-oriented NW-SE within radiating structure. Images recorded in the central part of the seep by the ROV show authigenic carbonates buildups populated by mussels/bivalves and sessile organisms. Authigenic carbonates are also the substrate of small patches of white, dark-grey, and light purple bacterial mats found around the area. Most of the larger mats (i.e., pluri-decimetric spots) are located at the edge of the seep overlying soft sediment as identified at the stations Deep Purple and Crusty White Clams (Fig. S4 and S5).

Five hotspot stations were identified:

Clam Hill: comprised of blocky carbonates, shells as well as dense patches of mussels/bivalves.
Deep Purple: identified by the presence of large, purple-colored microbial mats.
Holy Ground: in the vicinity of the seep, the seabed is mostly covered by soft structureless sediment with sporadic crater-like structure.
Crusty White Clams: selected for its blocky carbonates, shells as well as dense patches of mussels/bivalves.
The Hole: marked by authigenic carbonates forming a depression where a constant release of gas bubble was observed. Some bubbles were trapped as gas hydrates under a block of authigenic carbonates. The site was sampled with a push corer. Authigenic carbonates were also retrieved at the station.

Site 2B-1

The majority of the seafloor at 2B-1 is flat with extensive bioturbation identified by the abundance of sea urchin tracks, shallow depressions caused by an unknown organism, worm tubes. White and purple bacterial mats were observed. Similar to site 2A-1 authigenic carbonate buildups were populated with mussels/bivalves and sessile organisms. Infrequent gas bubbles were observed slowly emanating from the seabed in one location (sample site Tiny Bubbles). When the push cores were inserted into the seafloor at some of the coring locations at site 2B-1, gas bubbles were vigorously released from the seafloor (Coral Hill, Clamshell). Some of the cores also showed bubbling inside the tubes in the form of a cottage cheese texture, and/or ad gas cracking when they were examined on the deck of the Atlantic Condor. The warning alarm on handheld multi-gas detectors were triggered by the cores from this site. Sediment cores were collected at the following hotspots (Fig. S4 and S6):

Tiny Bubbles: was selected as being covered by a grey/white bacterial mat located near outcrops of carbonate material. Some infrequent gas bubbles were observed at this location. No bubbled gas samples could be collected.
Purple Patch: was named based on the presence of large, purple-colored bacterial mats.
Coral Hill: the push coring site was centered in a patch of sediment located on the flank of a large carbonate mound or chemoherm. Abundant benthic life was present at this location.

Clamshell: push cores were inserted into a patch of sediment located on the flank of a large carbonate mound or chemoherm. Abundant benthic life at this location. Gas collection was also conducted at this site.

A transect of push cores was also collected to investigate how hydrocarbon indicators in the sediment change with distance from the source. The coring site Tiny Bubbles was considered the base of the transect and then cores were collected 75, 40 and 25 m to the NW; and 75, 40, and 25 m to the SE of Tiny Bubbles.

Table S1. DHI locations and geophysical properties.

DHI#	(Lat) UTM27-20 X = easting (m)	(Long) UTM27-20 Y = northing (m)	Seismic survey	Proximal location in the DHI within the survey	Ocean depth (m)	DHI depth below seafloor (m)	Depth of diapir to seafloor (m)	Diameter of DHI (m)	Diameter of diapir Crest (m)	Estimated diameter of radial fault (m)	η ($D_{radial\ fault}/D_{diapir}$)	Fault pattern	Seal	Source of HCs
1	440547.05	4659686.11	Shelburne 3D	Northern	3100	360	1500	2050	4200	5437	0.74	Crestal and polygonal faults within the DHI	Hemipelagic + MTDs	
2	447432.73	4666936.28	Shelburne 3D	Northern	2215	372	1400	4200	3000	4165	1.20	Crestal and polygonal faults within the DHI	Hemipelagic + MTDs + contourites	
3	463772.52	4687940.14	Shelburne 3D	Northern	1950	366	1500	3800	1200	2437	4.96	Crestal and polygonal faults within the DHI	Hemipelagic + MTDs + contourites	
4	479707.1	4685072.17	Shelburne 3D	Northern	2055	305	1000	2600	3700	4501	0.95	Crestal and polygonal faults within the DHI	Hemipelagic + MTDs + contourites	Biogenic
5	489382.93	4675403.06	Shelburne 3D	Northern	2335	360	1700	2550	1850	2578	1.51	Crestal and polygonal faults within the DHI	Hemipelagic + MTDs	
6	503378.05	4680651.2	Shelburne 3D	Northern	2235	249	2000	1800	2050	3142	1.17	Crestal and polygonal faults within the DHI	Hemipelagic + MTDs	
7	512659.34	4683967.73	Shelburne 3D	Northern	2200	292	2000	2700	1650	2815	1.39	Crestal and polygonal faults within the DHI	Hemipelagic + MTDs	
8	524474.44	4688584.67	Shelburne 3D	Northern	2080	308	1700	4100	2000	2874	4.50	Crestal and polygonal faults within the DHI	Hemipelagic + MTDs	
9	528062.41	4700529.53	Shelburne 3D	Northern	1830	331	1900	4200	3050	3705	1.64	Crestal and polygonal faults within the DHI	Hemipelagic + MTDs	
10	516091.88	4674745.42	Shelburne 3D	Northern	2410	392	1800	2500	2500	3956	1.60	Crestal faults	Hemipelagic + MTDs	
11	497365.1	4658383.72	Shelburne 3D	Northern	2750	425	2500	2500	2900	3846	1.24	Crestal faults	N/A but hemipelagic sediments are present with hints of shallow canyons	
12	531414.07	4689081.48	Shelburne 3D	Northern	2185	333	1700	2100	2800	3819	1.07	Crestal and polygonal faults within the DHI	Hemipelagic + MTD + contourites	
13	529546.77	4678110.34	Shelburne 3D	Northern	2385	344	1600	2700	1200	3020	2.25	Crestal faults within the DHI	Hemipelagic + MTDs + contourite	
14	571203.66	4703681.28	Shelburne 3D	Northern	2055	325	2000	3800	2900	4720	1.28	Crestal and polygonal faults within the DHI	Hemipelagic + MTDs + contourites	Biogenic
15	552833.49	4696696.03	Shelburne 3D	Northern	2110	348	2100	9200	12000	13383	1.08	Crestal and polygonal faults within the DHI	Hemipelagic + MTDs	
16	545410.41	4692053.7	Shelburne 3D	Northern	2245	386	1400	7950	4000	5747	2.25	Crestal and polygonal faults within the DHI	Hemipelagic + MTDs + contourites	
17	535960.27	4697127.47	Shelburne 3D	Northern	1930	365	2000	7200	2050	3360	4.07	Crestal and polygonal faults within the DHI	Hemipelagic + contourite	
18	484436.09	4669612.36	Shelburne 3D	Northern	2350	310	1600	1700	1600	2474	1.16	Crestal and polygonal faults within the DHI	Hemipelagic + MTDs	
19	526214.55	4683038.26	Shelburne 3D	Northern	2235	366	1400	2150	2300	3392	1.70	Crestal and polygonal faults within the DHI	Hemipelagic + MTDs + contourite	
20	539746.66	4655521.45	Shelburne 3D	Southern	2945	374	1800	1600	1150	2315	1.83	Crestal and polygonal faults within the DHI	Hemipelagic + MTD + contourite	Biogenic
21	591884.29	4695929.92	Shelburne 3D	Southern	2585	274	1600	1200	1000	1874	2.20	Crestal and polygonal faults within the DHI	Hemipelagic + MTD + contourite	
22	516382.88	4697634.12	Shelburne 3D	Northern	1880	372	2500	3800	1700	2865	3.41	Crestal and polygonal faults within the DHI	Hemipelagic + MTDs	Mixed
23	452620.46	4684499.83	Shelburne 3D	Northern	1910	338	2000	3000	2100	3410	1.6	Crestal and polygonal faults within the DHI	Hemipelagic + MTDs	
24	435674.77	4684555.2	Shelburne 3D	Northern	1920	294	1200	2200	1050	1778	1.7	Crestal and polygonal faults within the DHI	Hemipelagic + MTDs	
25	441558.01	4676395.87	Shelburne 3D	Northern	2040	343	1400	2400	2300	3392	1.76	Crestal and polygonal faults within the DHI	Hemipelagic + MTDs	
26	459227.93	4652759.94	Shelburne 3D	Northern	2490	322	1300	800	3300	3882	2.90	Crestal and polygonal faults within the DHI	Hemipelagic + MTD + contourite	
27	472911.38	4663711.4	Shelburne 3D	Northern	2435	265	1300	2200	2350	2932	1.67	Crestal and polygonal faults within the DHI	Hemipelagic + MTD	
38	558581.43	4691244.44	Shelburne 3D	Northern	2320	334	1100	1200	1850	3306	0.65	Crestal and polygonal faults within the DHI	Hemipelagic + MTD + contourite	
29	537457.32	4661782.23	Shelburne 3D	Southern	2785	278	1300	1950	2100	2755	0.74	Crestal and polygonal faults within the DHI	Hemipelagic + MTD + contourite	Biogenic
30	508212.68	4690838.26	Shelburne 3D	Northern	2095	285	1800	3600	2700	3574	1.46	Crestal and polygonal faults within the DHI	Hemipelagic + MTD	Biogenic
31*	579877.66	4696345.51	Shelburne 3D	Northern	2415	262	1350	1200	1800	2674	1.24	Crestal and polygonal faults within the DHI	Hemipelagic + MTD + contourite	
32*	555745.87	4672422.25	Shelburne 3D	Southern	2790	328	2600	1850	1600	2328	2.96	Crestal and polygonal faults within the DHI	Hemipelagic + MTD + contourite	
33	545726.59	4687845.89	Shelburne 3D	Southern	2240	349	1400	4350	1750	2332	1.69	Crestal and polygonal faults within the DHI	Hemipelagic + MTD + contourite	
34	547054.71	4675121.08	Shelburne 3D	Southern	2585	257	1600	1600	2200	3510	1.09	Crestal and polygonal faults within the DHI	Hemipelagic + MTD + contourite	
35	675188.38	4747660.37	Tangier 3D	Northern	2325	209	2400	2300	3000	5038	2.17	Crestal faults below the DHI	Hemipelagic + MTD?	
36	692389.94	4771825.87	Tangier 3D	Central	1635	450	2600	3500	7500	9247	1.76	Crestal faults below the DHI	Hemipelagic + MTD	
37	727388.29	4765397.62	Tangier 3D	Central	2320	229	500	1250	1200	1418	2.90	Directly above the diapir	Hemipelagic sediments	Thermogenic gas hydrates

– MTD - mass transport deposit.

* DHIs # 31 and 32 are sites 2A-1 and 2B-1, respectively

Table S2. Seepage rate estimates of 2A-1 and 2B-1. †

Calculation Parameters		Measurements	Methane	Ethane	Ethylene	Propane
2A-1 Seepage rate ($mL \cdot min^{-1}$)	15	Molar mass ($g \cdot mol^{-1}$)	16.04	30.07	28.05	44.097
Time (min)	1	Gas species (%)	99.24	0.52	0.00	0.06
Area of the site (m^2)	13	Seepage ($L \cdot min^{-1}$)	0.01	0.000078	0.00	0.000010
Depth (m)	2692	Mole rate ($n \cdot min^{-1}$)	0.18	0.0014	0.00	0.00017
Ocean Bottom Pressure (atm)	268	Seepage rate ($Mg \cdot yr^{-1}$)	1.48	0.02	0.00	0.00
Ocean Bottom Temperature (K)	277					
Molecular weight of methane (amu; $g \cdot mole^{-1}$)	16					
Other gases	H_2SO_4, CO_2 (max <0.5%)					
Gas constant (R; $J \cdot mol^{-1} \cdot K^{-1}$)	0.0821					
2B-1 Seepage rate ($mL \cdot min^{-1}$)	0.1	Molar mass ($g \cdot mol^{-1}$)	16.04	30.07	28.05	44.097
Time (min)	1	Gas species (%)	99.92	0.04	0.03	0.01
Area of the site (m^2)	5	Seepage ($L \cdot min^{-1}$)	0.00	3.79E-08	2.83E-08	6.27E-09
Depth (m)	2740	Mole rate ($n \cdot min^{-1}$)	0.00	6.63E-07	4.96E-07	1.10E-07
Ocean Bottom Pressure (atm)	273	Seepage rate ($Mg \cdot yr^{-1}$)	0.01	0.00	0.00	0.00
Ocean Bottom Temperature (K)	277					
Molecular weight of methane (amu; $g \cdot mole^{-1}$)	16					
Other gases	H_2SO_4, CO_2 (max <0.5%)					
Gas constant (R; $J \cdot mol^{-1} \cdot K^{-1}$)	0.0821					

† After: MacDonald et al. (2002) and Römer et al. (2017).

Table S3. Hydrocarbon gas geochemistry data.

Sample name	Hot spot location	Sample type	C_1 ($\mu L \cdot \mu L^{-1}$ total gas)	C_2 ($\mu L \cdot \mu L^{-1}$ total gas)	C_3 ($\mu L \cdot \mu L^{-1}$ total gas)	C_1 (%)	C_2 (%)	C_3 (%)	C_1/C_{2+3}	CO_2 (%) ‡
Site 2A-1										
SpG_The Hole 1*	The Hole	Seep gas	463.6	0.41	0.01	99.91	0.09	0.00	1104	NA
SpG_The Hole 2*	The Hole	Seep gas	463.6	0.41	0.01	99.91	0.09	0.00	1104	NA
VG_2A-1_ Hole*	The Hole	Void gas	68.3	0.09	0.01	17.1	0.02	0.01	704	0.03
SedG-3 (42cm)	The Hole	Sediment gas	12.5	0.04	0.00	99.68	0.32	0.00	312	3.65
SedG-27 (21cm)	Holy Ground	Sediment gas	1.2	0.00	0.00	100.00	0.00	0.00	>1000	0.13
SedG-101 (34cm)	Crusty White Clams	Sediment gas	5.6	0.01	0.00	99.82	0.18	0.00	564	2.98
Site 2B-1										
SpG_Clamshell 1*	Clamshell	Seep gas	453.3	0.38	0.01	99.91	0.08	0.00	1162	NA
SpG_Clamshell 2*	Clamshell	Seep gas	453.3	0.38	0.01	99.91	0.08	0.00	1162	NA
VG_2B-1_65 transect 40m SE*	Clamshell	Void gas	128.9	0.12	0.01	32.2	0.03	0.01	983	0.06
VG_2B-1_66 transect 25m SE*	Clamshell	Void gas	138.3	0.15	0.01	34.6	0.04	0.01	853	0.09
SedG-46 (7cm)	Tiny Bubbles	Sediment gas	4.9	0.02	0.00	99.59	0.41	0.00	246	1.99
SedG-46 (14cm)	Tiny Bubbles	Sediment gas	9.6	0.04	0.00	99.59	0.41	0.00	241	1.4
SedG-52 (8cm)	Purple Patch	Sediment gas	1.8	0.01	0.00	99.45	0.55	0.00	181	6.72
SedG-52 (32cm)	Purple Patch	Sediment gas	1.2	0.00	0.01	99.18	0.00	0.82	121	1.88
SedG-53 (3cm)	Clamshell	Sediment gas	4.9	0.01	0.00	99.80	0.20	0.00	494	1.28
SedG-53 (32cm)	Clamshell	Sediment gas	7.4	0.02	0.00	99.73	0.27	0.00	371	1.51
SedG-53 (32cm)	Clamshell	Sediment gas	7.4	0.02	0.00	99.73	0.27	0.00	371	0.6

* Measured at SMU.

‡ CO_2 concentration based on total gas.

Table S4. Stable isotope data of methane two seep gas site 2A-1 and 2B-1, void gas, and sediment gas.

Sample Name	Hot Spot Location	Sample Type	$\delta^{13}C$	Std	δD	Std	$\Delta^{13}CH_3D$	Std	T (°C)	+	-
Site 2A-1											
SpG_The Hole 1	The Hole	Seep gas	-70.8	0.06	-193.8	0.11	4.91	0.24	53	10	9
SpG_The Hole 2	The Hole	Seep gas	-70.6	0.05	-193.5	0.07	4.84	0.45	56	19	17
VG_The Hole	The Hole	Void gas	-70.7	0.04	-185.2	-	5.85	0.34	20	11	10
SedG_The Hole sediment	The Hole	Sed. gas	-73.7	0.20	-173.2	0.18	7.67	0.10	-28	4	4
SedG-9 (42cm)*	Deep Purple	Sed. Gas	-80.4	-	-159	-	-	-	-	-	-
SedG-48 (42cm)*	Deep Purple	Sed. Gas	-84	-	-127	-	-	-	-	-	-
SedG-57 (42cm)*	Holy Ground	Sed. Gas	-75	-	-188	-	-	-	-	-	-
SedG-59 (42cm)*†	Crusty White Clams	Sed. Gas	-44.5	-	-	-	-	-	-	-	-
SedG-67 (42cm)*	The Hole	Sed. Gas	-75.4	-	-176	-	-	-	-	-	-
SedG-95 (42cm)*	Holy Ground	Sed. Gas	-73.5	-	-191	-	-	-	-	-	-
Site 2B-1											
SpG_Clamshell 1	Clamshell	Seep gas	-70.7	0.12	-199.3	0.14	4.60	0.19	66	8	8
SpG_Clamshell 2	Clamshell	Seep gas	-71.0	0.1	-199.5	0.1	4.67	0.15	63	4	4
VG_2B-1_65 Transect 40m SE	Transect	Void gas	-76.8	0.17	-184.0	0.15	6.12	0.22	12	7	6
VG_2B-1_66 Transect 25m SE	Transect	Void gas	-78.6	0.26	-182.1	0.21	6.50	0.24	1.2	6	5
SedG-27 (21cm)	Clamshell	Sed. Gas	-71.7	0.10	-175.71	0.34	-	-	-	-	-
SG-62 (42cm)*	Clamshell	Sed. Gas	-79	-	-185	-	-	-	-	-	-
SedG-53 (32cm)	Clamshell	Sed. Gas	-83.7	0.15	-174.1	0.16	8.16	0.18	-40	4	4
SG-16 (42cm)*	Tiny Bubbles	Sed. Gas	-75.3	-	-190	-	-	-	-	-	-
SG-29 (42cm)*	Coral Hill	Sed. Gas	-76.3	-	-176	-	-	-	-	-	-
SG-30 (42cm)*	Purple Patch	Sed. Gas	-72.3	-	-186	-	-	-	-	-	-
SG-49 (42cm)*	Purple Patch	Sed. Gas	-75.9	-	-164	-	-	-	-	-	-

*Data acquired by Fowler (2022). Reproducibility of $\delta^{13}C$ is better than 1‰ (2σ) and δD values are better than 10‰ (2σ).

† Isotope value likely inaccurate due to sample being compromised during its storage and analysis.

Table S5. Measured seep site kinetic isotope effects (see Fig. 2A and 2B).

Sample name	$\delta^{13}C$ Isotope Fractionation (‰)						δD Isotope Fractionation (‰)					
	KIE 1 $\varepsilon_{SpG\text{-}VG}$		$\varepsilon_{VG\text{-}SedG}$		KIE 2 $\varepsilon_{SpG\text{-}SedG}$		KIE 1 $\varepsilon_{SpG\text{-}VG}$		$\varepsilon_{VG\text{-}SedG}$		KIE 2 $\varepsilon_{SpG\text{-}SedG}$	
	$\overline{x}$	Max.	$\overline{x}$	Max.	$\overline{x}$	Max.	$\overline{x}$	Max.	$\overline{x}$	Max.	$\overline{x}$	Max.
Site 2A-1	0	-0.1	6.3	13.3	6.3	13.4	-8.5	-8.6	-16.2	-58.2	-24.6	-66.8
Site 2B-1	6.85	-7.9	-1.4	6.9	5.5	13	-16.4	17.4	-4.4	-20	-20.7	-35.5

Table S6. Isotropic grown water circulation model.

Diapir #	k [*] (m^2)	k_f [*] (m^2)	z_1 [†] (m)	z_2 [†] (m)	z_3 [†] (m)	β ($°C^{-1}$)	ΔT_1 [‡] (°C)	ΔT_2 [‡] (°C)	ΔT_3 [‡] (°C)	g ($m^2 \cdot s^{-1}$)	kΦ ($m^2 \cdot s^{-1}$)	V ($m^2 \cdot s^{-1}$)	T	Υ wt. (%)$^{-1}$	Permeability based on fully lithified sedimentary system						Permeability increased by fault network			
															SF to bottom of diapir (z_1, ΔT_1)		SF to top of diapir (z_2, ΔT_2)		SF to bottom of DHI (z_3, ΔT_3)		SF to top of diapir (z_2, ΔT_2)		SF to bottom of DHI (z_3, ΔT_3)	
															R_a	P_e	R_a	P_e	R_a	P_e	R_a	P_e	R_a	P_e
1	2.5E-15	2.5E-14	6733	1900	432	0.00061	175	60	25	9.8	1.43E-07	6.3E-07	0.8	0.01	195	1.3	19	0.36	1.8	0.082	189	3.6	18	0.8
2	2.5E-15	2.5E-14	6183	1800	470	0.00061	175	60	25	9.8	1.43E-07	6.3E-07	0.8	0.01	180	1.2	18	0.34	2.0	0.090	179	3.4	20	0.9
3	2.5E-15	2.5E-14	5066	1900	440	0.00061	150	60	25	9.8	1.43E-07	6.3E-07	0.8	0.01	126	1.0	19	0.36	1.8	0.084	189	3.6	18	0.8
4	2.5E-15	2.5E-14	4390	1300	350	0.00061	145	60	25	9.8	1.43E-07	6.3E-07	0.8	0.01	106	0.8	13	0.25	1.5	0.067	129	2.5	15	0.7
5	2.5E-15	2.5E-14	4309	1200	451	0.00061	140	60	25	9.8	1.43E-07	6.3E-07	0.8	0.01	100	0.8	12	0.23	1.9	0.086	119	2.3	19	0.9
6	2.5E-15	2.5E-14	4764	1700	337	0.00061	140	60	25	9.8	1.43E-07	6.3E-07	0.8	0.01	111	0.9	17	0.32	1.4	0.064	169	3.2	14	0.6
7	2.5E-15	2.5E-14	5373	1800	405	0.00061	145	60	25	9.8	1.43E-07	6.3E-07	0.8	0.01	129	1.0	18	0.34	1.7	0.077	179	3.4	17	0.8
8	2.5E-15	2.5E-14	4917	1400	449	0.00061	150	60	25	9.8	1.43E-07	6.3E-07	0.8	0.01	122	0.9	14	0.27	1.9	0.085	139	2.7	19	0.9
9	2.5E-15	2.5E-14	4507	1100	488	0.00061	150	60	25	9.8	1.43E-07	6.3E-07	0.8	0.01	112	0.9	11	0.21	2.0	0.093	109	2.1	20	0.9
10	2.5E-15	2.5E-14	5795	2200	462	0.00061	145	75	25	9.8	1.43E-07	6.3E-07	0.8	0.01	139	1.1	27	0.42	1.9	0.088	274	4.2	19	0.9
11	2.5E-15	2.5E-14	5366	1500	525	0.00061	125	60	25	9.8	1.43E-07	6.3E-07	0.8	0.01	111	1.0	15	0.29	2.2	0.100	149	2.9	22	1.0
12	2.5E-15	2.5E-14	5122	1600	394	0.00061	150	65	25	9.8	1.43E-07	6.3E-07	0.8	0.01	127	1.0	17	0.30	1.6	0.075	173	3.0	16	0.7
13	2.5E-15	2.5E-14	6166	2700	476	0.00061	150	60	25	9.8	1.43E-07	6.3E-07	0.8	0.01	153	1.2	27	0.51	2.0	0.091	269	5.1	20	0.9
14	2.5E-15	2.5E-14	8039	2700	443	0.00061	180	60	25	9.8	1.43E-07	6.3E-07	0.8	0.01	240	1.5	27	0.51	1.8	0.084	269	5.1	18	0.8
15	2.5E-15	2.5E-14	5916	2100	459	0.00061	165	75	25	9.8	1.43E-07	6.3E-07	0.8	0.01	162	1.1	26	0.40	1.9	0.087	261	4.0	19	0.9
16	2.5E-15	2.5E-14	7611	2600	482	0.00061	190	75	25	9.8	1.43E-07	6.3E-07	0.8	0.01	240	1.4	32	0.49	2.0	0.092	323	4.9	20	0.9
17	2.5E-15	2.5E-14	5816	2000	438	0.00061	140	60	25	9.8	1.43E-07	6.3E-07	0.8	0.01	135	1.1	20	0.38	1.8	0.083	199	3.8	18	0.8
18	2.5E-15	2.5E-14	5238	1400	412	0.00061	145	45	25	9.8	1.43E-07	6.3E-07	0.8	0.01	126	1.0	10	0.27	1.7	0.078	105	2.7	17	0.8
19	2.5E-15	2.5E-14	4501	1700	459	0.00061	140	70	25	9.8	1.43E-07	6.3E-07	0.8	0.01	105	0.9	20	0.32	1.9	0.087	197	3.2	19	0.9
20	2.5E-15	2.5E-14	4417	1800	506	0.00061	130	60	25	9.8	1.43E-07	6.3E-07	0.8	0.01	95	0.8	18	0.34	2.1	0.096	179	3.4	21	1.0
21	2.5E-15	2.5E-14	5764	1400	327	0.00061	150	45	25	9.8	1.43E-07	6.3E-07	0.8	0.01	143	1.1	10	0.27	1.4	0.062	105	2.7	14	0.6
22	2.5E-15	2.5E-14	4650	1800	430	0.00061	140	65	25	9.8	1.43E-07	6.3E-07	0.8	0.01	108	0.9	19	0.34	1.8	0.082	194	3.4	18	0.8
23	2.5E-15	2.5E-14	5589	2000	418	0.00061	150	60	25	9.8	1.43E-07	6.3E-07	0.8	0.01	139	1.1	20	0.38	1.7	0.080	199	3.8	17	0.8
24	2.5E-15	2.5E-14	5233	1200	363	0.00061	150	45	25	9.8	1.43E-07	6.3E-07	0.8	0.01	130	1.0	9	0.23	1.5	0.069	90	2.3	15	0.7
25	2.5E-15	2.5E-14	5085	1700	424	0.00061	150	60	25	9.8	1.43E-07	6.3E-07	0.8	0.01	127	1.0	17	0.32	1.8	0.081	169	3.2	18	0.8

26	2.5E-15	2.5E-14	5584	1000	387	0.00061	160	45	25	9.8	1.43E-07	6.3E-07	0.8	0.01	148	1.1	7	0.19	1.6	0.074	75	1.9	16	0.7
27	2.5E-15	2.5E-14	5567	1000	367	0.00061	160	45	25	9.8	1.43E-07	6.3E-07	0.8	0.01	148	1.1	7	0.19	1.5	0.070	75	1.9	15	0.7
28	2.5E-15	2.5E-14	5690	2200	385	0.00061	150	60	25	9.8	1.43E-07	6.3E-07	0.8	0.01	142	1.1	22	0.42	1.6	0.073	219	4.2	16	0.7
29	2.5E-15	2.5E-14	5604	1100	354	0.00061	160	60	25	9.8	1.43E-07	6.3E-07	0.8	0.01	149	1.1	11	0.21	1.5	0.067	109	2.1	15	0.7
30	2.5E-15	2.5E-14	4436	1400	373	0.00061	150	65	25	9.8	1.43E-07	6.3E-07	0.8	0.01	110	0.8	15	0.27	1.5	0.071	151	2.7	15	0.7
31§	2.5E-15	2.5E-14	6445	1400	311	0.00061	170	40	25	9.8	1.43E-07	6.3E-07	0.8	0.01	182	1.2	9	0.27	1.3	0.059	93	2.7	13	0.6
32§	2.5E-15	2.5E-14	7020	1200	424	0.00061	175	45	25	9.8	1.43E-07	6.3E-07	0.8	0.01	204	1.3	9	0.23	1.8	0.081	90	2.3	18	0.8
33	2.5E-15	2.5E-14	6092	1000	451	0.00061	180	70	25	9.8	1.43E-07	6.3E-07	0.8	0.01	182	1.2	12	0.19	1.9	0.086	116	1.9	19	0.9
34	2.5E-15	2.5E-14	5790	2000	363	0.00061	150	40	20	9.8	1.43E-07	6.3E-07	0.8	0.01	144	1.1	13	0.38	1.2	0.069	133	3.8	12	0.7
35	2.5E-15	2.5E-14	5121	1000	341	0.00061	150	40	25	9.8	1.43E-07	6.3E-07	0.8	0.01	127	1.0	7	0.19	1.4	0.065	66	1.9	14	0.6
36	2.5E-15	2.5E-14	2933	1200	674	0.00061	100	60	25	9.8	1.43E-07	6.3E-07	0.8	0.01	49	0.6	12	0.23	2.8	0.128	119	2.3	28	1.3
37	2.5E-15	2.5E-14	2884	500	431	0.00061	100	25	25	9.8	1.43E-07	6.3E-07	0.8	0.01	48	0.5	2	0.10	1.8	0.082	21	1.0	18	0.8

***** Permeability of 80% shale and 20% sand based on Torbrook well log sediment accumulation intersected on NS1400 transect line OETRA Play Fairway Analysis (2011). Fault influenced permeability (k_f) is based on a single magnitude reduction of the initial permeability (k) value.

† Depth of predicted circulation cell depths. The z_1, z_2, and z_3 marks the test for bottom of diapir to ocean floor, top of diapir to ocean floor and DHI to ocean floor, respectively. All sites based on DHI locations (Fig. S2) with depths defined by 2D cross-line seismic sections or isocore map detailing the depth of all diapirs to the ocean bottom (Fig. S3).

‡ Temperature changes (ΔT_1, ΔT_2, ΔT_3) to various basin depth ranges (z_1, z_2, and z_3) are based on the geothermal model of Negulic & Louden (2016).

§ DHIs # 31 and 32 are sites 2A-1 and 2B-1, respectively.

R_a and P_e are Rayleigh and Péclet numbers calculated based on Eq. 11 and 12 in the Methods section.

Additional ground water flow model parameters are listed below:

Symbol	Description	SI unit	Values
k	Permeability	m2	2.50×10^{-15}
z	Thickness of reservoir	m	5000
β	Water expansivity	$°C^{-1}$	6.10×10^{-4}

∇T	Temperature change over domain	°C	125
g	Gravity	$m2 \cdot s^{-1}$	9.8
kθ	Thermal diffusivity of saturated matrix	$m2 \cdot s^{-1}$	1.43×10^{-7}
V	Water viscosity	$m2 \cdot s^{-1}$	6.30×10^{-7}
Γ	Ratio of volume heat capacity of saturated matrix to fluid	Dimensionless	0.8
γ	Coefficient of fluid density dependence on salinity	wt (%)$^{-1}$	0.01
Ra	Rayleigh number	Dimensionless	
Pe	Péclet number	Dimensionless	

† Derived from geothermal gradient model of Negulic & Louden (2016).

Supplemental Figures

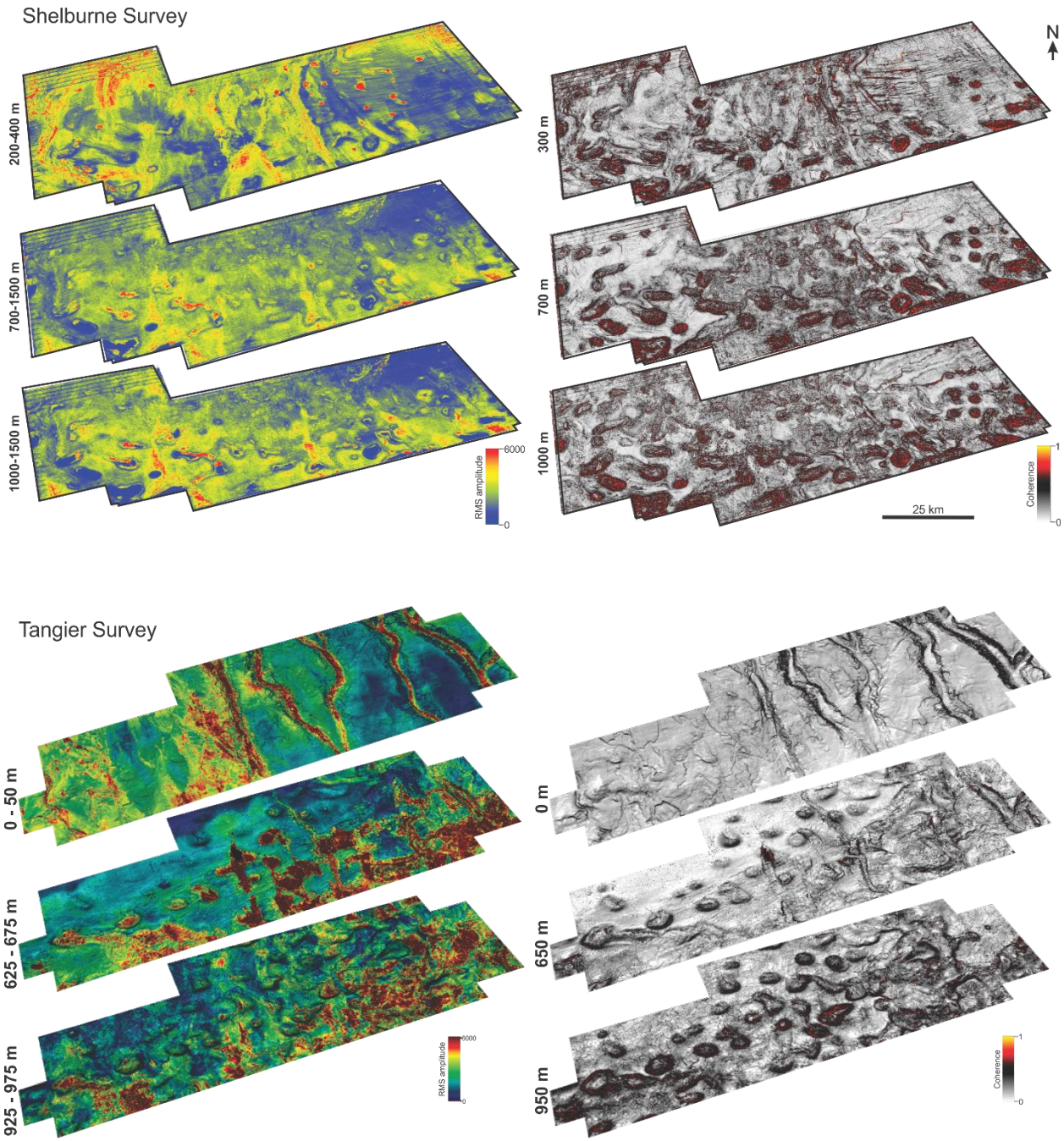

Fig. S1. Root mean square (RMS) (left) and coherence (right) seismic attribute maps for the Shelburne (top) and Tangier (bottom) data blocks.

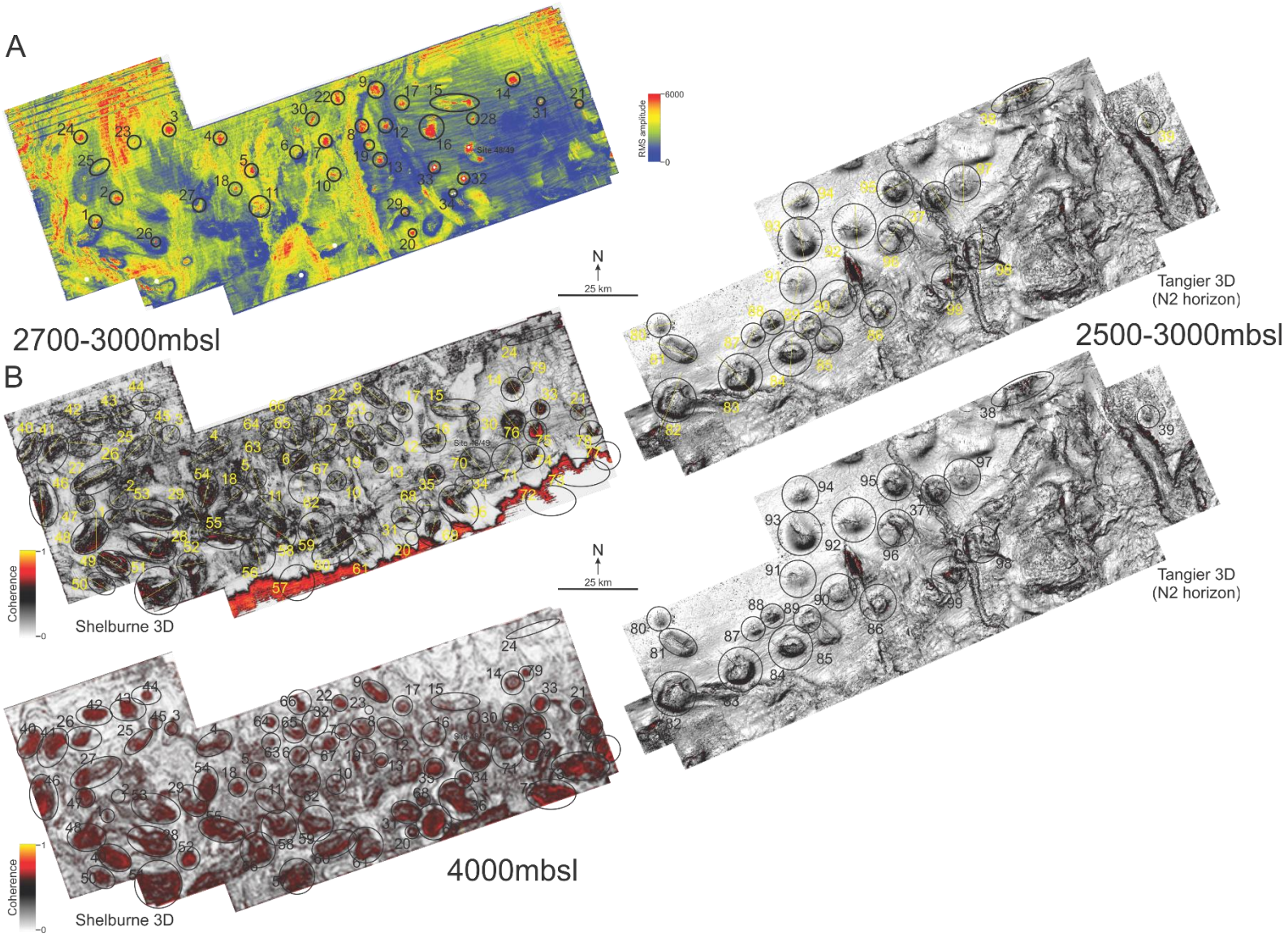

Fig. S2. A) RMS map of the Shelburne data block with DHIs numbered. B) Covariance maps of the Shelburne and Tangier data blocks for different depth intervals showing the location and number assignments for the underlying salt diapirs.

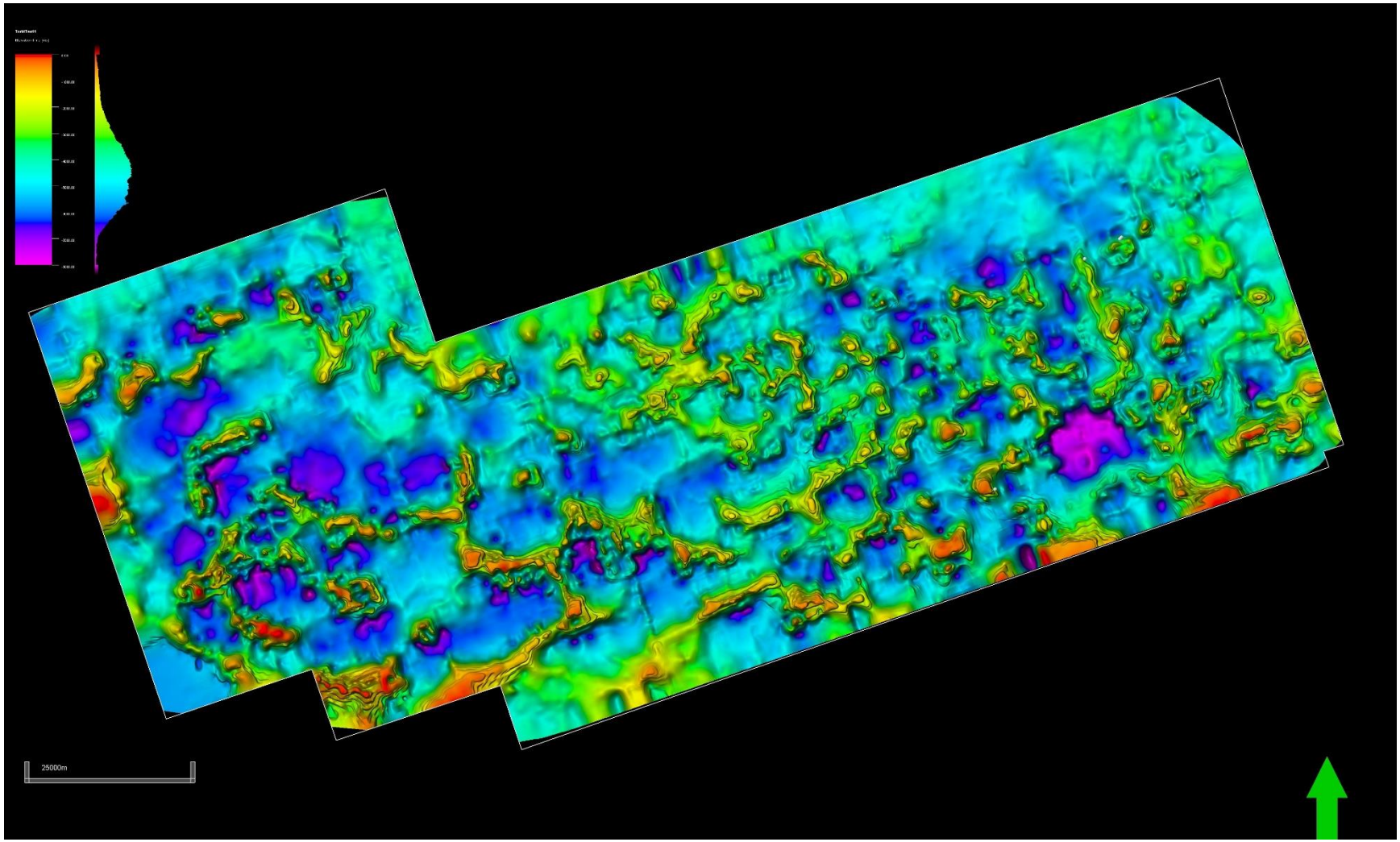

Fig. S3. Shelburne isocore map marking the thickness of overburden sedimentary above each salt diapir. Deeper buried diapirs are found in more shallow water settings closer to the shelf.

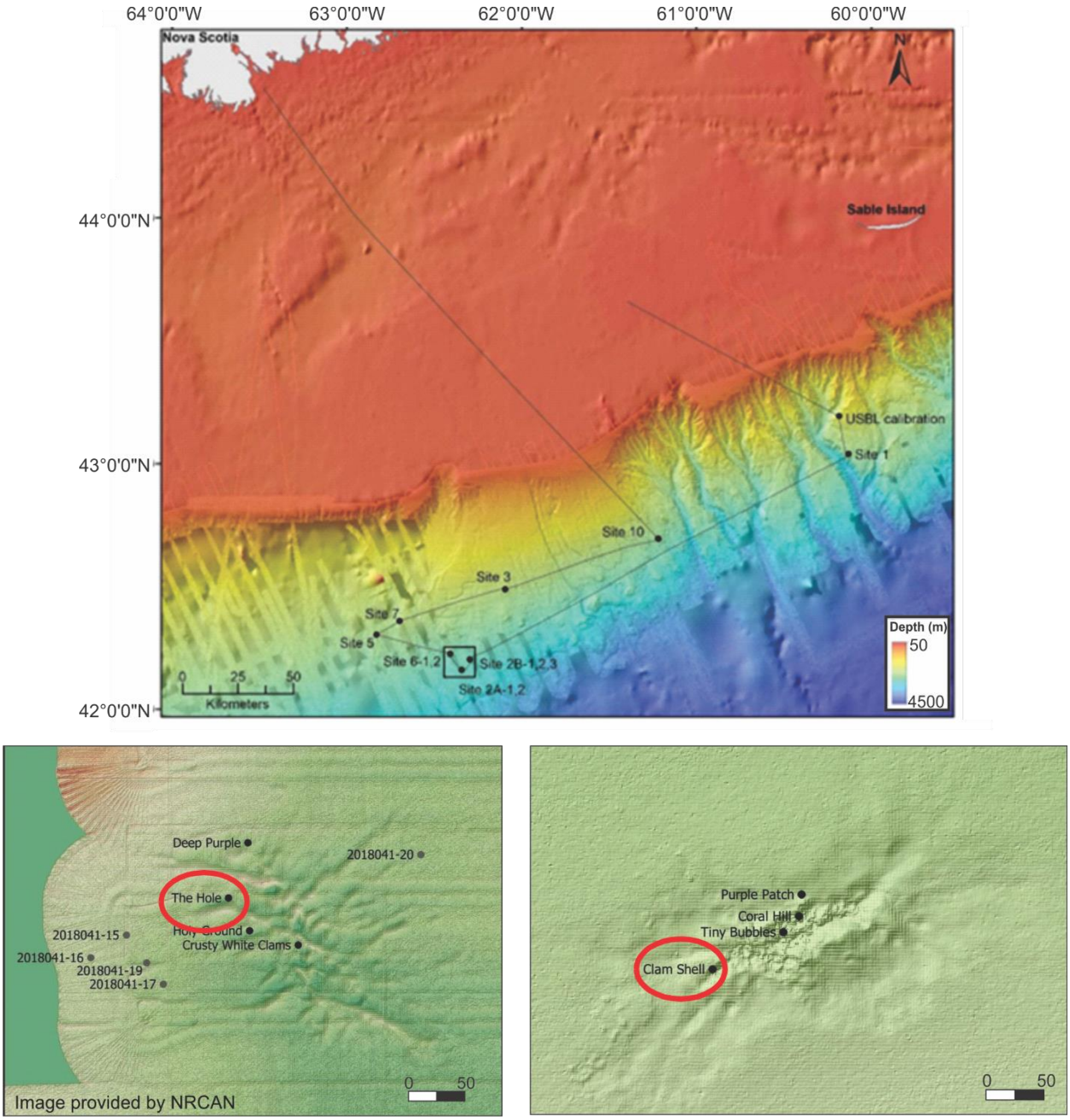

Fig. S4. Bathymetric map (top) of the southern Scotian Slope showing the location of ROV sampled seep sites 2A-1 and 2B-1 (black box). Multibeam maps of sites 2A-1 (bottom left) and 2B-1 (bottom right). Red ellipses indicate the sites of active seepage. Positions of 2018 gravity coring locations indicated on the Site 2A-1 map (modified from Bennet and Desiage, 2022).

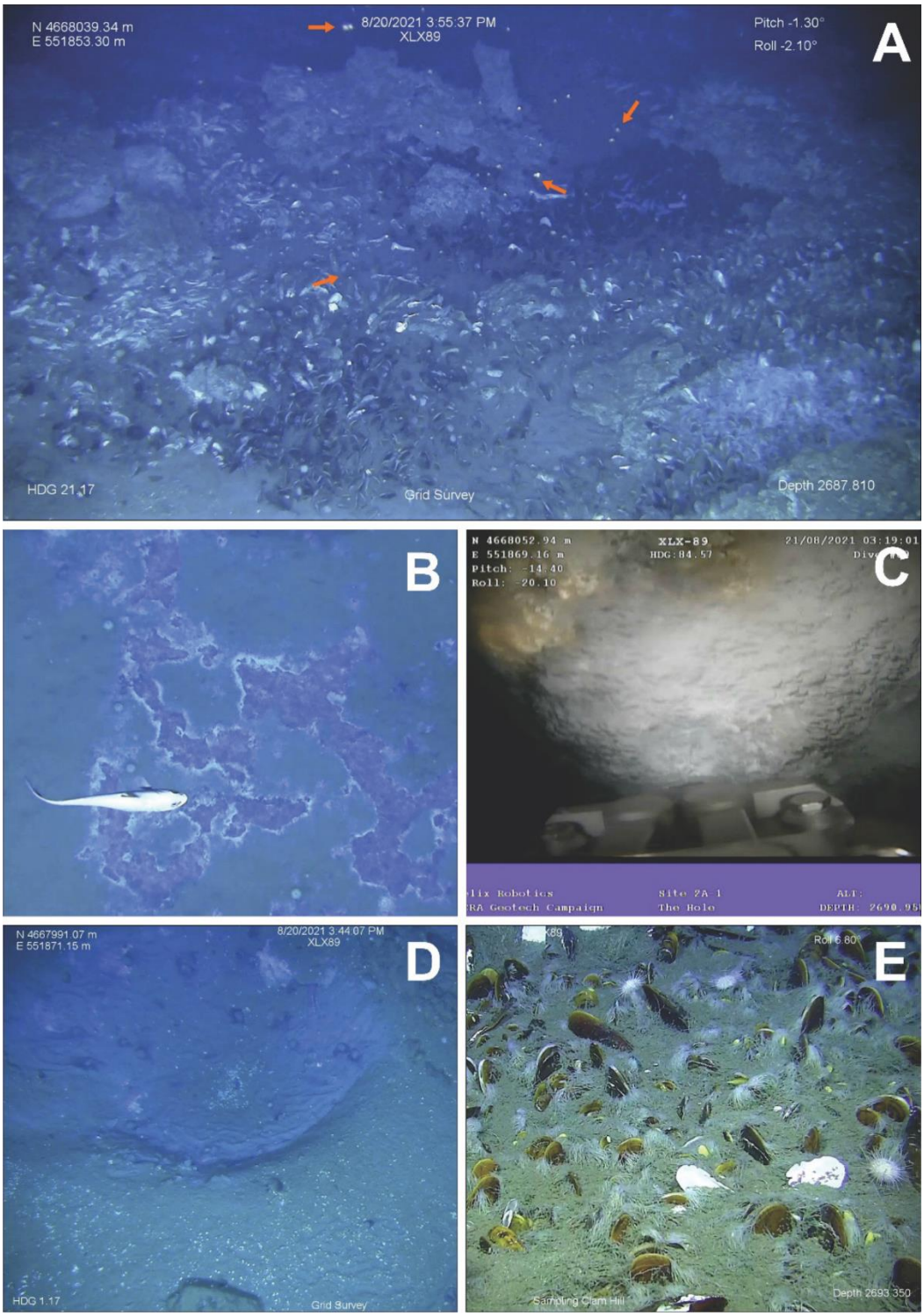

Fig. S5. Seep site 2A-1 seafloor photographs. A) Image of The Hole, with red arrows indicating bubbles. B) Hot spot coring site Deep Purple with white and light-purple microbial maps. C) Gas hydrates with bubbles trapped under a carbonate rim in The Hole. D) Coring hot spot site with crater-like structure with bivalves, shells and carbonates. E) Holy Ground coring hot spot site Clam Hill with mussel and bivalve patch with sea urchins (from Bennett and Desiage, 2022).

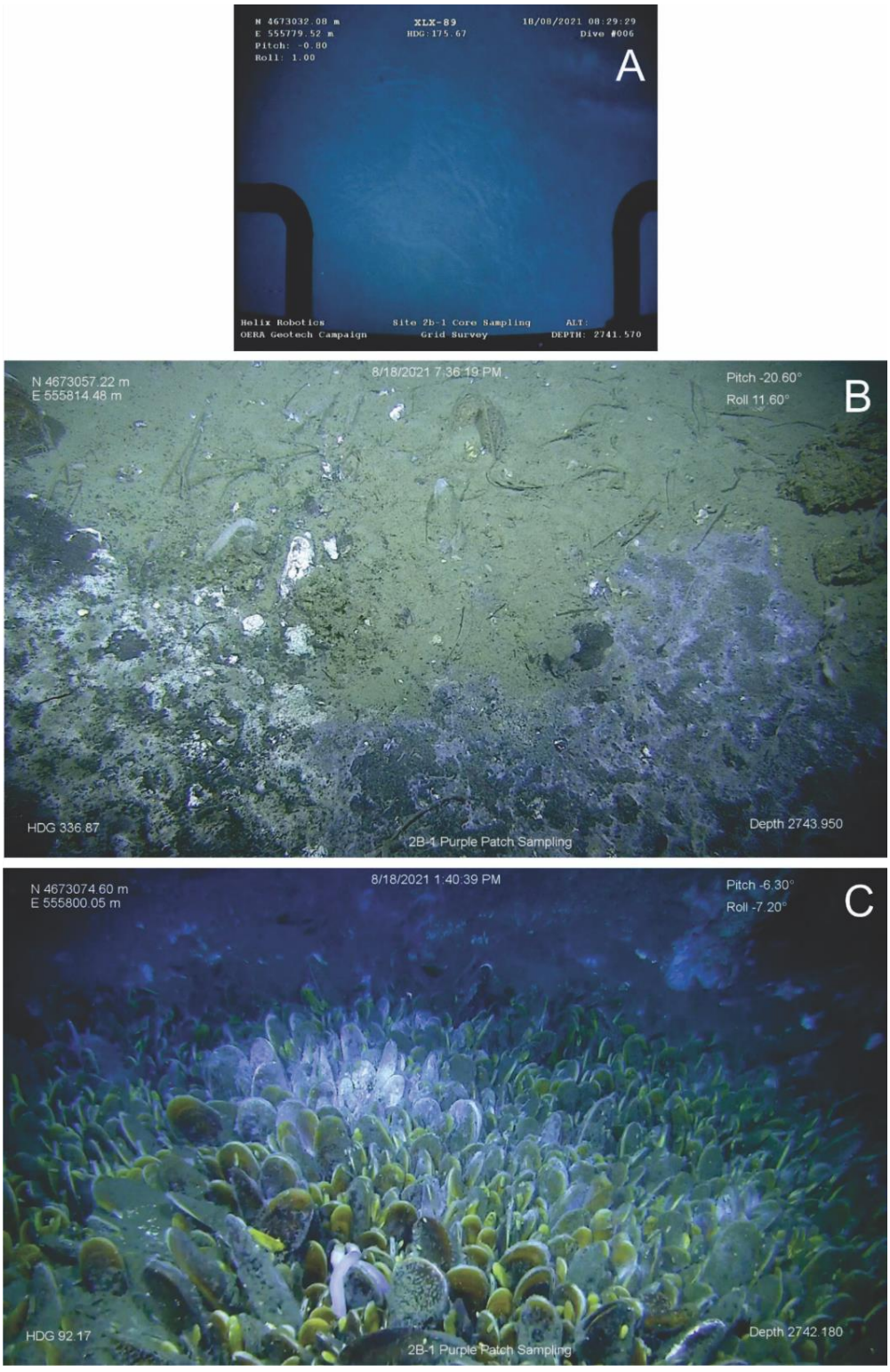

Fig. S6. Seep site 2B-1 seafloor photographs. A) Bioturbation of the sediment by sea urchins evidenced by urchin tracks. B) White, grey, and purple microbial mats at the Tiny Bubbles coring hot spot. C) Autogenic carbonate mound encrusted with mussels and bivalves from the Coral Hill hotspot coring location (from Bennett and Desiage, 2022).

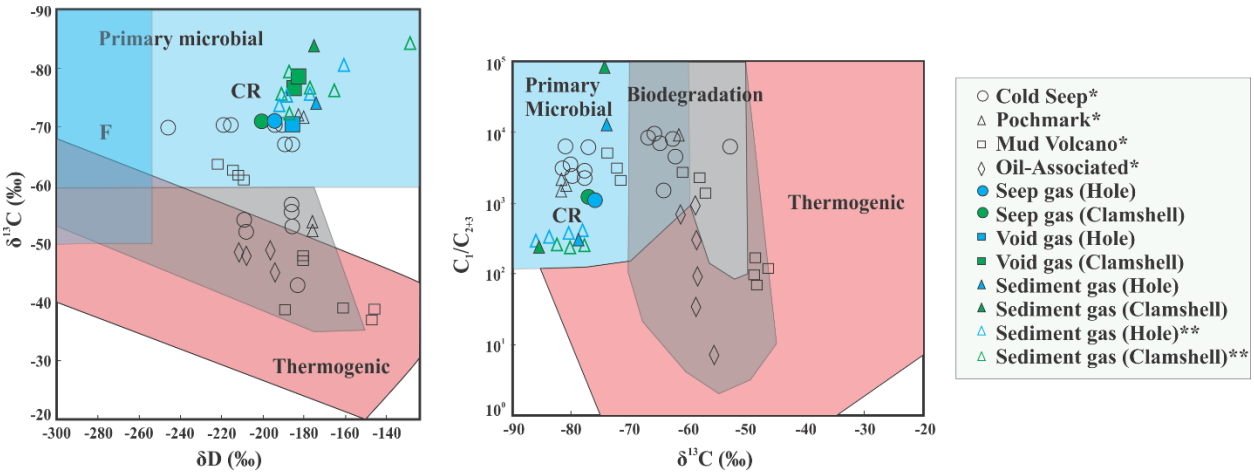

Fig. S7. Whiticar-Schoell plot (left) showing $\delta^{13}C$ and δD values of methane. Bernard plot (right) showing $\delta^{13}C$ values versus C_1/C_{2+3} (both plots modified from Milkov and Etiope, 2018). Non-Scotian seep sample data and formation and alteration boundaries from Lalk et al. (2022).

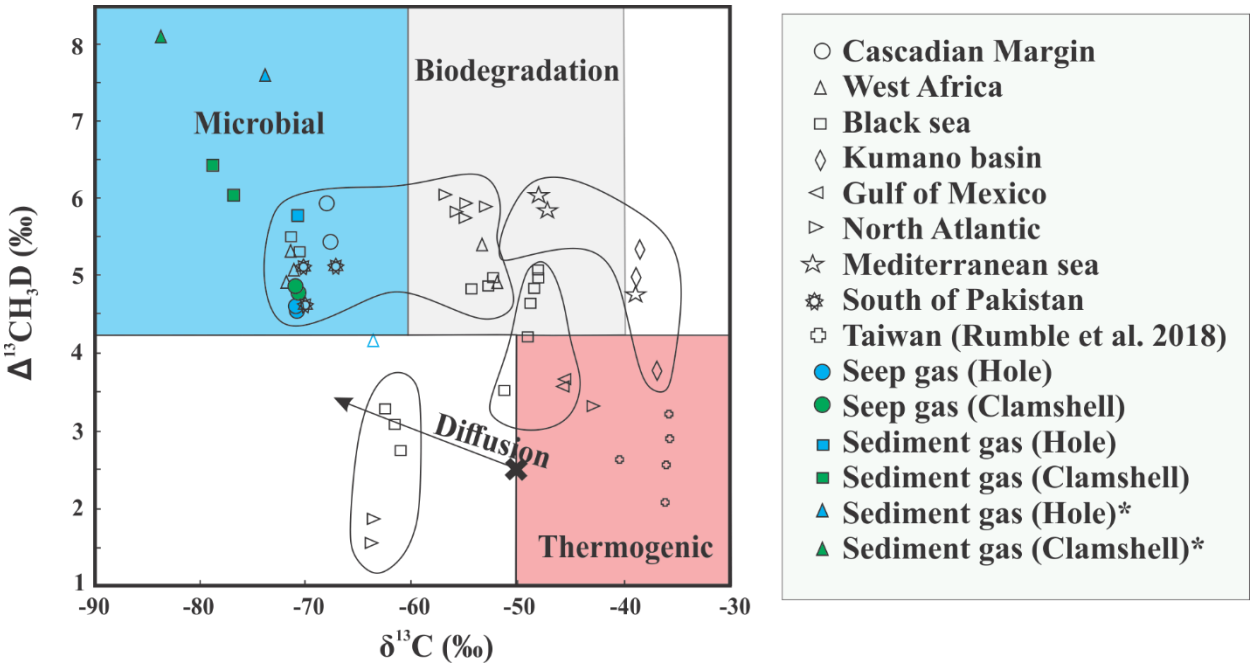

Fig. S8. Cross-plot of $\delta^{13}C$ and $\Delta^{13}CH_3D$ values. Quadrants are defined based on attribute diagrams from Whiticar (1999) and Milkov and Etiope (2018) with the upper limit of secondary microbial methanogenesis (Wilhelms et al., 2001; Head et al., 2003). Non-Scotian seep sample data and formation and alteration boundaries from Lalk et al. (2022). Arrow with "X" indicates isotope change due to diffusion as slow movement of the gas from its source.

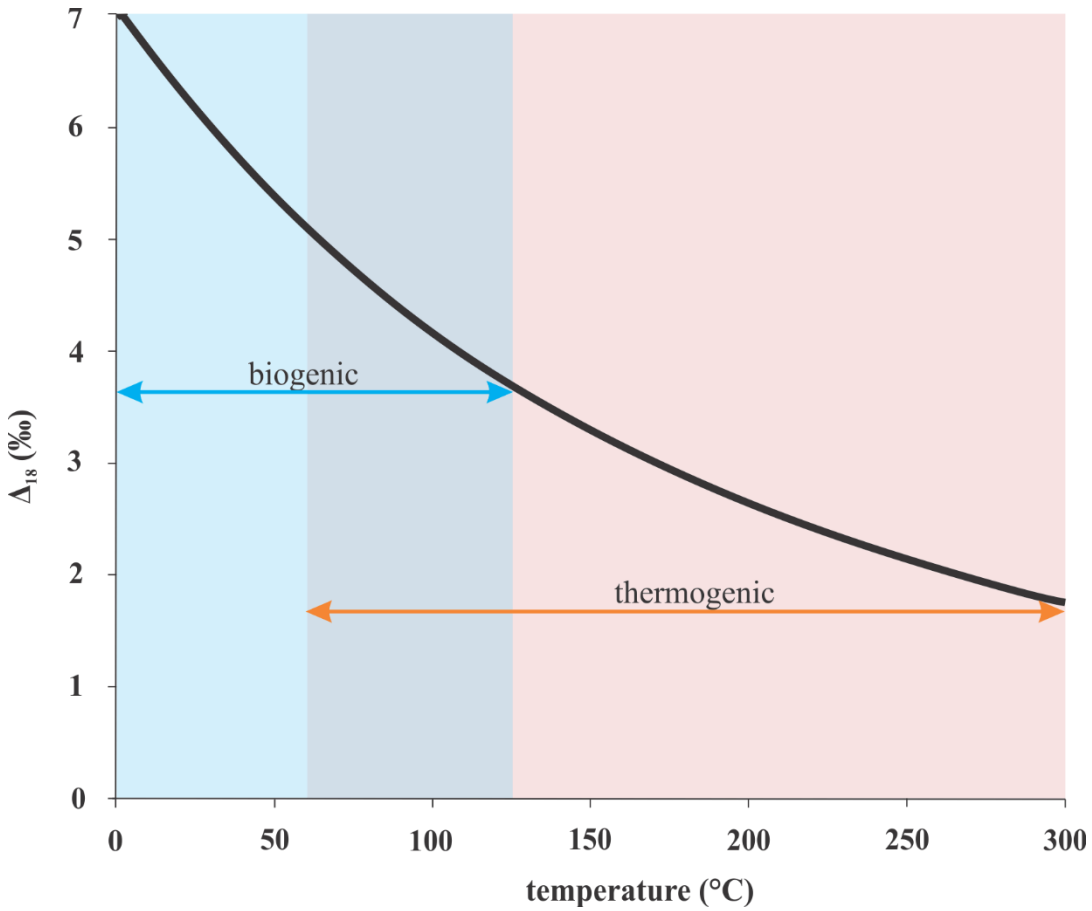

Fig. S9. Equilibrium dependence of Δ_{18} on temperature (modified from Stolper et al., 2014). Expected ranges are given for biogenic and thermogenic gases formed in clumped-isotopic equilibrium. The overall thermogenic range is derived from the start of the oil window of c. 60 °C (Hunt, 1996) through c. 300 °C; 300 °C is the approximate modelled maximum temperature of methane generation (e.g., Behar et al., 1992; Vandenbroucke et al., 1999; Burruss & Laughrey, 2010), though the maximum temperature of thermogenic gas generation is poorly constrained (Seewald, 2003).

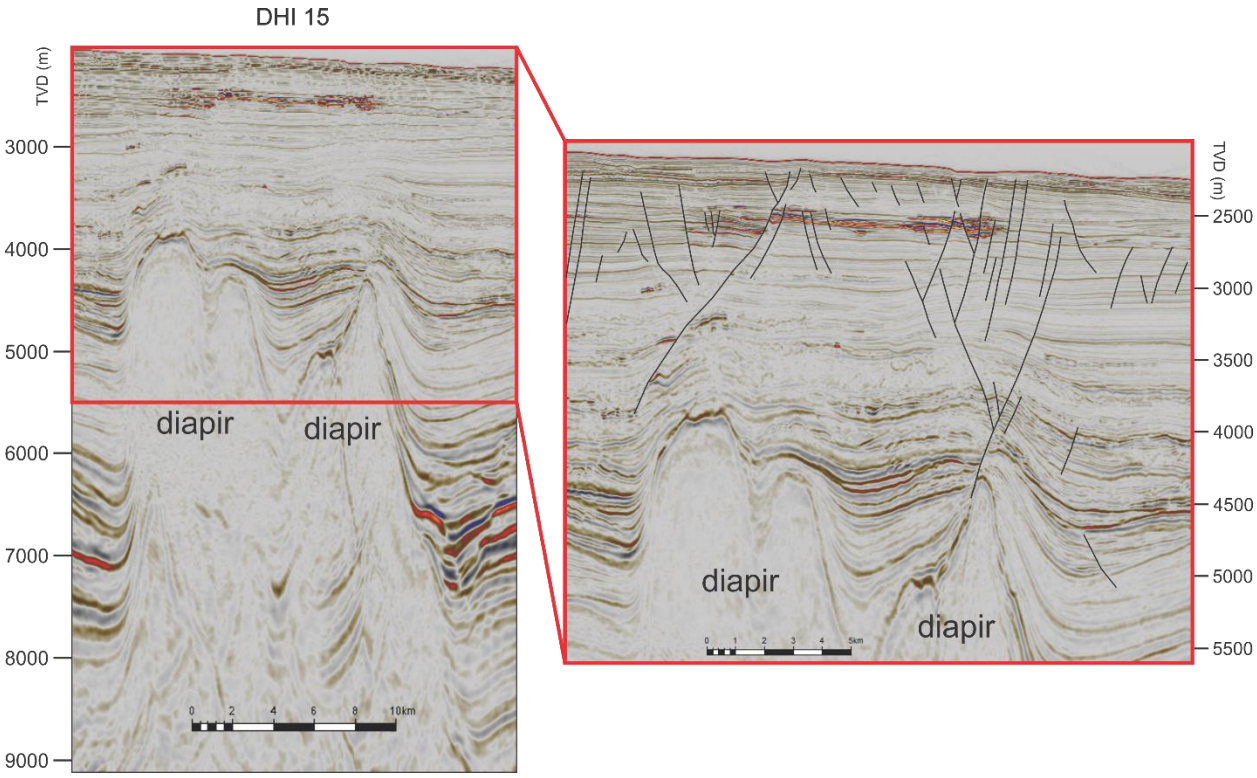

Fig. S10. Strike-oriented seismic cross-section located on the Shelburne 3D area showing the resolved subsurface geology spanning DHI 15 (see Fig. S2 for location). Red box on the right marks a more shallow blow-up of the profile with faults outlined in black. Yellow ellipse marks the location of the DHI (data courtesy of Shell via NSDNRR). Up to four diapirs are apparent collectively forming an ~12K wide subsurface salt plateau.

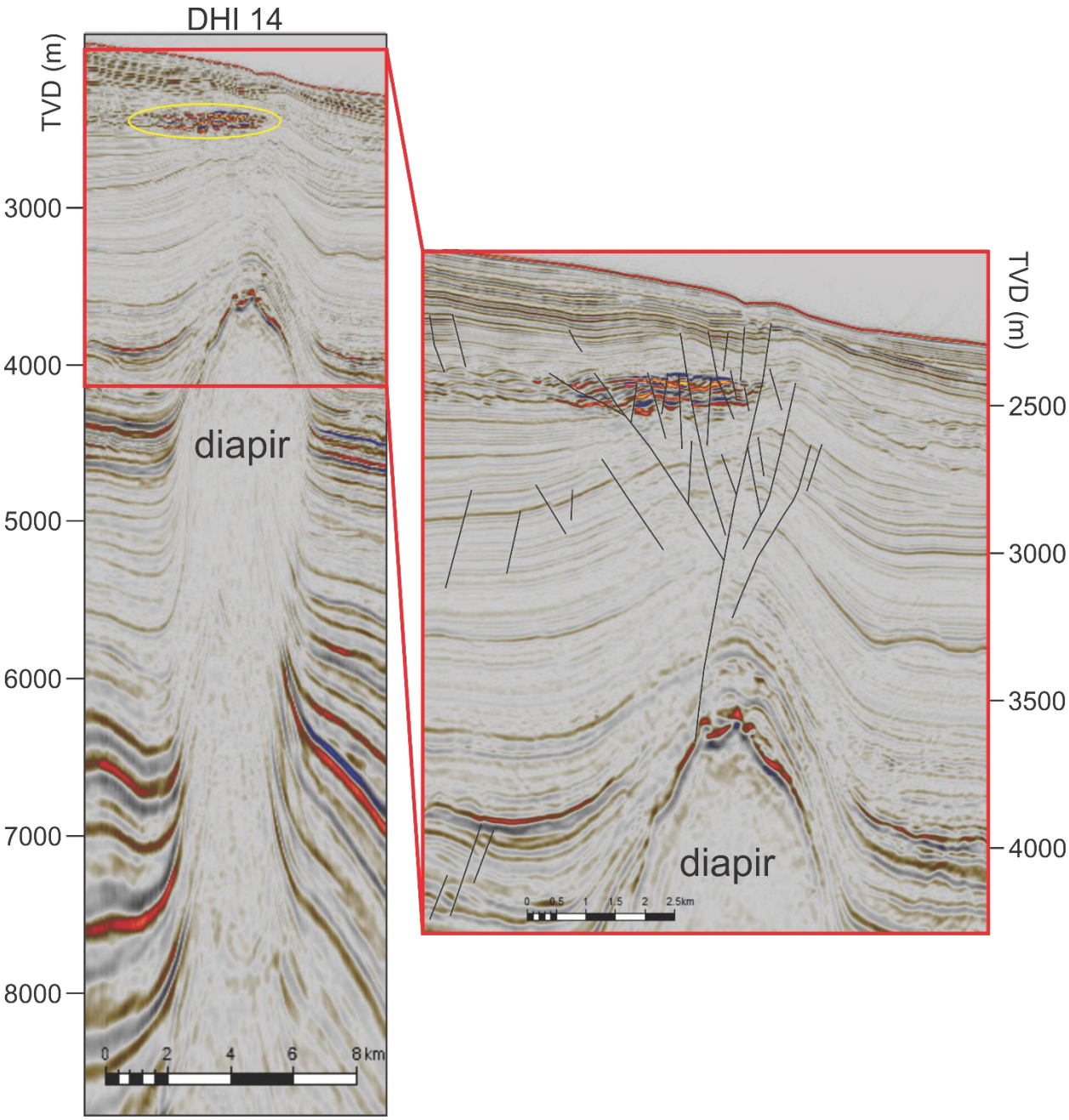

Fig. S11. Strike-oriented seismic cross-section located on the Shelburne 3D area showing the resolved subsurface geology spanning DHI 14 (see Fig. 4 and S2 for location). Red box on the right marks a more shallow blow-up of the profile with faults outlined in black. Yellow ellipse marks the location of the DHI (data courtesy of Shell via NSDNRR).

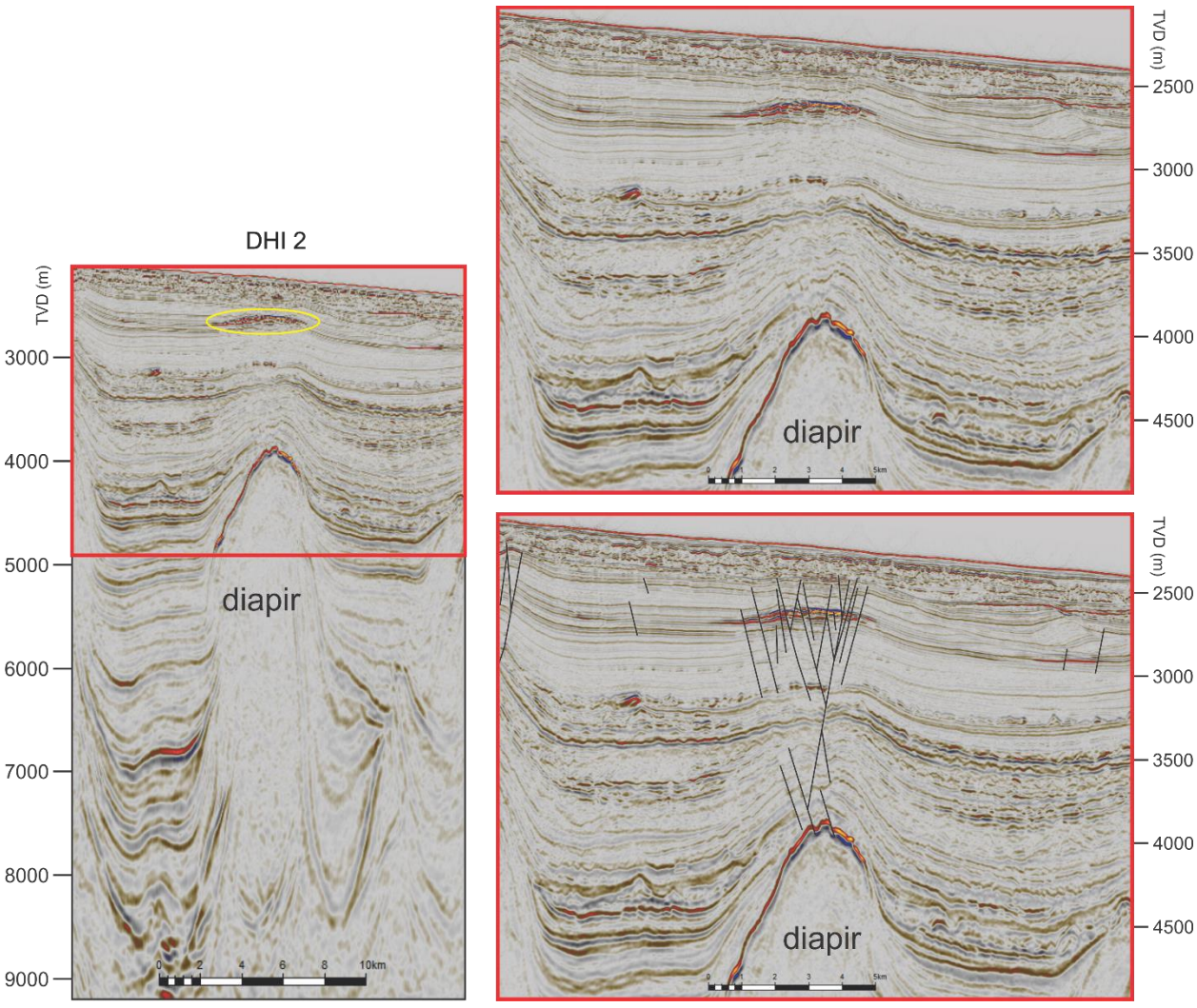

Fig. S12. Strike-oriented seismic cross-section located on the Shelburne 3D area showing the resolved subsurface geology spanning DHI 2 (see Fig. S2 for location). Red box on the right marks a more shallow blow-up of the profile with faults outlined in black. Yellow ellipse marks the location of the DHI (data courtesy of Shell via NSDNRR).

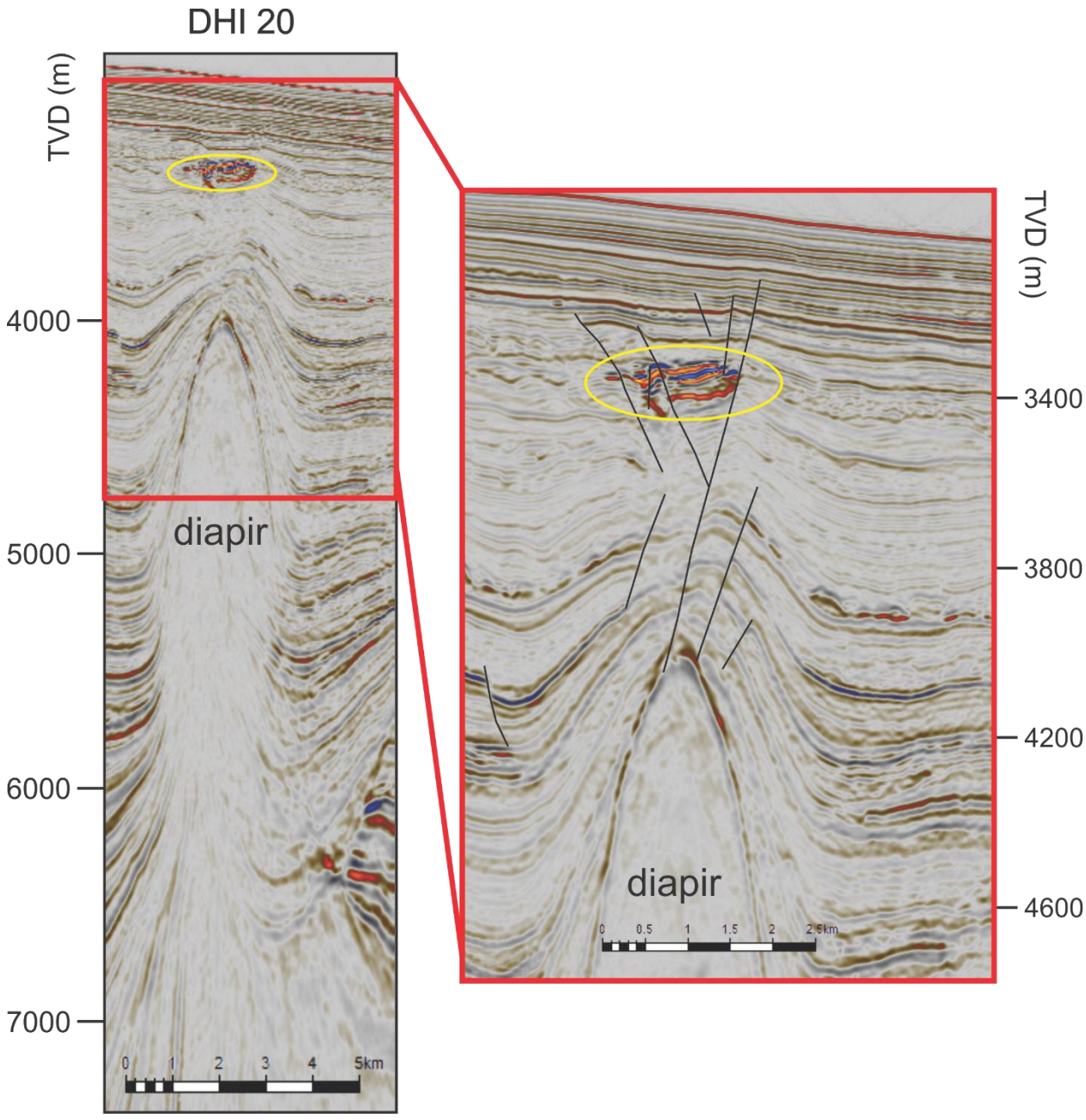

Fig. S13. Strike-oriented seismic cross-section located on the Shelburne 3D area showing the resolved subsurface geology spanning DHI 20 (see Fig. S2 for location). Red box on the right marks a more shallow blow-up of the profile with faults outlined in black. Yellow ellipse marks the location of the DHI (data courtesy of Shell via NSDNRR).

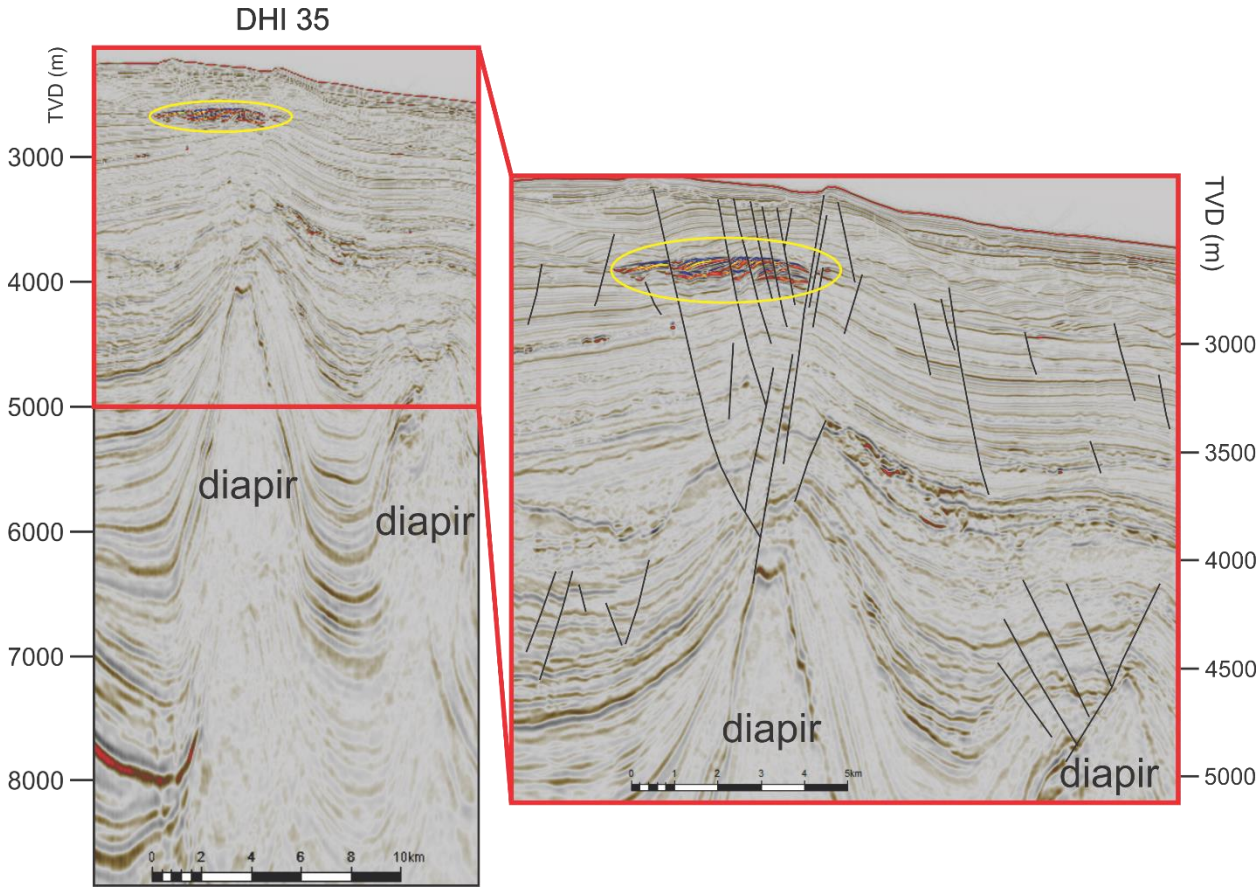

Fig. S14. Strike-oriented seismic cross-section located on the Shelburne 3D area showing the resolved subsurface geology spanning DHI 35 (see Fig. S2 for location). Red box on the right marks a more shallow blow-up of the profile with faults outlined in black. Yellow ellipse marks the location of the DHI (data courtesy of Shell via NSDNRR).

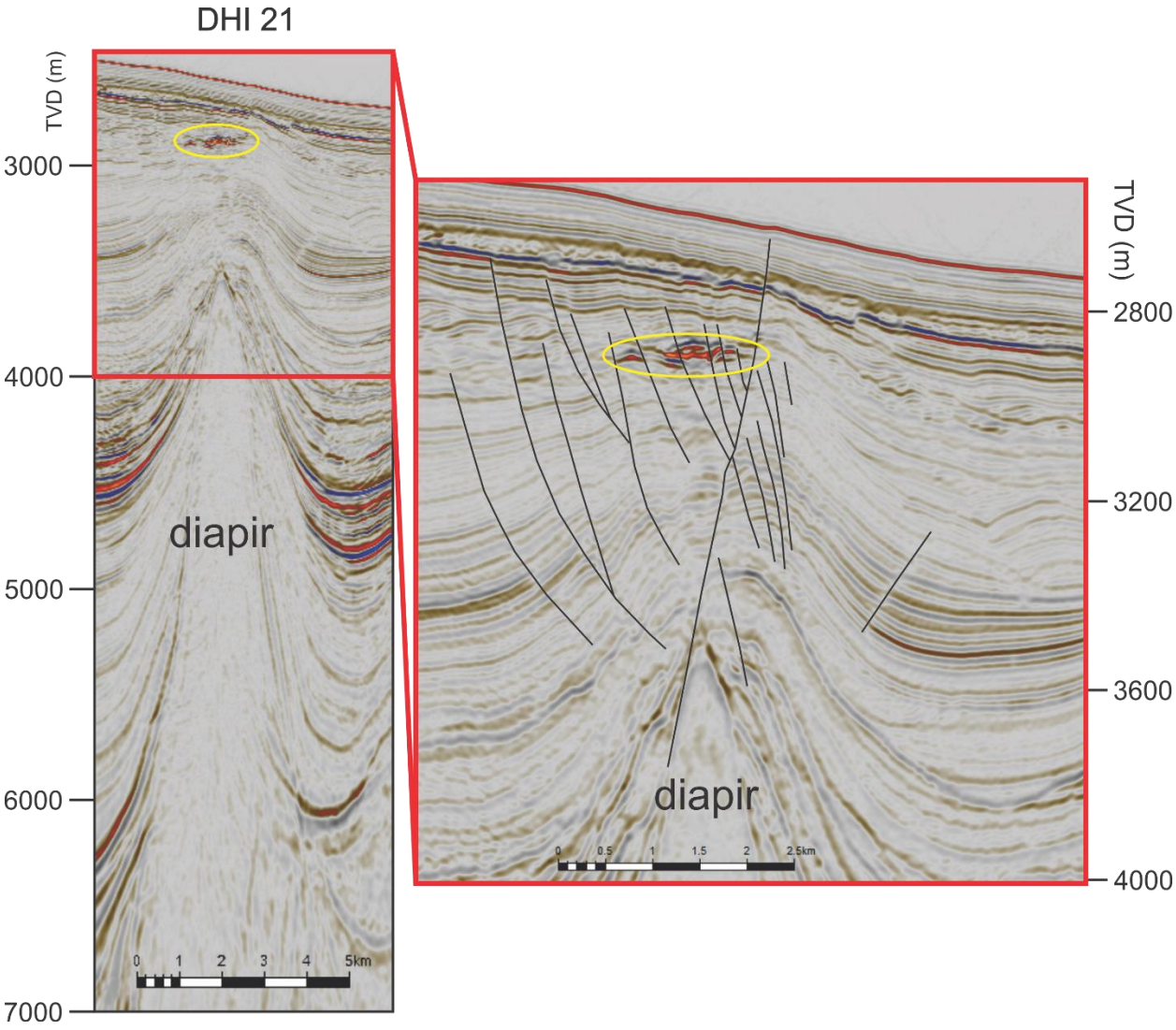

Fig. S15. Strike-oriented seismic cross-section located on the Shelburne 3D area showing the resolved subsurface geology spanning DHI 21 (see Fig. S2 for location). Red box on the right marks a more shallow blow-up of the profile with faults outlined in black. Yellow ellipse marks the location of the DHI (data courtesy of Shell via NSDNRR).

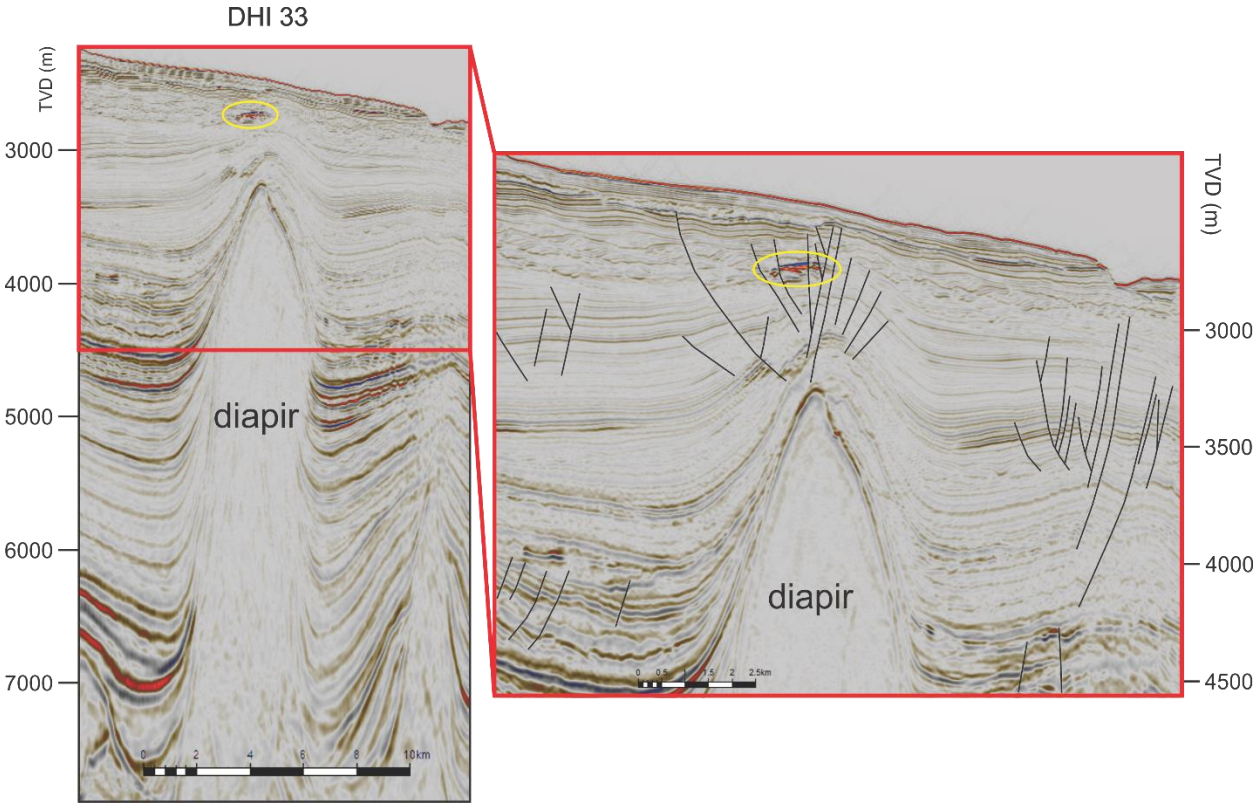

Fig. S16. Strike-oriented seismic cross-section located on the Shelburne 3D area showing the resolved subsurface geology spanning DHI 33 (see Fig. S2 for location). Red box on the right marks a more shallow blow-up of the profile with faults outlined in black. Yellow ellipse marks the location of the DHI (data courtesy of Shell via NSDNRR).

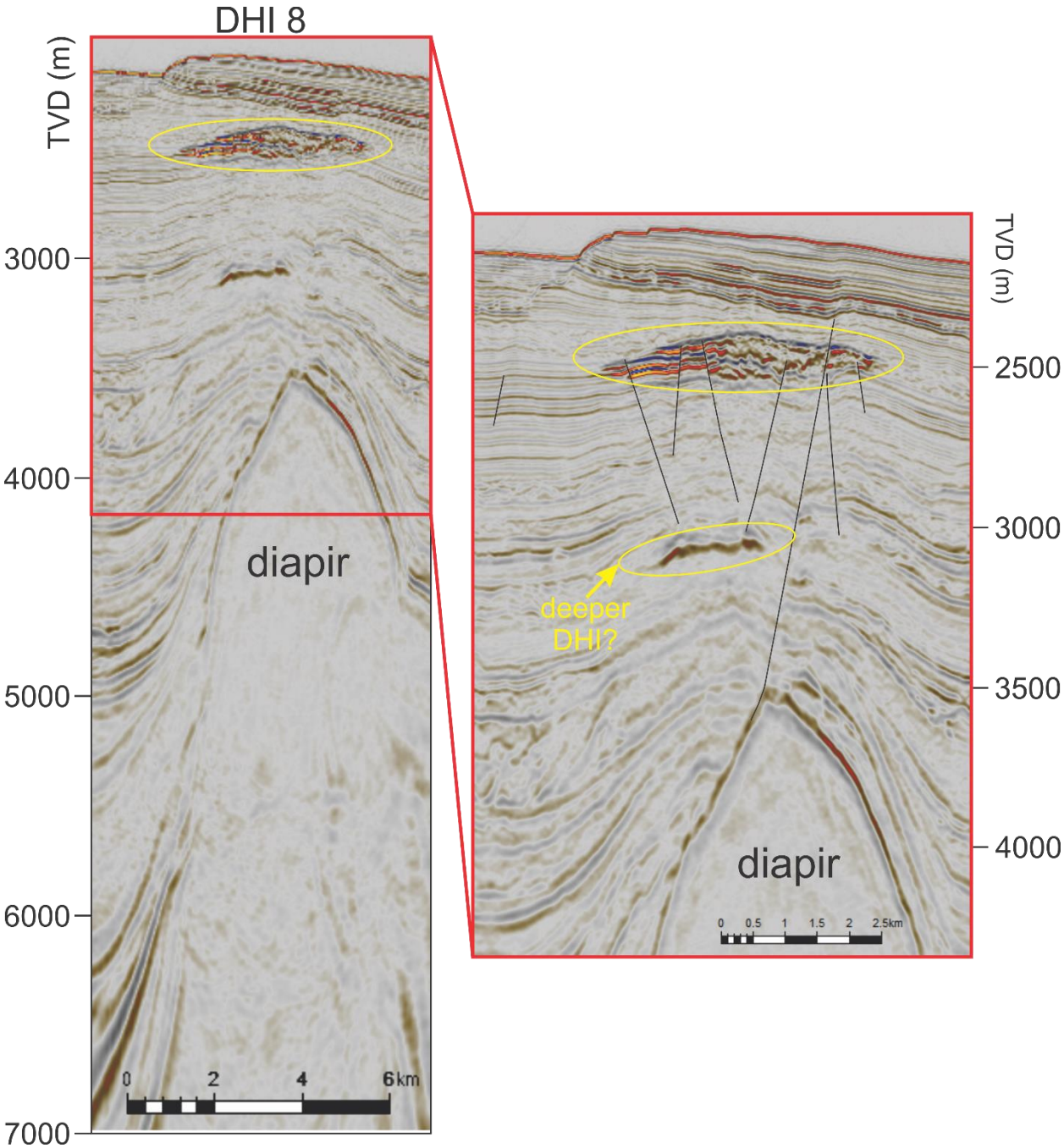

Fig. S17. Strike-oriented seismic cross-section located on the Shelburne 3D area showing the resolved subsurface geology spanning DHI 8 (see Fig. S2 for location). Red box on the right marks a more shallow blow-up of the profile. Yellow ellipse marks the locations of the DHIs (data courtesy of Shell via NSDNRR). This site hosts the only deep (700 – 1500 mbsf) DHI observed in the diapiric province.

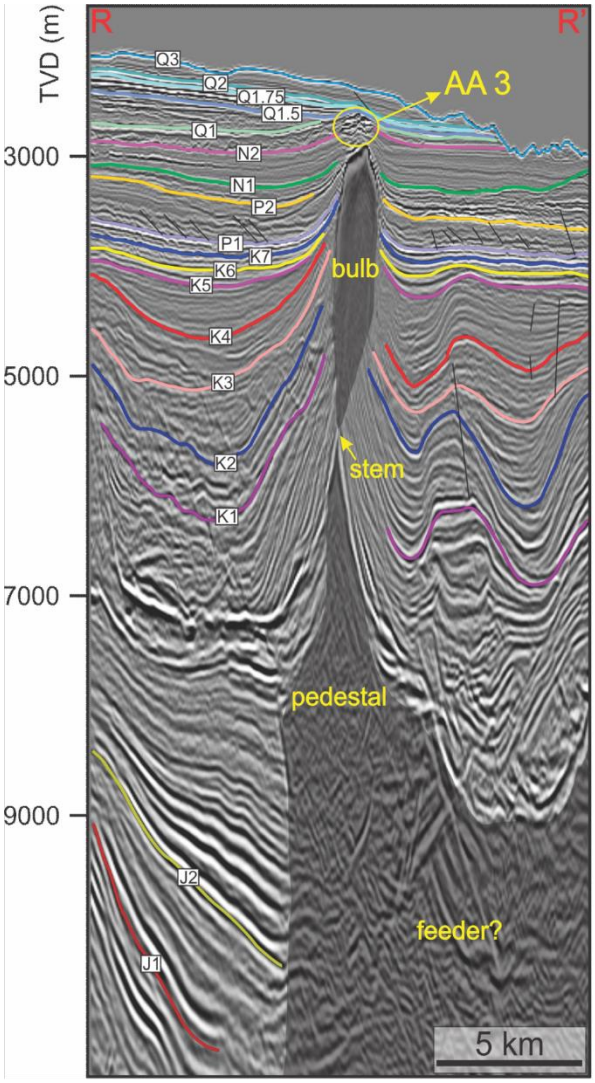

Fig. S18. Strike-oriented Tangier 3D survey seismic profile showing interpreted DHI-39 (AA 3; see Fig. S2 for location). Yellow ellipse marks the location of the DHI (data courtesy of BP Canada Exploration Ltd via NSDNRR).

Supplemental References

Behar, F., Kressmann, S., Rudkiewicz, J. L., & Vandenbroucke, M. (1992). Experimental simulation in a confined system and kinetic modelling of kerogen and oil cracking. Organic Geochemistry, 19(1-3), 173-189.

Bennett, R., & Desiage, P.-A. (2022). Expedition report 21CONDOR: Scotian Slope, August 14–29, 2021; Geological Survey of Canada, Open File 8889, 53 p. https://doi.org/10.4095/329977.

Burruss, R. C., & Laughrey, C. D. (2010). Carbon and hydrogen isotopic reversals in deep basin gas: Evidence for limits to the stability of hydrocarbons. Organic Geochemistry, 41(12), 1285-1296.

Fowler, M. G. (2022). Geochemistry Data Report - 2021 Offshore Nova Scotia ROV Push Cores Geochemistry, Report for Nova Scotia Department of Natural Resources and Renewables.

Head, I. M., Jones, D. M., & Larter, S. R. (2003). Biological activity in the deep subsurface and the origin of heavy oil. Nature, 426, 344–352.

Hunt, J. M. (1996). Petroleum geochemistry and geology. W.H. Freeman and Co.

Lalk, E., Pape, T., Gruen, D. S., Kaul, N., Karolewski, J. S., Bohrmann, G., & Ono, S. (2022). Clumped methane isotopologue-based temperature estimates for sources of methane in marine gas hydrates and associated vent gases. Geochimica et Cosmochimica Acta, 327, 276-297.

MacDonald, I. R., Leifer, I., Sassen, R., Stine, P., Mitchell, R., & Guinasso, N. Jr. (2002). Transfer of hydrocarbons from natural seeps to the water column and atmosphere. Geofluids, 2, 95–107. doi: 10.1046/j.1468-8123.2002.00023. x.

Milkov, A. V., & Etiope, G. (2018). Revised genetic diagrams for natural gases based on a global dataset of >20,000 samples. Organic Geochemistry, 125, 109–120.

Negulic, E., & Louden, K. E. (2016). The thermal structure of the central Nova Scotia Slope (eastern Canada): seafloor heat flow and thermal maturation models. Can. J. Earth Sci., 54, 146–162.

OETRA. (2011). Play Fairway Analysis Atlas – Offshore Nova Scotia. Nova Scotia Department of Energy Report. 347. https://oera.ca/research/play-fairway-analysis-atlas.

Römer, M., Wenau, S., Mau, S., Veloso, M., Greinert, J., Schlüter, M., et al. (2017). Assessing marine gas emission activity and contribution to the atmospheric methane inventory: a multidisciplinary approach from the Dutch Dogger Bank seep area (North Sea). Geochem. Geophys. Geosyst., 18, 2617–2633. doi: 10.1002/2017gc006995.

Seewald, J. S. (2003). Organic-inorganic interactions in petroleum producing sedimentary basins. Nature, 426, 327–333.

Stolper, D. A., Lawson, M., Davis, C. L., Ferreira, A. A., Santos Neto, E. V., Ellis, G. S., ... Eiler, J. M. (2014). Formation temperatures of thermogenic and biogenic methane. Science, 344, 1500–1503.

Vandenbroucke, M., Behar, F., & Rudkiewicz, J. L. (1999). Kinetic modelling of petroleum formation and cracking: implications from the high pressure/high temperature Elgin Field (UK, North Sea). Organic Geochemistry, 30(9), 1105-1125.

Whiticar, M. J. (1999). Carbon and hydrogen isotope systematics of bacterial formation and oxidation of methane. Chem. Geol., 161, 291–314.

Wilhelms, A., Larter, S. R., Head, I., Farrimond, P., Di-Primio, R., & Zwach, C. (2001). Biodegradation of oil in uplifted basins prevented by deep-burial sterilization. Adv. Pet. Geochem., 411, 1034–1037.